2-2012

Morphology and Development of Droplet Deformation Under Flow Within Microfluidic Devices

Molly Katlin Mulligan
University of Massachusetts Amherst, mollymulligan@gmail.com

MORPHOLOGY AND DEVELOPMENT OF DROPLET DEFORMATION UNDER FLOW WITHIN MICROFLUIDIC DEVICES

A Dissertation Presented

by

MOLLY K. MULLIGAN

Submitted to the Graduate School of the University of Massachusetts Amherst in partial

fulfillment of the degree of

DOCTOR OF PHILOSOPHY

February 2012

Mechanical and Industrial Engineering

MORPHOLOGY AND DEVELOPMENT OF DROPLET

DEFORMATION UNDER FLOW WITHIN MICROFLUIDIC DEVICES

A Dissertation Presented

by

MOLLY K. MULLIGAN

_____

Jonathan P. Rothstein, Chair

_____

J. Blair Perot, Member

_____

David P. Schmidt, Member

_____

Anthony D. Dinsmore, Member

_____

Donald Fisher, Department Head
Department of Mechanical and Industrial Engineering

ACKNOWLEDGMENTS

I would like to acknowledge Center for Heriachial Manufacturing (CHM) and the Materials Research Science and Engineering Center on Polymers (MRSEC) for funding my research throughout my graduate education.

I would like to thank my graduate research adviser, Jonathan Rothstein, for five years worth of guidance, collaboration and helping me in pursuit of my goals. Thanks to Professors Anothony D. Dinsmore, J. Blair Perot and David P. Schmidt for their comments, collaborations and service as my committee member. I would also like to thank John Nicholson for his hard work and dedication in the cleanroom. Without his tireless effort much of this research would not have been possible. A big thank you goes to my lab mates who have put up with me for so long. A special thank you to my lab mates who have graduated before me for all of their help, guidance, and encouragement and for telling me to calm down because I would publish a paper/get a job/finish my dissertation. Finally a special thanks to my parents, my friends and my family for their support along the way.

ABSTRACT

MORPHOLOGY AND DEVELOPMENT OF DROPLET DEFORMATION UNDER FLOW WITHIN MICROFLUIDIC DEVICES

FEBRUARY 2012

MOLLY K. MULLIGAN, B.A, SMITH COLLEGE

PH.D., UNIVERSITY OF MASSACHUSETTS AMHERST

Directed by: Professor Jonathan P. Rothstein

Microfluidics is the science of processing up to microliters of fluid at a time in a channel with dimensions on the order of microns. The small size of the devices allows fluid properties to be studied in a world dominated by viscosity, surface tension, and diffusion rather than gravity and inertia. Microfluidic droplet generation is a well studied and understood phenomena, which has attracted attention due to its potential applications in biology, medicine, chemistry, sensing and diagnostics and a wide range of industries. This dissertation adds to the field of microfluidic droplet studies by studying individual droplet deformation and the process of scaling-up microfluidic devices for industrial use.

The study of droplet deformation under extensional and mixed shear and extensional flows was performed within a microfluidic device. Droplets were generated using a flow-focusing device and then sent through a hyperbolic contraction downstream of the droplet generator. The hyperbolic contraction allowed the smallest droplets to be deformed by purely extensional flows and for the larger droplets to experience mixed extensional and shear flows. The shear resulted from the proximity of the droplet to the

walls of the microfluidic channel. The continuous phase in all of these devices was oil and the dispersed phase was one of three fluids: water, an aqueous surfactant solution, or an aqueous suspension of colloidal particles. Droplet deformation dynamics are affected by the use of surfactants and colloidal particles, which are commonly used to stabilize emulsion droplets again coalescence. Surfactants reduce the interfacial tension between the dispersed and continuous phases and particles can reduce the interfacial tension in the system and form an elastic shell around the droplets.

Microfluidic droplet generating devices have many potential industrial applications; however, due to the low output of product from a single droplet generating device, their potential has not been realized. Using six parallel flow-focusing droplet generators on a single chip, the process of microfluidic droplet formation can be scaled up, thus resulting in a higher output of droplets. The tuning of droplet size and production frequency can be achieved on chip by varying the outlet tubing lengths, thus allowing for a single device to be used to generate a range of droplet sizes.

TABLE OF CONTENTS

Page

LIST OF TABLES

Table Page

LIST OF FIGURES

Figure Page

CHAPTER 1

MICROFLUIDIC DEVICES AND DROPLET FORMATION

1.1 Microfluidics: Motivation and History

Microfluidics is the science and technology of systems that process microliters or less of fluids and devices whose channel dimensions are on the order of microns (100s of nanometers to 999 microns). The small size scales of these devices leads to systems where fluids behave differently from conventional flow theory allowing scientists to probe a world dominated by viscosity, surface tension and diffusion rather than gravity and inertia, which are the dominant forces in our macroscopic world (Atencia and Beebe 2005; Nguyen and Wereley 2006; Whitesides 2006). Microfludics has applications in numerous research areas, ranging from biotechnology, to the food industry, pharmaceuticals, coatings, optics, electronics, etc, and the development of the field of micro-electro mechanical systems (MEMS) in the 1980s, resulted in the technology necessary to make microfluidic systems in a controlled and repeatable method (Stone, Stroock et al. 2004; Atencia and Beebe 2005). Biology was one of the original motivations for the development of microfluidic systems because these devices allow for manipulation on the cellular length scale (Stone, Stroock et al. 2004). Today there are several commercially available microfluidic devices. A frequently encountered microfluidic device is the inkjet printer head. The inkjet printer head uses orifices of less than 100 microns in diameter to produce droplets of ink (Whitesides and Stroock 2001; Christopher and Anna 2007).

Microfluidics offers a number of advantages over macrofluidics including using small amounts of fluids and materials and laminar flows for fluids with low viscosity at high flow rates (Whitesides 2006). Microfluidic devices have high surface area to volume ratios, allowing for more effective heat and mass transfer. Diffusion distances are also smaller leading to shorter reaction times (Atencia and Beebe 2005; Nie, Seo et al. 2008).

As systems are reduced in size the effects of diffusion, surface tension and viscosity begin to dominate. The Reynolds number, used to classify flow type becomes dominated by the viscosity of the system. The Reynolds number, which is the ratio of the inertial to viscous forces, is defined as

$$\mathrm{Re} = \frac{\rho V L}{\mu} \tag{1.1}$$

where ρ is the density of the fluid, V is the average velocity of the fluid, L is the characteristic length scale of the system and μ is the viscosity of the system. In the macroscopic world Reynolds number is generally used to determine whether a flow is laminar or turbulent, where a high Reynolds number (above 4,000 for macroscopic channel flow) corresponds to a turbulent flow. The Reynolds number in microfluidic devices flowing water is on the order of $0.1 \le \mathrm{Re} \le 10$.

1.2 Emulsions

Emulsions, which are defined as stable droplets of one immiscible fluid in another are useful in a range of applications from personal care products such as body wash, to food products such as salad dressing, to the pharmaceutical industry where they can be

utilized as drug delivery vehicles and to the chemical industry where they can be used as microreactors (Shu, Eijkel et al. 2007). In addition, the surfaces of dispersed droplets can be utilized for purification of the bulk phase and as templates for assembly of lipids or colloidal particles for novel materials (Zeng, Bissig et al. 2006). The ability to precisely control drop size in the creation of emulsions has many wide spread industrial applications. Unlike a suspension of solid particles, emulsion droplets are readily deformed under flow because the liquid-liquid interface is mobile (McClements 1999; Fischer and Erni 2007).

Emulsions do not form spontaneously and are generally made through various types of emulsification processes (Chang and Su 2008). Bulk emulsions are traditionally formed using high-speed mixing and agitation where stresses generated within the flow are used to break apart an immiscible mixture into small droplets. The size of the drops produced is determined by the strength of the flow as described by the capillary number. The capillary number is the ratio of the viscous to interfacial/surface tension forces and is defined as

$$\mathrm{Ca} = \frac{\mu_C V}{\sigma} \tag{1.2}$$

where μ_c is the viscosity of the continuous phase of the system and σ is the interfacial tension between two immiscible fluids.

Many of techniques used to form bulk emulsions are "top-down" approaches to creating emulsions, involving breaking larger drops into smaller drops, allowing little control over the formation of individual droplets and resulting in a polydisperse range of droplet sizes. Microfluidics however offers a "bottom-up" method for droplet generation for use in emulsions, allowing for precise control over individual droplets and therefore

the creation of monodisperse and controlled polydisperse emulsions (Anna, Bontoux et al. 2003).

Pickering is famous for laying the ground work on emulsions in his 1907 paper (Pickering 1907), by noting that soap helps to stabilize emulsions. In 1932 G. I. Taylor extended Einstein's work on how solid particles in a suspension affect liquid viscosity to how liquid particles with deformable interfaces affect emulsion viscosity (Taylor 1932). This work made three assumptions about emulsions: 1) that the drops were so small they would remain spherical under surface tension and viscous forces; 2) a no-slip boundary condition at the surface of the drop; and 3) the tangential stress parallel to the drop surface continues all the way to the surface of the drop and is transmitted from one fluid to the other. Using these assumptions an equation for the viscosity of an emulsion was found to be

$$\mu_{eff} = \mu_c \left[1 + 2.5\Phi \left(\frac{\mu_d + \frac{2}{5}\mu_c}{\mu_d + \mu_c} \right) \right], \tag{1.3}$$

where μ_{eff} is the mean viscosity of the emulsion, Φ is the volume fraction of the fluid that the fluid spheres occupy, μ_d is the dispersed or droplet phase viscosity and μ_c is the continuous phase fluid viscosity. Einstein's original equation for the viscosity of a suspension of hard spherical particles in the dilute limit was

$$\mu^x = \mu\left[1 + 2.5\Phi\right] \tag{1.4}$$

As the particle concentration increases beyond the dilute limit, the particle-particle interactions produce long-range order resulting in non-Newtonian effects, such as shear thinning or shear thickening of the fluid viscosity (White, Chellamuthu et al. 2010).

1.2.1 Droplet Generation Using Microfluidics

Microfluidic devices can be used to make monodisperse emulsion droplets. The size of droplets produced by microfluidic devices is controlled by a combination of the method of droplet creation, the properties of the bulk and emulsified fluids, the flow rates used to drive the two fluids and method use to input fluid into the microfluidic device (Nie, Seo et al. 2008).

A variety of droplet creation methods have been employed within microfluidics devices to produce monodisperse droplets, including flow-focusing/co-flowing streams and T-junctions, as shown in Figure 1-1 (Thorsen, Roberts et al. 2001; Anna, Bontoux et al. 2003; Christopher and Anna 2007; Teh, Lin et al. 2008; Yeh, Lee et al. 2008; Abate, Poitzsch et al. 2009). These are all passive methods of droplet creation because they rely on the continuous phase flow to deform the interface and form droplets from interfacial instabilities rather than moving parts. Many of the methods used in industrial settings are not passive methods of droplet creation. Instead large blenders are generally used to produce an emulsion of polydisperse droplets. Each method of droplet production in microfluidic devices will be discussed further.

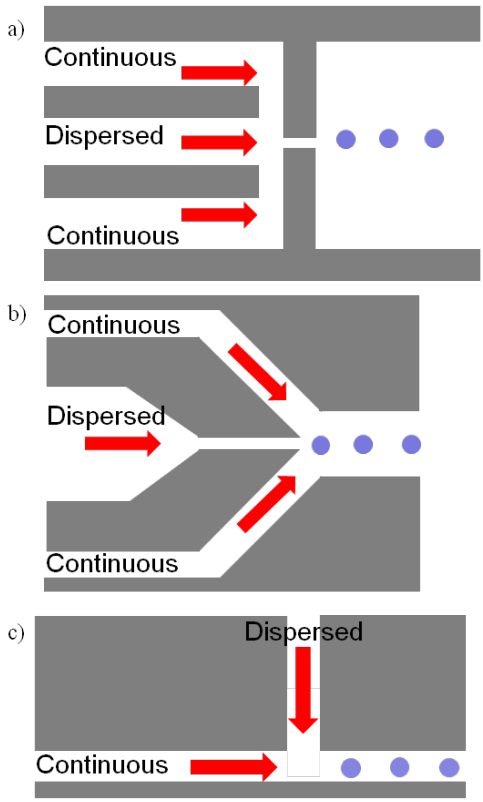

Figure 1-1: Three types of droplet producing flow cells. a) Flow-focusing b) Coflowing c) T-junction.

The geometry used to create droplets impacts the range of capillary numbers and flow rate ratios over which monodisperse drops can be produced (Abate, Poitzsch et al. 2009). For a fixed flow rate ratio, $Q_r = Q_c / Q_d$ of $Q_r = 1$ where Q_c is the continuous phase flow rate and Q_d is the dispersed phase flow rate, water drops in a fluorocarbon oil are produced by a T-junction up to a capillary number of $Ca \approx 1$. Flow-focusing devices produce droplets in the range of capillary numbers between $0.04 \le Ca \le 0.15$ (Abate, Poitzsch et al. 2009).

The use of syringe pumps and pressure are the most common methods for fluid input into microfluidic devices. In single phase flows these two methods are equivalent

to each other, however in multiphase flows these methods are not the same due to interface dynamics (Ward, Faivre et al. 2005). Syringe pump driven flow, as was used in all of the work discussed in this dissertation, provides a larger range of drop production frequency and drop velocities compared to pressure driven flows which allow for greater variety of drop size over a small range of pressures (Ward, Faivre et al. 2005).

1.2.2 Flow-Focusing Droplet Generation

Flow-focusing and co-flowing droplet generation techniques in microfluidics rely on the interplay of the shear/viscous and capillary/interfacial forces. A small jet of the dispersed phase fluid protrudes into the continuous phase fluid and is sheared by the continuous phase fluid. A droplet pinches off the jet when the viscous forces overcome the surface tension forces. The continuous phase is always a liquid; however the dispersed phase can be aqueous or gaseous, although less work deals with gas-liquid dispersions than with liquid-liquid emulsions in microfluidic devices. Generally it is not desirable for the dispersed phase to wet the walls of the device as this can cause droplets to stick to the walls.

The flow rate of both the continuous and dispersed phase fluid affects droplet formation (Anna, Bontoux et al. 2003). Anna *et al.* were able to produce monodisperse, bidisperse and polydisperse drops by adjusting the flow rates of the dispersed water phase and the continuous oil phase. Increasing the continuous phase flow rate, while holding the dispersed phase flow rate constant, led to a decrease in droplet size. Increasing the dispersed phase flow rate, while holding the continuous phase flow rate constant, also led

to a decrease in droplet size and eventually to the creation of bidisperse and polydisperse droplets (Anna, Bontoux et al. 2003).

Flow focusing devices have been used to create gas bubbles in a continuous liquid phase (Garstecki, Gitlin et al. 2004). By varying the continuous phase flow rate or the dispersed phase pressure bubble size and production frequency were varied. This is similar to how liquid-liquid droplet formation has been shown to behave. The volume of the gas bubbles formed was found to be proportional to the pressure applied to the gas inlet stream and inversely proportional to the product of the continuous phase flow rate and viscosity (Garstecki, Stone et al. 2005).

Microfluidic flow-focusing devices have been used to create monodisperse solid particles 20μm to 1000μm in diameter using in situ-polymerization of a liquid monomer in the system and by using a thermally set liquid (Xu, Nie et al. 2005). This increases the variety of materials spherical particles can be made from. Particle could also be controlled and varied from spherical using confinement downstream of droplet production resulting in rod and disc shaped particles (Xu, Nie et al. 2005). Microfluidic flow-focusing devices have even been used to encapsulate droplets inside other droplets thereby creating controlled double and triple emulsions (Chang and Su 2008).

It has also been shown that there are different modes of droplet production within microfluidic flow-focusing devices: geometry controlled breakup, dripping, jetting and thread formation (Anna, Bontoux et al. 2003). Geometry controlled breakup produces monodisperse droplets roughly the size of the orifice from which the dispersed phase finger protrudes. In this type of droplet creation the dispersed phase finger retracts after each droplet is pinched off. In the dripping mode of droplet formation droplets are

smaller than the orifice from which the dispersed phase finger protrudes and no dispersed phase finger retraction occurs. In jetting, the droplet size is more polydisperse and droplets are larger than those produced by dripping. In the thread formation regime the main droplets are on the order of the size of the orifice, but after each droplet pinches off a thread of significantly smaller, polydisperse droplets trails behind until the next large droplet forms. The transition between each of these droplet formation regimes depends on the viscosity ratio, $\lambda = \mu_d / \mu_c$, and the capillary number (Anna, Bontoux et al. 2003).

Control over droplet size and droplet creation frequency can be achieved within in a microfluidic flow-focusing device using valves (Abate, Romanowsky et al. 2009). Valves were used to change the size of the orifice downstream of the flow-focusing region used to create droplets, allowing for on demand adjustment of droplet size without changing the fluid flow rate. Drop sizes were varied between 7μm and 200μm (Abate, Romanowsky et al. 2009). Valves which regulated the width of the continuous oil phase inlets were used to regulate frequency of the droplet production (Abate, Romanowsky et al. 2009). When the valves were actuated droplet production frequency increased.

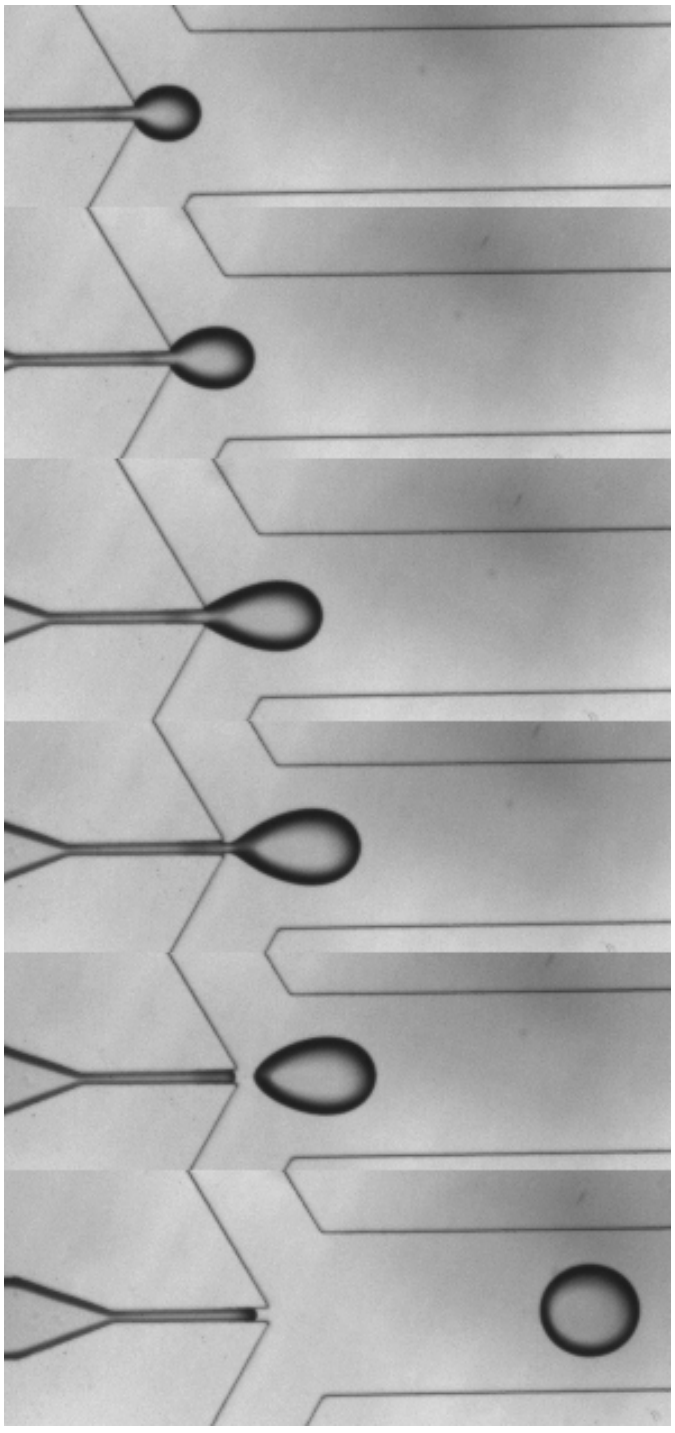

Figure 1-2: The process of droplet formation for a flow focusing device.

Shown in Figure 1-2 is the process of droplet formation using a flow focusing device. A droplet forms at the end of the channel containing the dispersed phase fluid and the droplet grows until it pinches off, which results from the interplay between the viscous and interfacial forces. After pinch off the dispersed phase neck recedes into the dispersed phase channel. When the next droplet forms the neck will push out into the continuous phase and the process will repeat itself.

1.2.3 T-Junction Droplet Generation

The shearing cross flow of a continuous phase fluid past a T-junction where a dispersed phase fluid is introduced has been shown to be a simple and effective method of creating stable and monodisperse droplets for a variety of fluid systems (Nisisako, Torii et al. 2002; Hillborg, Tomczak et al. 2004; Husny and Cooper-White 2006). T-junction droplet production occurs when the dispersed phase enters the continuous phase and a neck of the dispersed phase is pulled and thinned by the continuous phase fluid. Evenetually the viscous forces of the continuous phase overcome the surface tension of the dispersed phase and a drop breaks off the neck. There are two regimes for droplet formation in T-Junction microfluidic devices, squeezing and dripping. Experimentally squeezing was determined to occur at $Ca \leq 10^{-2}$ and dripping at $Ca \geq 10^{-2}$ (Garstecki, Fuerstman et al. 2006). However, using two-dimensional simulations the transition between squeezing and dripping was found more exactly to be at $Ca = 0.018$ and the transition point is independent of flow rate ratio, Q_r, and viscosity ratio, λ (Liu and Zhang 2009). In the squeezing regime, droplet breakup is dominated by pressure drop. The pressure drop results from the dispersed phase fluid obstructing the main channel. In the

dripping regime droplet formation occurs due to shear stresses which shear drops from the dispersed phase finger. Droplet size, in the squeezing regime, is dependent upon the flow rate ratio and the capillary number. For the dripping regime droplet size is dependent upon the viscosity ratio of the system.

The first work done on water-in-oil emulsions formed in T-junction microfluidic devices was done by Thorsen *et al*. (Thorsen, Roberts et al. 2001), who found that droplet size and production frequency were controlled by the relative pressure of the water and oil phases. Thorsen *et al*. (Thorsen, Roberts et al. 2001) found that when the water pressure was greater than the oil pressure the droplets could be organized into patterns ranging from "pearl necklaces" to zigzag patterns to layers of droplets. Garstecki *et al.* (Garstecki, Fuerstman et al. 2006) extended this work to look at the mechanism of drop formation, as mentioned above, for both liquid-liquid systems and gas-liquid systems.

1.3 Drop Deformation

The interfaces of droplets are mobile and deformable, unlike those of solid particles in suspensions. There are several important factors in defining drop deformation and breakup. Generally the deformation of an initially spherical droplet is modeled as an ellipse, Figure 1-3, and the deformation is quantified with the dimensionless parameter D, defined as

$$D = \frac{a-b}{a+b}, \tag{1.5}$$

where a is half the major axis of the ellipse and b is half the minor axis of the ellipse and $a=b$ in the case of an undeformed spherical drop, and therefore $D=0$.

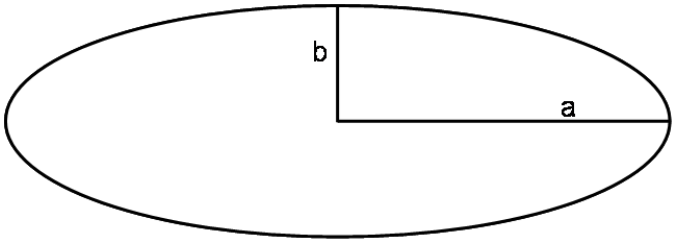

Figure 1-3: Relevant dimensions of an ellipse. An ellipse is generally used as the model for droplet deformation as they are generally viewed as two dimensional.

Taylor began the exploration of the deformation of droplets in emulsions with his 1934 paper (Taylor 1934). Taylor motivated his work by saying, "any movement of the outer fluid (apart from pure rotation or translation) will distort the drop owing to the dynamical and viscous forces which then act on its surface. Surface tension, however, will tend to keep the drop spherical" (Taylor 1934). Using a four-roll mill and parallel band apparatus Taylor was able to deform drops in well defined and controlled flows. The four roll mill produced a pure extensional flow which stretched the drops. As the capillary number increased, the deformation increased and in the case of high viscosity ratios, some drops broke into smaller drops. The parallel band shear cell apparatus was used to produce shear flows, where a higher viscosity ratio lead to greater droplet deformation. However for extensional and shear flows increasing the dispersed phase viscosity lead to a decrease in the speed, capillary number, needed for droplet breakup to occur (Taylor 1934).

There is a critical capillary number for idealized flows that will determine when a drop will transition from steady deformation to break up based on the viscosity ratio of the continuous and dispersed phase fluids. According to Bentley et al. (Bentley and Leal 1986) this number varies between $0.25 \geq Ca_{cr} \geq 0.1$ for viscosity ratios ranging from

$10^{-3} \le \lambda \le 10^{2}$ for irrotational flows. It holds constant for $\lambda \ge 3$ at $Ca_{cr} = 0.1$. For pure extensional flows the critical capillary number for droplet break up is much higher, with $0.58 \ge Ca_{cr} \ge 0.35$, over the same range of viscosity ratios as the irrotational flows. However, the extensional flow hits a minimum of $Ca_{cr} = 0.31$ at $\lambda = 1$. This experimental work agreed well with the predictions of small deformation theory for $\lambda \ge 0.05$ (Bentley and Leal 1986).

Geometrical or passice droplet breakup can be achieved within a microfluidic device using T-junctions and obstacles in the flow (Link, Anna et al. 2004). This method of passively breaking larger parent droplets into smaller daughter droplets allows for the precise control over the daughter droplet size distribution. The T-junction method for breakin large drops into smaller daughter droplets gave the maximum precision for droplet breakup when compared to flow past an obstacle. The smallest size daughter droplets, which could be achieved, were limited by the smallest channel width designed into the device. Placement of the perpendicular leg of the T-junction at the center of the channel of offsetting the perpendicular leg closer to one side of the channel than the other allowed for the production of monodisperse (centrally located leg), bidisperse (offset) and polydisprse droplet size distributions. The capillary number for breaking drops increased with decreasing extension rates (Link, Anna et al. 2004). When a single stream of droplets with sizes on the order of the channel width encounters an obstacle in the center of the channel the parent droplet breaks into two smaller droplets of nearly the same size. However, when the obstacle is offset in the channel a bidisperse set of droplets is created. More complicated droplet breakup dynamics occur for layers of droplets encountering an obstacle within a channel (Link, Anna et al. 2004).

A number of methods of active and passive droplet deformation have been demonstrated in the literature, the study of individual droplet deformation in extensional flow and mixed shear and extensional flows is still an open question in the literature. The study of droplet deformation in under mixed shear and extensional flow conditions that are the result of confinement effects is also an open question. Confinement is used as a first approximation of the droplet interactions in a stabilized concentrated emulsion.

1.4 Particle and Surfactant Covered Droplets

Emulsion droplets need to be stabilized against coalescence. This can be achieved with surfactants and colloidal particles. When using surfactants as stabilizers, droplet coalescence is prevented by the repulsive interaction between the surfactants on the surface of the droplets (Baret, Kleinschmidt et al. 2009). Particles stabilize droplets against coalescence by adsorbing at the droplet interface or by forming a 3D network of particles in the continuous phase and surrounding the droplet (Binks 2002). The network of particles formed on or around the outside of a fluid droplet can form an elastic membrane as will be discussed on Chapter 4.

Surfactants are composed of a hydrophilic head group and a hydrophobic tail group. Adding surfactants to the solution acts to stabilize the droplet interface against coalescence, but also reduces the surface tension between the droplet and continuous phases of the emulsion, thereby reduces the work required to create the interface between the two immiscible fluids (Eggleton, Tsai et al. 2001). Surfactants can aid in droplet creation within a microfluidic device because of the reduction in interfacial tension

between the two phases. Surfactants lead to the phenomenon of tip streaming as discussed in (Milliken, Stone et al. 1993; Anna and Mayer 2006).

Tip streaming occurs for liquid-liquid systems where surfactants are present at the liquid-liquid interface. This phenomenon can occur on the surface of drops or jets coming out of an orifice into the flow of another fluid. Surfactants adsorb and desorb onto the interface between the continuous and dispersed phase. The reduction in surface tension caused by the surfactant is generally uniform across the entire interface. However, when an elongational flow stretches the surfactant laden fluid-fluid interface surfactant concentration gradients appear along the interface particularly near a pole on a drop or at the tip of a jet. The surfactants are swept along the interface by the extensional flow to the poles. The surfactant cannot desorb fast enough to prevent the surfactant concentration from becoming large. This large surfactant concentration gradient leads to a local reduction in interfacial tension and causes a highly curved tip to form at the end of the jet/drop of fluid. This highly curved tip is pulled into a thin thread, which breaks into tiny surfactant laden droplets (Anna and Mayer 2006).

There have been numerous studies on the effects surfactants have on system stabilization (Stone and Leal 1990; Edmond, Schofield et al. 2006) and on drop deformation (Stone and Leal 1990; Milliken, Stone et al. 1993). As the surfactant concentration is increased drop stability against coalescence is also increased due to the repulsive interaction between the surfactants (Baret, Kleinschmidt et al. 2009).

Pickering is credited with demonstrating that particles can stabilize emulsions by showing that particles which are wet more by water than oil could effectively stabilize oil in water emulsions by residing at the interface of the droplets (Pickering 1907). A

particle's ability to stabilize an emulsion not only depends on the particles wettabilty, as shown by Pickering, but it also depends on the particle shape, concentration and inter-particle interactions. For spherical particles, with a radius on the order of a few microns, the energy needed to remove a particle from the interface between the two phases is

$$U = \pi r_p^2 \sigma (1 \pm \cos\theta)^2 \tag{1.6}$$

where U is the energy needed to remove the particle from the interface into one of the two fluid phases, r_p is the radius of the particle, the positive sign corresponds to removal of the particle into oil and the minus is for the removal of the particle into water (Binks and Lumsdon 1999). We are looking to move a particle with a radius of $r_p = 5 \times 10^{-8}$ m from oil into water. The interfacial tension of the system is $\sigma = 5x10^{-3}$ N/m. For a particle with a wettability of $\theta = 90^\circ$, the energy required to remove the particle from oil and into water is $U = 9554$ kT, where k is the Boltzmann constant. As θ goes to zero, U decreases and at $\theta = 10^\circ$, $U = 145$ kT. As θ approaches 180°, U increases. At $\theta = 180^\circ$, the energy to remove the particle increases to $U = 19{,}109$ kT and for comparison at $U = 160^\circ$ the energy for particle removal is $U = 18{,}533$ kT. It can be seen that the wettability of the particle has a large influence on how easily it can be moved between phases. A hydrophilic particle ($\theta \leq 90^\circ$) is easy to remove from the oil phase into the water phase, as the energy required to do so is two orders of magnitude less than the energy required to move the particle from the water phase into the oil phase. It is interesting to note that particle stabilization was exploited by the food industry, even before the dynamics of particle stabilization were well understood, by the use of ice crystals in ice cream and fat particles in whipping cream (Binks 2002).

Figure 1-4: Fully constructed microfluidic drop making device.

1.5 Device Fabrication

Early microfluidic devices were fabricated using the technology from the microelectronics industry- photolithography and etching of silicon and glass. While this technology was a good starting point, it was costly, required the use of a cleanroom for every step, was time and labor intensive, and optical detection methods could not be used to view the microfluidic systems because silicon does not transmit light. Instead of using the conventional methods employed in making microelectronics system, most microfluidic devices are now made using the process of rapid prototyping, which involves the creation of a silicon master wafer in the cleanroom and the creation of devices outside the cleanroom using elastomeric polymers (Duffy, McDonald et al. 1998; McDonald, Duffy et al. 2000; McDonald and Whitesides 2002). A series of devices created using rapid prototyping can be seen in Figure 1-4. The process of device creation is a multistep process that will be described in detail in the next few sections of this chapter.

1.5.1 Photolithography

Photolithography, the most widely used lithographic technique, is the process by which silicon master wafers are created for the rapid prototyping of microfluidic devices (Madou 2002). In photolithography, used for the development of microfluidic devices, the flow cell design is transferred from a mask to a silicon wafer coated with photoresist. Photoresist is a light sensitive material used to form a patterned coating on a surface. UV light is shown through a mask to transfer the flow cell design to the photo resist. Two types of masks are generally used, either a chrome mask or a transparency mask. Chrome masks are advantageous because they can have features as small as a few hundred nanometers, however they are very expensive. In cases where numerous design iterations are needed before a final design is chosen chrome masks can be cost prohibitive. The printing of masks on transparencies is much cheaper, but resolution is limited to 10s of microns. This is the most commonly used technique in microfluidics as these masks can be obtained in a matter of hours or days, as opposed to weeks or months for chrome masks. In addition the printed masks are relatively cheap, making it possible to go through numerous design iterations in the research and development process (McDonald, Duffy et al. 2000).

Figure 1-5 is a pictorial representation the process of photolithography. Starting from the top, we have UV light shown through a mask. The mask is aligned with the silicon wafer using a mask aligner. The UV light passes through the mask hitting the wafer surface and transferring the pattern to the resist. If the resist is positive, resist exposed to light will be removed in the development stage, leading to a direct transfer of the image on the mask to the wafer. For a negative resist, resist which is not exposed to

UV light is removed in the development process, resulting in a negative transfer of the mask. After exposure the wafers are developed and ready for use as master wafers in the softlithography step of device fabrication.

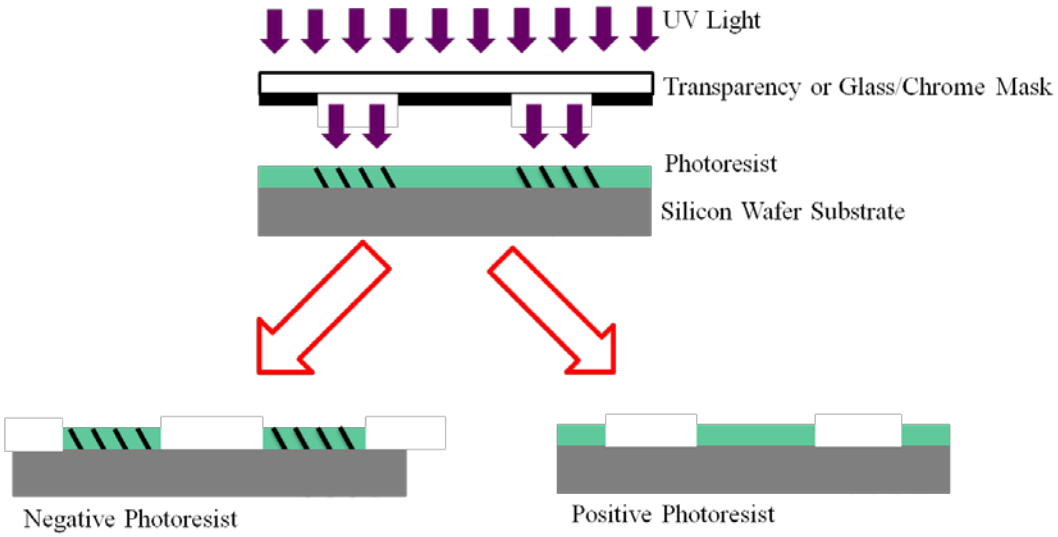

Figure 1-5: Pictorial representation of the process of photolighogaphy.

1.5.2 Photoresist

For the process of creating microfluidic devices, we use a negative photoresist, called SU8 (MircoChem Corporation) to create the master slide for rapid prototyping of microfluidic devices. This SU8 master is very durable and can be used to cast numerous molds. The most common failures occur when the wafer is broken by the user or the photoresist releases from the wafer (Anderson, Chiu et al. 2000). This process is called rapid prototyping, because the creation of the master slide is the only step which requires a cleanroom, thereby greatly reducing the time and cost to fabricate a microfluidic device, as well as allowing numerous devices to be made from each master wafer (Duffy, McDonald et al. 1998; McDonald, Duffy et al. 2000).

SU8 comes in several different formulations depending upon the desired thickness of resist which directly corresponds to device height. The step by step process of creating a master wafer will be explained based on the assumption that SU8-100 is being used. The resist is deposited onto the wafer via spin coating. The wafer is accelerated to 500 rpm at a rate of 100 rpm/sec and held there for 10 seconds, and then it is accelerated to 2000 rpm at 300 rpm/sec for 30 seconds to achieve a resist thickness of approximately 150 μm. Next, the wafer is pre-exposure baked at 65˚C for 20 minutes and at 95˚C for an additional 50 minutes. Next the wafer is exposed to UV light. Exposure time is based on SU8 thickness and UV lamp age, as the intensity of the lamp changes over time. After exposure, the wafer is post-exposure baked for 1 minute at 65˚C and then for 12 minutes at 95˚C. Following the post exposure bake the wafer is developed.

1.5.3 Softllithography

After the creation of the SU8 master, the remainder of the microfluidic device is made using soft lithographic techniques, represented pictorially in Figure 1-6.

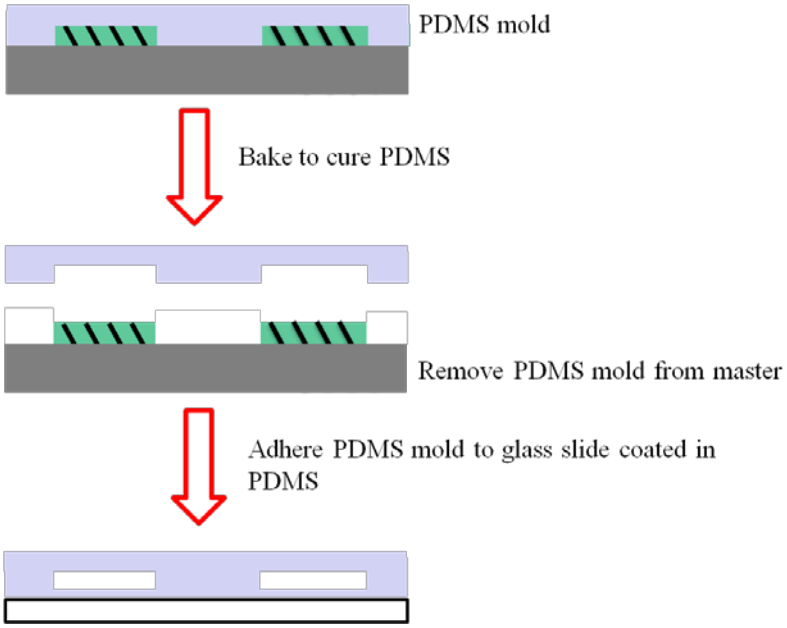

Figure 1-6: Pictorial representation of the process of softlithography.

First poly(dimethyl)-silonxane (PDMS, Dow Sylguard 184), the properties of which will be discussed later, is mixed in a 10:1 ratio of elastomer to curing agent. This mixture is degassed and then poured over the master wafer. The PDMS covered wafer is then baked at 60°C for 1 hour or until nearly hard. The PDMS molds are cut and removed from the wafer. This process creates a negative of the master wafer, meaning there are indents in the PDMS where there are raised spots on the master wafer. Inlet and outlet holes are punch, so that syringe tips and tubing can be inserted later for fluid input and output.

The final step in device fabrication is the sealing of the device. PDMS is spun onto a glass slide, however this time the PDMS is mixed in a 5:1 ratio. This higher ratio allows there to be extra curing agent, which creates an irreversible seal between the PDMS on the glass and the PDMS mold of the microfluidic device created from the master wafer. This bond cannot be distinguished from the physical properties of bulk

PDMS (McDonald and Whitesides 2002). The PDMS coated glass is then put in an oven at 60˚C for 1 hour, after which the PDMS molds of the microfluidic device are put into contact with the PDMS coated glass and left to cure overnight in a 60˚C oven.

PDMS microfluidic devices can also be sealed to PDMS or glass using oxygen plasma. However this is a reversible seal, so it cannot withstand as high a pressure as the irreversible PDMS ratio mismatch method of sealing and it requires more costly equipment (McDonald, Duffy et al. 2000).

1.5.4 Poly(dimethyl)-siloxane

The goal is to be able to create many devices cheaply and quickly and this is acheived through rapid prototyping – the process of lithography, softlithography and device sealing. Most microfluidic devices are created out of poly(dimethyl)-siloxane (PDMS) because it is an inexpensive and easily molded polymer (McDonald and Whitesides 2002). PDMS is polymerized at low temperatures and its elasticity allows it to be easily pulled off the SU8 master wafers without damaging the master wafer. It's other advantages include that it is optically transparent, it is biologically inert, and it is gas permeable (Makamba, Kim et al. 2003).

A few of the disadvantages include that PDMS, by nature is hydrophobic, therefore without surface modification it is difficult to fill a channel with an aqueous solution. This also proves to make the creation of oil in water emulsions difficult. PDMS swells when contacted by strong organic solvents.

1.5.5 Surface Modification of PDMS

There are a variety of different methods that can be used to modify the surface of PDMS and make it hydrophilic or even more hydrophobic. The measurement of the contact angle between water and a solid surface can be used to determine how hydrophilic or hydrophobic a surface is. A contact angle of 0° would be indicative of a perfectly hydrophilic surface and a contact angle of 90° is where surfaces transition from hydrophilic to hydrophobic. A contact angle of greater than 150° is termed a superhydrophobic surface. As discussed, one the disadvantages of using PDMS for microfluidic devices is that it is hydrophobic, naturally having a contact angle of about 109° with water (Hu, Ren et al. 2002).

There are a variety of ways to modify PDMS and make it hydrophilic so that aqueous solutions can be tested in microfluidic devices made of PDMS, including exposure to oxygen plasma, UV radiation, corona discharge, deposition of a surfactant layer and radiation induced graft polymerization. The process of exposing PDMS to energy sources, such as oxygen plasma, is generally a reversible means of making PDMS hydrophilic (Makamba, Kim et al. 2003). Exposure over time to air and heat can revert PDMS to its natural hydrophobic state after plasma treatment (Hu, Ren et al. 2004).

The exposure of PDMS to plasmas, corona discharges and UV radiation leads to the oxidation of PDMS and temporary hydrophilicity. Hillborg et al. used a UV/ozone cleaner to build a layer of SiOx, which forms gradually but increases in depth with an increase in exposure to UV/ozone (Hillborg, Tomczak et al. 2004). The silica like layer is hydrophilic and between 7 and 160nm deep depending upon exposure time. After 60 min of exposure to the UV/ozone the advancing and receding contact angles were

reported to be 28˚±2˚ and 21˚±4˚ respectively (Hillborg, Tomczak et al. 2004). The difference between the advancing and receding contact angles is referred to as contact angle hysteresis.

UV induced graft polymerization has been extensively studied by Hu et al. (Hu, Ren et al. 2002) as a means to permanently modify PDMS and make it hydrophilic. Contact angles between the water and graft polymerized PDMS have been shown to be as low as 45˚ (Hu, Ren et al. 2002). Oxidized PDMS can have contact angles as low as 15˚, however this is a reversible process (Hu, Ren et al. 2004). For graft polymerization the two pieces of the unsealed micro devices are immersed in an aqueous solution of NaIO4 (0.5 mM), benzyl alcohol (0.5 wt%) and one of 5 monomers. The PDMS in solution was then exposed to UV light, after exposure the samples were rinsed for 24 hours in distilled water to remove any excess monomer. In this particular work the most effective monomer used was acrylic acid (AA), which made the contact angle between water and modified PDMS 45˚ (Hu, Ren et al. 2002). Next Hu et al, decided to try mixing neutral monomers with both a negative (AA) monomer and a positive monomer (2-methacryloxyethyltrimethylammonium chloride, MATC) The same solution and exposure process were used as in (Hu, Ren et al. 2002) work, however this time a variety of different neutral monomers were added to the NaIO4, benzyl alcohol, AA or MATC mixtures. The results found that both the neutral and charged monomers were grafted to the surface as the results for the mixtures were between those for the AA only and the neutral monomers (Hu, Ren et al. 2004).

UV induced graft polymerization has also been done within assembled microchannels. When the previous method of using AA, NaIO4 and benzyl alcohol was

used a gel formed in the channel after UV light exposure which caused clogging and numerous other problems within the flow cells. So a two step process was developed. First the flow cell rinsed with a solution of benzophenone, a photoinitiator, then rinsed with water, filled with the monomer solution and exposed to UV light for 5 minutes. The use of the photoinitiator also decreased UV light exposure time to 5 minutes from 3.5 hours (Hu, Ren et al. 2004). This two step method for creating a hydrophilic flow cell after assembly was also used to selectively pattern a microchannel so that some parts were hydrophilic and other parts maintained their natural hydropobicity (Wang, Lai et al. 2005). These patterned microchannels where used as a new way to fuse droplets within a microfluidic device (Fidalgo, Abell et al. 2007). This is a unique approach to the fusion of aqueous droplets because the droplets get "caught" in the hydrophilic stripes, mix and breakoff into new monodisperse droplets when the viscous drag forces overcome the surface energy forces. The droplet size can be controlled by the flow rate of the outer fluid, which wets most of the microchannel. This method also does not require the precise synchronization of droplet formation and movement within a microchannel, thereby allowing for easier drop fusion. Drop fusion is highly studied as it can be used to make microreactors.

1.6 Contributions

This dissertation is a compilation of experimental work performed on several different topics with a unifying foundation in microfluidics and microfluidic droplet production and deformation. A number of significant scientific discoveries were made through the research discussed in this dissertation. This first chapter looked to introduce

the reader to the necessary background which motivated the experimental work discussed in the remaining chapters of this dissertation. The remaining chapters will better highlight and discuss the scientific discoveries made throughout my research career as a PhD candidate.

In Chapter 2, the deformation of individual water droplets in extensional and mixed extensional and shear flows within a microfluidic device is discussed. Using a microfluidic flow-focusing device and a hyperbolic contraction downstream of the droplet generator, droplet deformation was explored on the individual droplet level. The smallest droplets studied only experienced extensional flows. For the larger droplets, confinement from the walls of the microfluidic device added shear to the droplets. It was found that droplet deformation did not agree with the Maffetone and Minale model for unconfined-droplet deformation, even for the least confined droplets, thus showing that droplet confinement plays a significant role in water droplet deformation even for minimally confined droplets. This work was published in the journal *Physics of Fluids* (Mulligan and Rothstein 2011).

In Chapter 3, the deformation of surfactant solution droplets in extensional and mixed extensional and shear flows is investigated. Surfactants are commonly used to stabilize emulsion droplets against coalescence; however the surfactants also decrease the interfacial tension between the dispersed and continuous phases, resulting in some interesting droplet deformation dynamics. In this case the most minimally confined droplets agreed with the Maffetone and Minale model for the deformation of unconfined droplets. However, for the nearly-fully-confined and fully-confined droplets studied the droplets deformed shape changed with increasing capillary number, which caused the

droplets deformation to vary significantly from that predicted by the Maffetone and Minale model. Droplets were found to transition from an elliptical shape, to a bullet-like shape, to a rocket-ship-like shape and eventually to streaming tails of daughter droplets from the trailing edge of the deformed droplet. The formation of tails was found to depend on the mobility of the surfactant used. This work was published in the journal *Physics of Fluids* (Mulligan and Rothstein 2011).

Chapter 4 continues the study of droplet deformation by looking at particle-coated droplets using 1μm and 500nm amine modified silica particles which populate the oil-water interface. Particles are another commonly used stabilizer in emulsions. Emulsions stabilized by particles are generally called Pickering emulsions. Particle coated droplet deformation was found to deviate from the Maffetone and Minale model for droplet deformation. Droplets coated in 1μm amine modified particles were found to stream tails from the rear of the droplet, but only in the case of fully confined droplets. Trailing behind these deformed fully-confined droplets were buckled and crumpled daughter droplets. This work was published in the journal *Langmuir* (Mulligan and Rothstein 2011).

Chapter 5 discusses the process of scaling-up microfluidic devices to produce droplets in multiple flow-focusing devices in parallel on a single chip. A single inlet was used for the continuous and dispersed phase fluids. Each of the parallel flow-focusing devices has its own exit tubing. The length of the exit tubing can be adjusted in order to control droplet size and production frequency. By using parallel droplet production a higher output of droplets can be realized, thus moving this well understood technology

for producing droplets with precise control over droplet size one step closer to use in industry.

CHAPTER 2

DEFORMATION OF WATER DROPLETS IN EXTENSIONAL FLOWS

A series of experiments were performed where droplets of deionized water were generated in oil using a microfluidic flow-focusing device. The morphological development of the droplets in extensional flow and confinement-induced shear flow at various extension rates was studied using a hyperbolic contraction. This novel approach to droplet deformation within a microfluidic device allowed for the probing of droplets within a nearly uniform extensional flow and mixed extensional and shear flow conditions. Mixed extensional and shear flow conditions resulted from the droplets becoming confined within the channel. The focus of this work was to study the effect of confinement-induced shear on droplet deformation and breakup in extensional flows. Droplet deformation was found to increase with both increasing capillary number and increasing confinement, for a fixed viscosity ratio of $\lambda = 0.1$. Droplet deformation was found to vary from the predictions of theory at all capillary numbers and confinements studied.

2.1 Water Droplet Deformation

Understanding the deformation and breakup of water droplets under flow has been a topic of great interest since Taylor's seminal experiments (Taylor 1934) and a number of excellent reviews exist in the recent literature (Olbricht 1996; van Puyvelde, Vananroye et al. 2008).

The critical capillary number for droplet breakup has been shown to be a function of both the character of the flow (shear or extension) as well as the viscosity ratio, $\lambda = \eta_d / \eta_c$. Here η_d is the viscosity of the dispersed phase. The critical capillary number has been found to be significantly smaller in extensional flows than in shear flow with the result that at the same deformation rate, smaller droplets can be produced in extensional flows (Bentley and Leal 1986). It should be stressed, however, that creating emulsions in this way typically results in a wide distribution of drop sizes. In many applications, control over both the size and the size distribution of such droplets is the critical element in such emulsions (Anna, Bontoux et al. 2003). Recent work has shown that emulsions with nearly monodisperse droplet size distributions can be produced using microfluidic devices (Christopher and Anna 2007; Miller, Rotea et al. 2010).

Droplet deformation and breakup is governed by the capillary number and the interplay between the viscous and surface forces. When the capillary number is large, viscous forces dominate and the initially spherical droplet becomes ellipsoidal and eventually breaks into smaller droplets. Conversely at low capillary numbers, surface forces dominate and the drop remains spherical. In addition to the studies on individual droplets in shear and extensional flows, extensive work has been to study how shear flow affects polydisperse bulk emulsions. For polydisperse emulsions, the capillary number experienced by each droplet will vary. Migler (Migler 2001) used the shear flow between two rotating parallel disks to study the effect of shear and confinement on drop deformation and flow induced structure in polydisperse emulsions during droplet coalescence. High shear rates were initially used to produce a high concentration of water droplets in oil. At a fixed gap between the disks, a number of distinct transitions

were observed as the shear rate was progressively decreased; smaller droplets coalesced into larger droplets, which aligned due to flow into pearl necklace like structures and finally to strings of the dispersed phase fluid. It was also shown that similar transitions were obtained by maintaining a fixed shear rate and decreasing the gap between the plates as the degree of confinement was increased. The string to droplet transition was also seen over a range of viscosity ratios, $0.1 \le \lambda \le 10,$ and in the case of both a Newtonian and highly elastic continuous phase fluid (Migler 2001).

Vananroye *et al.* (Vananroye, Van Puyvelde et al. 2007) looked at how a confinement of less than one affects the dynamics of single droplet breakup in shear flows for clean droplets. Using a counter rotating parallel plate flow cell with a constant gap between the plates of 1000 μm, drops ranging in diameter from $160 \le D \le 800$ μm were injected into the matrix fluid individually and sheared over the range of capillary numbers from $0.0 \le Ca \le 0.5$. Confinement is defined as

$$C = \frac{R}{w_2}, \tag{2.1}$$

where w_2 is the half width of the gap the droplet is confined in. For droplets with a confinement of C=0.8, droplet deformation was enhanced for all viscosity ratios, $0.31 \le \lambda \le 2.03$. For droplets with a confinement of C=0.2, over the same range of viscosity ratios, droplet deformation was found to match the predictions of the Maffetone and Minale model. In the work of Pathak *et al*., (Pathak and Migler 2003) droplets which were strongly confined were found to have deformation enhanced and droplet breakup suppressed by confinement for a viscosity ratio of λ=1.

The confinement of droplets can also be exploited to enhance or suppress the breakup of droplets. For an unconfined droplet, the critical capillary number for droplet breakup is dependent on the viscosity ratio of the two fluids (Bentley and Leal 1986). This transition from stable drop to breakup is the result of the imbalance of viscous and interfacial forces (Fischer, Plummer et al. 2007). For extensional flows the critical capillary number for breakup for unconfined droplets varies from $0.25 \geq Ca_{cr} \geq 0.1$ for viscosity ratios of $10^{-3} \leq \lambda \leq 10^{2}$ and then becomes constant for $\lambda = 3$ at $Ca_{cr} = 0.1$. For pure shear flows over the same range of viscosity ratios the critical capillary number is $0.35 \leq Ca_{cr} \leq 0.58$ (Bentley and Leal 1986). In work done by Vananroye *et al*., (Vananroye, Van Puyvelde et al. 2006) it was found that the critical capillary number for droplet breakup increased with increasing confinement for viscosity ratios of $\lambda<1$. However, for viscosity ratios of $\lambda>1$, an increase in droplet confinement lead to a decrease in the critical capillary number for droplet breakup.

As described above, much work has been done to study emulsions under shear flow conditions. Droplets within emulsions also often undergo extensional flows in their various industrial uses. For example, a nozzle is essentially an abrupt contraction placing extensional stresses on the fluid being passed through it. This set of experiments looks to explore how extensional flow affects droplet deformation under partial and full confinement using microfluidics on the single drop scale. Little work has been done to study droplets under an extensional flow in the presence of sidewall confinement. According to a recent review by Pipe and McKinley, (Pipe and McKinley 2009) work in microfluidics has included planar hyperbolic contractions like the one utilized here. These systems have been used to measure the extensional rheology of polymeric

solutions (Pipe and McKinley 2009) and as a preconditioner to stretch DNA molecules (Randall, Schultz et al. 2006). Additionally there have been a small number of studies where abrupt contractions were used to deform droplets. These contractions are easier to design and build; however, unlike hyperbolic contractions the droplets do not experience a uniform extension rate throughout the contraction and the comparison to previous unconfined four roll mill experiments cannot be made directly (Randall, Schultz et al. 2006; Oliveira, Alves et al. 2007; Pipe and McKinley 2009). Thus, there is still a gap in the fundamental understanding of the process of droplets deformation by extensional flows in complex fluids.

2.2 Water Droplet Deformation Experimental Details

2.2.1 Device Fabrication

The experimental flow cell is shown schematically in Figure 2-1a. The flow cell was designed with a flow focusing geometry to create a steady stream of monodisperse droplets followed by a hyperbolic contraction where droplet deformation and breakup can be measured as a function of extension rate and confinement. Devices were fabricated using standard soft lithography techniques (Anderson, Chiu et al. 2000; McDonald and Whitesides 2002). A computer aided design program, AutoCAD^{TM}, was used to design the microfluidic device. The design was then printed on a high-resolution transparency at 20,000 dpi, thus resulting in features as small as 10 μm. A negative photoresist, SU8 (MicroChem Corporation, Newton, MA), was used to create master wafers for rapid prototyping of the microfluidic devices with channel walls h=200μm deep (Anderson, Chiu et al. 2000). Microfluidic devices were then cast from the master wafer using

poly(dimethyl)-siloxane (PDMS, Dow Sylguard 184, Copley, OH). To seal the devices, standard glass microscope slides were spin-coated with a thin layer of PDMS and the molded devices were then bonded to the slides using a simple PDMS-ratio mismatch to provide uniform surface properties within the channels. More details of the specific fabrication procedure can be found in previous work (Rodd, Scott et al. 2005; Rodd, Cooper-White et al. 2007).

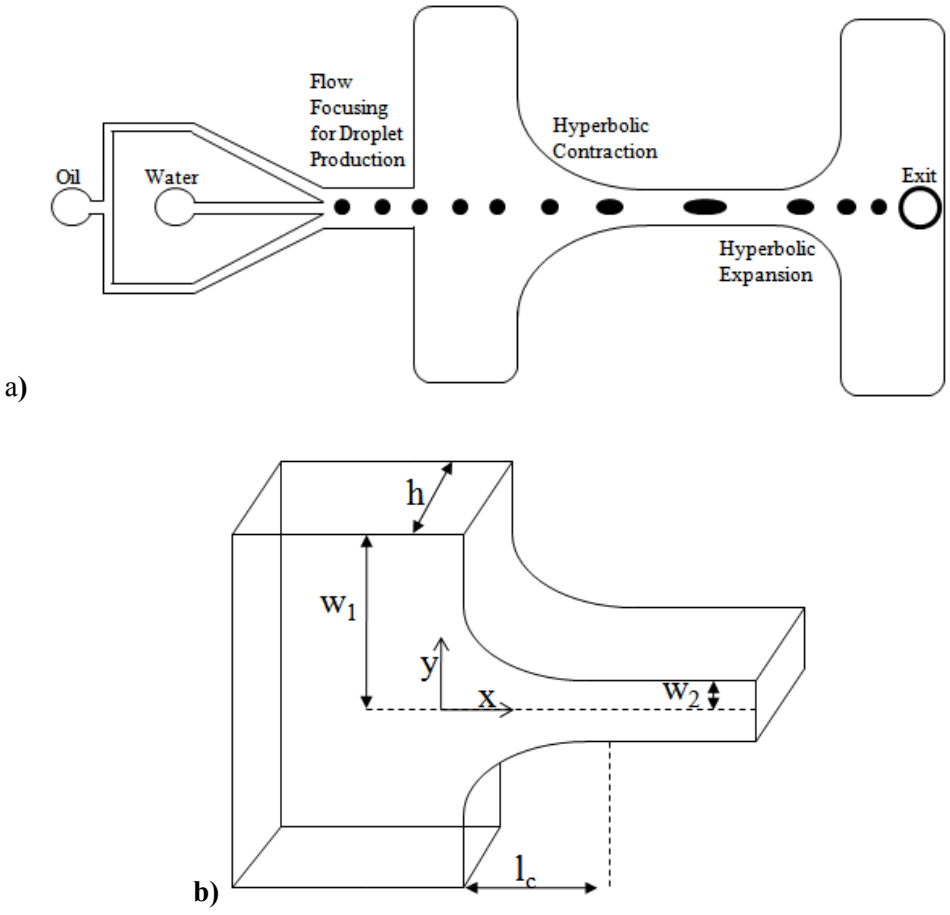

Figure 2-1: Schematic diagram of the flow cell used in these experiments. In (a) the entire flow cell is shown, including the hydrodynamic flow focusing region where droplets are produced and the hyperbolic contraction where they are stretched in a nearly constant extensional flow. In (b) the relevant dimensions of the hyperbolic contraction are shown.

2.2.2 Hyperbolic Contraction and Droplet Deformation

In order to investigate the deformation of droplets under an extensional flow and investigate the role of confinement on droplet deformation, a hyperbolic contraction was incorporated into the microfluidic device. A hyperbolic contraction was chosen because the fluid entering the contraction experiences a nearly constant extension rate within the contraction (Oliveira, Alves et al. 2007). Flow through a hyperbolic contraction has been used to measure the extensional rheology of polymeric fluids for more than thirty years by relating the measured pressure drop across the contraction to the flow rate (Everage and Ballman 1978; James and Chandler 1990; James and Chandler 1990; Pipe and McKinley 2009). More recently, the hyperbolic contraction extensional rheometer has been fabricated within microfluidic devices, which due to their small size can be used to probe the rheology of low viscosity fluids in the absence of inertial effects (Oliveira, Alves et al. 2007; Pipe and McKinley 2009) and stretch DNA (Randall, Schultz et al. 2006). A schematic diagram of the hyperbolic contraction used in these experiments with all the pertinent dimensions labeled is shown in Figure 2-1b. The position of the walls along the hyperbolic contractions is described by the following equation

$$y = \frac{c_1}{x + \frac{2c_1}{w_1}}, \tag{2.2}$$

where y is the vertical position within the channel, c_1 =0.025 mm^2 is a design parameter which dictates the strength of the extensional flow, x is the position along the length of the channel and w_1 = 3mm is the half-width of the channel before the contraction. The design parameter $c_1 = 1/2\, w_2 l_c$ can be related to the length of the contraction, l_c, and the final downstream half-width, w_2. The length of the contraction, l_c, was either 2mm or

1mm depending upon the value of the downstream half-width, which was taken as either w_2=25 μm or w_2=50 μm respectively. The narrower channel is called FC1 and the wider channel FC2 and all relevant channel dimensions are summarized in Table 2-1. The upstream half-width, w_1, was held constant for all flow cells at w_1=3mm. After reaching a minimum width, the contraction is extended for an additional 1.5 mm at a separation of $2w_2$, so that the effect of confinement on droplet breakup can be observed. The contraction is then re-expanded through a hyperbolic expansion designed to result in a compression rate which is ten times smaller than that of the contraction.

It should be noted that this ideal homogeneous extensional flow does not occur across the entire channel due to the presence of shear near the walls of the hyperbolic contraction. The shear rate is at a maximum at the walls of the channel and decreases to zero at the centerline. At the narrowest point in the hyperbolic contraction the shear rate at the wall can be as much as twice the extension rate, however, it decreases significantly at wider points of the contraction. Oliviera *et al*. (Oliveira, Alves et al. 2007) showed both experimentally and computationally that a nearly constant extension rate can still be achieved along the centerline of the hyperbolic contraction. In addition, they demonstrated that for over 80% of the channel width, the velocity is essentially constant and can be approximated by the plug flow approximation. In the absence of droplets, my own μ-PIV data were consistent with these findings. Thus shear will become increasingly important as the droplet confinement increases and the droplets approach the wall. Confinement is also important because it is a good first approximation of the flow environment experienced by droplets in a concentrated emulsion.

Table 2-1: The relevant dimensions for each type of flow cell used in the experiments

Type of Flow Cell	w_1 [μm]	w_2 [μm]	l_c [μm]
FC1	3000	25	2000
FC2	3000	50	1000

2.2.3 Experimental Methods

Flow through the microchannels was driven by two stepper-motor actuated micro-syringe pumps (New Era Pump Systems, NE-500 OEM, Wantagh, NY) using a 500 μl glass syringe (Hamilton, Microliter™ #750, Reno, NV) for the dispersed phase and a 10 mL plastic syringe (BD, plastic Leur-Lok Tip, Franklin Lakes, NJ) for the continuous phase. The syringe pumps impose a constant volumetric flow rate, Q, resulting in an average velocity within the channel that increases linearly with position along the length of the contraction,

$$u(x) = \frac{Q}{yh} = \frac{Q}{c_1 h}\left(x + \frac{2c_1}{w_1}\right). \tag{2.3}$$

Here h is the height of the channel and yh is the cross-sectional area at any given point in the channel. A more detailed solution of the spatially resolved velocity profiles requires numerical simulations and can be found in Oliveira *et al*. (Oliveira, Alves et al. 2007) The extension rate in the channel based on the average velocity in Equation 4 thus becomes

$$\dot{\varepsilon} = \frac{\partial u}{\partial x} = \frac{Q}{c_1 h}. \tag{2.4}$$

In our microfluidic device, a range of extension rates between $37s^{-1} < \dot{\varepsilon} < 2100s^{-1}$ were accessible. Additionally, the total Hencky strain imposed on the fluid can be determined from $\varepsilon = \ln(w_1 / w_2)$ which for our geometry is equal to $\varepsilon_{FC1} = 4.8$ and $\varepsilon_{FC2} = 4.1$. The

extension rate calculated from Equation 2.4 was thus used to recalculate an extensional capillary number as

$$Ca = \frac{\mu_c \dot{\varepsilon} R}{\sigma}. \tag{2.5}$$

All experiments were carried out on an inverted microscope (Nikon TE2000-U, Melville, NY) and video data was recorded using a high-speed video camera (Vision Research, Phantom 4.6, Wayne, NJ). The continuous phase fluid for all experiments was Migylol oil, which has a viscosity of μ_c=10 mPas (Migylol Oil 840, Sasol, Johannesburg, South Africa). The interfacial tension between Migylol oil 840 and water was characterized using a pendent drop experiment (Dataphysics, OCA 20, San Jose, CA) and found to be $\sigma = 19$ mN/m with the viscosity ratio fixed at λ=0.1.

The applied flow rate was varied, so that a range of extension rates and extensional capillary numbers could be accessed for the droplets as they entered the contraction. Droplet deformation was measured using ImageJ™ and quantified using the deformation parameter (Taylor 1934)

$$D = \frac{a-b}{a+b}, \tag{2.6}$$

where a is the length of the major axis of the ellipse formed when the drop is deformed and b is the length of the minor axis. Droplet deformation was measured as a function of the extensional capillary number and the amount of relative confinement of the drop. Not all droplets remain elliptical in shape.

2.3 Water Droplet Deformation Results and Discussion

Clean water droplets, deformed by extensional flows have increasing deformation with increasing extensional capillary number. In Figure 2-2a, the deformation parameter as a function of the extensional capillary number for various amounts of relative droplet confinement is shown. Without confinement, the critical capillary number for droplet breakup for a viscosity ratio of λ=0.1 is Ca_{cr}=0.19 (Bentley and Leal 1986). It can be seen in Figure 2-2a that the droplet deformation increases with increasing confinement over the entire range of capillary numbers studied for water droplets. In Figure 2-2a, the capillary number increases from $0.005 \leq Ca \leq 0.03$ as one moves from symbols near the bottom to the top at a given confinement. Even for the droplets with a confinement parameter of $C < 1$, significant deformations beyond the unconfined case predicted by droplet deformation models were observed. In order to try to understand the results from first principles and to help quantify the effects of confinement in these extensional flows, the predictions of the Maffettone and Minale model (Maffettone and Minale 1998) for droplet deformation in a homogeneous uniaxial extensional flow in the absence of confinement is superimposed over the data in Figure 2-2a (clean water droplets).

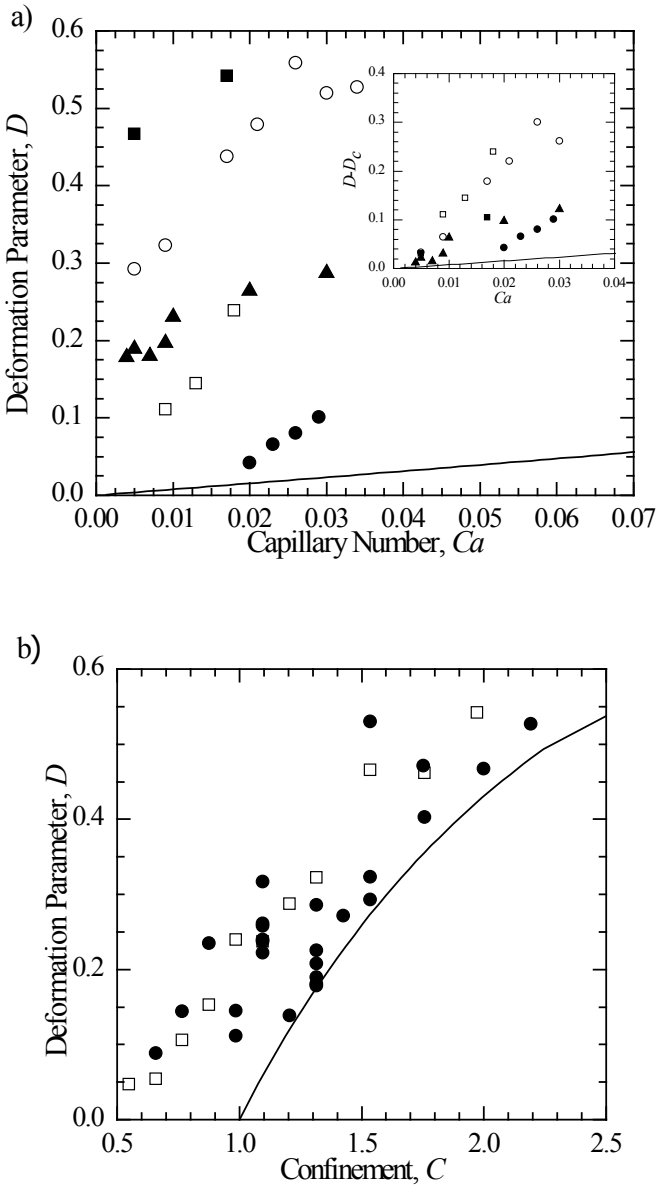

Figure 2-2: In (a) the deformation parameter as a function of the extensional capillary number is shown at various confinements for water drops in oil. The strength of the extensional flow is defined by the capillary number and the deformation parameter shows the deviation of a drop from a sphere. The data include confinement parameters at *C*=0.66 (●), *C*=0.99 (□), *C*=1.3 (▲), *C*=1.5 (○) and *C*=2.0 (■). The line represents predictions of the Maffetone and Minale model. (b) shows the deformation parameter as a function of the confinement for all capillary numbers studied (●). A capillary number of *Ca*=0.02 is shown by (□). The solid line shows the deformation parameter versus confinement at zero capillary number.

The Maffattone and Minale model (Maffettone and Minale 1998) was originally developed in order to determine droplet deformation resulting from an arbitrary flow around a droplet. The model makes two basic assumptions. First, that the droplet remains ellipsoidal at all time and second, that the drop does not break-up. It is thus only truly applicable in flows below the critical capillary number. The Maffattone and Minale model tracks the evolution of the drop shape tensor $\boldsymbol{S}$ through the following equation

$$\frac{d\boldsymbol{S}}{dt} - \boldsymbol{\Omega}\cdot\boldsymbol{S} + \boldsymbol{S}\cdot\boldsymbol{\Omega} = -\frac{f_1}{\tau}\left[\boldsymbol{S} - g(\boldsymbol{S})\boldsymbol{I}\right] + f_2\left(\boldsymbol{E}\cdot\boldsymbol{S} + \boldsymbol{S}\cdot\boldsymbol{E}\right). \tag{2.7}$$

The Eigenvalues of $\boldsymbol{S}$, $\lambda_{s,1}$ and $\lambda_{s,2}$, represent the square of the principal axis of the ellipsoid. Both f_1 and f_2 are empirical constants which are functions of the viscosity ratio, λ, and the capillary number, Ca, of the flow

$$\begin{aligned} f_1 &= \frac{40(\lambda+1)}{(2\lambda+3)(19\lambda+16)}, \\ f_2 &= \frac{5}{(2\lambda+3)} + \frac{3Ca^2}{2+6Ca^2}, \end{aligned} \tag{2.8}$$

while $\boldsymbol{E}$ is the shear rate tensor and $\boldsymbol{\Omega}$ is the vorticity tensor. To ensure conservation of drop volume, the variable g is defined as $g(\boldsymbol{S}) = 3III_s / II_s$ where II_s and III_s are the second and third invariants of the drop shape tensor $\boldsymbol{S}$ respectively.

Matlab was used to solve equation (2.7) for the extension rate and strain imposed during the flow through the hyperbolic contraction and calculated the resulting unconfined drop shape.

As expected, even in the presence of confinement, droplet deformation increases monotonically with increasing capillary number. However, as the confinement is increased, greater droplet deformation is observed at a given capillary number. In addition, the onset of deviations of the droplet deformation from predictions of the

Maffetone and Minale model occur at lower capillary numbers with increasing confinement. For the case of $C = 0.66$, the data deviates from the predictions of the Maffetone and Minale model at a capillary number of about $Ca = 0.016$. For $C = 1.0$, the deviation appears to occur just past the onset of flow at about $Ca = 0.01$. While for fully confined drops, $C > 1.0$, the data never follows the Maffetone and Minale model. We also see that the slope of the line for deformation versus capillary number at any confinement is greater than that predicted by the Maffetone and Minale extensional model. The larger slope is likely due to the secondary shear effects which are a direct result of confinement and will be discussed in greater detail later. Similar trends of increased deformation with increasing confinement were observed in confined shear flows for viscosity ratios less than $\lambda<1$ (Vananroye, Van Puyvelde et al. 2007). Unfortunately, for the microfluidic device used here, it was not possible to approach the extensional capillary number and imposed strain necessary to break the water drops in the hyperbolic contraction (Bentley and Leal 1986). We will, however, show that confinement effects can have a dramatic effect on the critical capillary number for breakup of surfactant coated drops.

For confinement greater than one, the droplets are too large to fit through the contraction without first deforming. The deformation due solely to steric confinement at vanishingly small capillary number, can be determined by starting from a simple volume conservation argument. Here two assumptions are made. First, that the flow does not deform the drop, $Ca << 1$, and second that the drop is only confined in the y-direction and not in the z-direction. The deformed drop should thus take on a pancake-like shape shown schematically in Figure 2-3. The total volume of the drop compressed between the

sidewalls of the throat of the contraction can be estimated as the sum of a cylinder with a diameter $a-2w_2$ plus a revolved semicircle with diameter $2w_2$ (this is shown schematically in Figure 2-3)

$$V=\left[\frac{\pi}{2}(a-2w_2)^2 w_2\right]+\left[\pi^2 {w_2}^2\left(\frac{a-2w_2}{2}+\frac{4}{3\pi}w_2\right)\right]. \tag{2.9}$$

By volume conservation, the deformed volume must be equal to the undeformed drop volume, $V=4/3\,\pi R^3$. Equating these, a rather messy expression for deformation parameter as a function of a confinement factor can be derived in the limit of vanishingly small capillary number, $D_C=f(C)$. Predictions from this model are superimposed over the data in Figure 2-2b resulting in a lower bound for confined drop deformation. These calculations also suggest that the deformation parameter can be renormalized to remove the deformation due to low capillary number confinement, $D - D_c$, in order to highlight the deformation resulting from the flow only. A plot of the renormalized deformation parameter is presented as an inset in Figure 2-2a. The data does not collapse onto a master curve; however, the vertical shift in the data is due to the steric effects at $C>1$ are for the most part eliminated. These results demonstrate the important role that confinement plays by not only physically limiting the lateral size of the drop, but by changing the flow type from a pure extensional flow under limited confinement to one of mixed shear and extensional flows in the presence of strong confinement. As we will see, shear flow that sets up between the droplet and the walls of the hyperbolic contraction has a strong effect not only on droplet deformation, but also on droplet breakup.

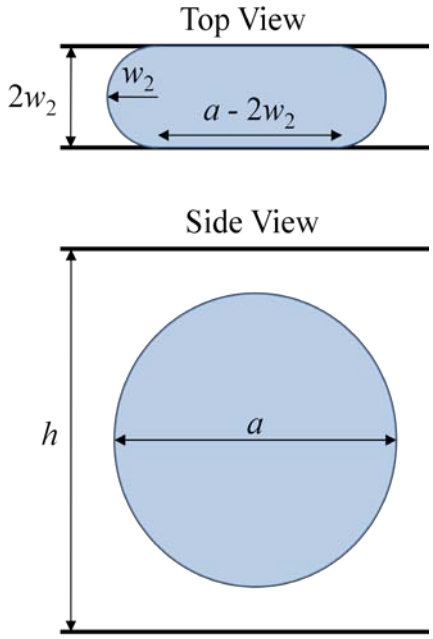

Figure 2-3: Schematic diagram illustrating shape of confined drop at $Ca = 0$.

Vananroye *et al.* (Vananroye, Van Puyvelde et al. 2006; Vananroye, Van Puyvelde et al. 2007) noted that in shear flows a confined droplet broke up at a capillary number greater than that predicted for an unconfined droplet with a viscosity ratio less than unity. However for higher viscosity ratios, $\lambda > 1$, Vananroye *et al*. (Vananroye, Van Puyvelde et al. 2007) found that confinement promoted droplet breakup. It can also be seen from their work that partially confined droplets ($C = 0.77$) deviated from the predictions of the Maffettone and Minale model, whereas nearly unconfined droplets ($C = 0.2$) undergoing shear forces agreed with the model predictions over the range of capillary numbers studied. To better understand the role of confinement on water drop deformation in extensional flows, the deformation parameter is plotted as a function of confinement in Figure 2-2b. The data shows that the droplet deformation increases with increasing confinement for a given capillary number. This observation is made more

clear by isolating a single capillary number, $Ca = 0.02$, within the many data sets presented in Figure 2-2b. The general trends in the data agree with those in the literature for confined shear flows (Bentley and Leal 1986; Vananroye, Van Puyvelde et al. 2007). Additionally, the predictions of Equation 2.9 for minimum deformation for confinements greater than $C > 1$ are superimposed over the experimental data. All the deformation parameters in Figure 2-2b were found to be larger than the predicted minimum. For a given capillary number, the difference between the deformation and the zero capillary number limit, D-D_c, remains positive everywhere, but appears to decrease with increasing confinement. This suggests that the out of plane, z-direction, deformation of the drops increases with increasing confinement and increasing influence of the shear flow.

Shown in Figure 2-4 is the evolution of droplet deformation with capillary number. The deformed water droplets are initially spherical, Figure 2-4a, before undergoing a shape transition and becoming elliptical with increasing capillary number, Figure 2-4b. At larger capillary numbers, water droplets begin to take on a bullet-like shape, with a slightly blunt trailing edge and a rounded leading edge, Figure 2-4c.

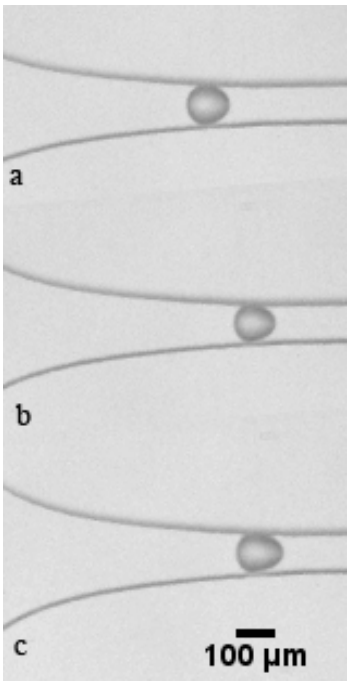

Figure 2-4: The evolution of water droplet deformation for water droplets with a confinement of *C*=0.99 and a radius r_d=49µm at various capillary numbers, (a) *Ca*=0.009 (b) *Ca*=0.013 (c) *Ca*=0.018.

2.4 Water Droplet Deformation Conclusions

Water droplet deformation and the critical capillary number for breakup was well characterized for various types of linear flows at a large number of viscosity ratios for unconfined droplets (Bentley and Leal 1986). However, droplet deformation due to extensional flows and confinement was not as well defined. Here it was found that water droplet deformation deviated greatly from the unconfined model predictions. The critical capillary number for droplet burst, $Ca_{cr} = 0.19$, was not reached, nor were droplets seen to burst below this critical capillary number. However, a droplet shape transition was seen to occur. Droplets began as spheroids and transitioned to ellipsoids as the capillary number increased. Eventually the droplets transitioned to bullet-like shapes with a blunt

trailing edge. The interplay of the extensional flow created by the hyperbolic contraction and the confinement-induced shear flow, is most likely what caused the only partially-confined droplets to deviate from the Maffetone and Minale model.

CHAPTER 3

DEFORMATION OF SURFACTANT DROPLETS IN EXTENSIONAL FLOWS

Using a microfluidic flow-focusing device a series of experiments were performed where droplets of aqueous surfactant solutions in oil were generated. The morphological development of the surfactant-laden droplets was studied for four 5mM aqueous surfactant solutions in extensional and mixed extensional and shear flows within a microfluidic hyperbolic contraction at various capillary numbers. The shear resulted from droplet confinement and was used as a first approximation of the flow field droplets experience in a concentrated emulsion. Droplet deformation was found to increase with increasing capillary number and confinement. Droplet deformation followed the predictions of theory at low capillary numbers and low confinement. For partially- to fully-confined droplets, droplet deformation was seen to vary from the predictions of theory. Droplets underwent a shape transition from spherical, to elliptical, to a bullet-like shape before tails began to form on the trailing edge of the droplet. At a critical capillary number, daughter droplets were seen to stream from the tails. The critical capillary number for tail streaming to occur varied with surfactant mobility.

3.1 Deformation of Surfactant Droplets

Surfactants are often used to stabilize emulsion droplets against coalescence because the repulsive interaction between the surfactants on the surface of the droplets prevents the droplets from coalescing (Baret, Kleinschmidt et al. 2009). Surfactants have hydrophobic tails and hydrophilic heads and will self assemble on oil-water interfaces to minimize the free energy of the system, thereby reducing the interfacial tension. On an

interface, surfactants are mobile, they can adsorb and desorb very quickly and can be moved around the droplet surface by flow, thereby setting up surface tensions gradients and inducing Marangoni flows (Leal 1992). Surfactants can be used to aid in droplet creation within microfluidic devices due to the reduction in interfacial tension between the dispersed and continuous phases. This reduction in interfacial tension also allows for a variety of droplet deformation and breakup phenomena not seen for clean water droplets (Mulligan and Rothstein 2011).

Anna et al. (Anna and Mayer 2006) explored the effects of surfactants on droplet formation within a microfluidic flow-focusing droplet generator, finding four distinct droplet formation regimes for the geometry studied: (1) geometry controlled breakup, (2) dripping, (3) jetting and (4) thread formation. Figure 3-1, shows representative images of each of the four droplet formation regimes. For a detailed discussion of the various geometries used to create droplets within microfluidic devices please see Chapter 1.2.1: Droplet Generation Using Microfluidics. Geometry controlled breakup within the flow-focusing droplet generator was achieved with the lowest capillary numbers studied and produced very monodisperse droplets on the order of the size of the flow-focusing orifice. An increase in the capillary number, achieved in this case, by increasing the total flow rate of the system, lead to the dripping droplet formation regime. In the dripping regime the finger, which produced droplets, did not retract out of the orifice as it did in the geometry-controlled breakup. Droplets formed were smaller than the size of the orifice. In the jetting regime, which required a further increase in capillary number, the finger or jet of the dispersed fluid extended past the orifice and created polydisperse droplets on the order of or larger than the size of the orifice used in droplet creation. The fourth

mode of droplet formation, thread formation, occurred at capillary numbers intermediate to geometry controlled breakup and dripping. Here large droplets break off the finger protruding from the flow focusing orifice, and then thin threads form and follow the large droplets eventually becoming unstable and breaking into much smaller droplets. This regime occurs for capillary numbers in the range $0.4 \le Ca \le 1.0$, the same region in which tip streaming occurs (Milliken, Stone et al. 1993; Anna and Mayer 2006).

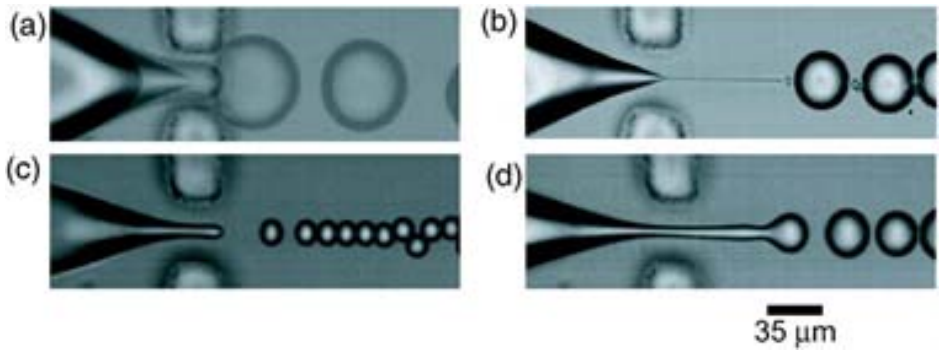

Figure 3-1: Shown here are four representative images of the four droplet formation modes. (a) Geometry controlled breakup is shown. Shown here is a series of consecutive time images over laid to show how the tip of the water phase extends and retracts during droplet formation. (b) Thread formation, (c) dripping and (d) jetting. Images courtesy of Anna *et al*. (Anna and Mayer 2006).

Deformation of clean water droplets has been well characterized in a variety of flow types (De Bruijn 1993; Stone 1994; Mulligan and Rothstein 2011). While some work has been done to understand the deformation of surfactant-laden droplets, there are a number of notable differences between surfactant-laden droplets and clean water droplets in oil. At low capillary numbers, the presence of surfactants can result in larger deformations of the interface between two immiscible fluids, such as oil and water, than would normally be seen for a drop with constant interfacial tension, such as a clean water droplet in oil. This is due to the fact that surfactants are mobile on the interface between

oil and water, and in the case of a droplet under shear or extensional flows, the surfactant can be swept to the ends of the droplet causing a local reduction in surface tension and a dilution of the overall surfactant concentration as a result of drop deformation (Stone and Leal 1990). This phenomenon is thought to be similar to the phenomenon of tip streaming, described in Chapter 1.4: Particle and Surfactant Covered Droplets. It is therefore important to understand the role of surfactants on drop deformation and breakup.

This chapter seeks to explore the deformation of surfactant-coated droplets under extensional and mixed extensional and shear flow environments. The comparison will be made to the water droplets discussed in the previous chapter. Also the effect of surfactant size and mobility on droplet deformation is investigated using an experimental setup identical to that described in Chapter 2.

3.2 Surfactant Droplet Deformation Experimental Setup

Flow cells were designed using a computer-aided design program, Auto-CAD™. Flow cells were fabricated using standard lithography techniques (Anderson, Chiu et al. 2000; McDonald and Whitesides 2002; Mulligan and Rothstein 2011). For a detailed discussion of device design and the fabrication process please refer to Chapter 2.2.1: Device Fabrication. Droplets were made using microfluidic flow-focusing techniques and deformed in a hyperbolic contraction. A hyperbolic contraction was used because it produces a nearly uniform extensional flow, allowing for the study of individual droplet deformation in extensional flows (Oliveira, Alves et al. 2007). Using the hyperbolic contraction also allowed for the study of confinement induced shear effects on individual

droplet deformation, which is a good first approximation of the flow environment in concentrated emulsions. The details of the hyperbolic contraction can be found in Chapter 2.2.2: Hyperbolic Contraction and Droplet Deformation.

The continuous phase was once again Miglyol Oil 840, however for this set of experiments the dispersed phase consisted of one of four different aqueous surfactant solutions. The surfactant solutions consisted of 5mM cetylpyridinium chloride (CPyCl) in water, 5mM hexadecytrimethyl ammonium bromide (CTAB) in water, 5mM octyltrimethyl ammonium bromide (OTAB) in water and sodium oleate (NaOa) in water. The interfacial tension between Migylol oil 840 and each of the dispersed phase solutions was characterized using a pendent drop experiment (Dataphysics, OCA 20, San Jose, CA) and are listed in Table 3-1. In all cases the viscosity ratio was fixed at λ=0.1. For the 5mM CPyCL solution both flow cell FC1 and FC2 were used to study droplet deformation. However for the other three surfactant solutions only FC2 was used to study the surfactant-laden droplet deformation. For the relevant flow cells dimensions please refer to Table 2-1. For a schematic of the flow cells used please refer to Figure 2-1.

Table 3-1: The relevant interfacial tensions and viscosities for the various droplet phase fluids used in the experiments.

Fluid	σ [mN/m]	η [mPa·s]
Water	19	1
CPyCl	4.8	1
NaOa	5.6	1
CTAB	2.1	1
OTAB	5.6	1

3.3 Surfactant Droplet Deformation Results and Discussion

These experiments studied the deformation of surfactant covered droplets in extensional and mixed shear and extensional flows. Surfactants act to stabilize droplets against coalescence in emulsions; however they also reduce the surface tension between the droplet and continuous phases of the system. Figure 3-2 shows two different surfactant solution droplets at the beginning of the hyperbolic contraction at varying capillary numbers and a water drop for comparison. Some droplets in Figure 3-2 are shown past the hyperbolic contraction in order to emphasize the tails which form on the trailing edge of the droplets. Figure 3-2(a-e) show droplets of CPyCl with an undeformed radius of r_d=38 μm and a confinement of C=0.77. As the capillary number increases from top to bottom, the drop deformation increases and the droplet shape progresses from an ellipsoid to a bullet and finally to what appears to be a rocket ship shape. The same holds true for the fully confined droplet of NaOa, $C = 1.1$, shown in Figure 3-2(f-j). In the case of the NaOa the droplet shape transitions from an ellipsoid to a bullet to tail streaming. Mietus *et al*. (Mietus, Matar et al. 2002) found similar twin tails when applying an orthogonal shear to macroscopic drops of castor oil in a Couette cell. The process that forms these tails is similar to the process of tip streaming. Tip streaming is a well-understood phenomena, which occurs due to a surface tension gradient at the tip of a jet or droplet (Eggleton, Tsai et al. 2001; Anna and Mayer 2006). The surface tension gradient is most likely the result of a surfactant concentration gradient caused by surfactants being swept by the extensional, as in Figure 3-4(c-d), and/or shears flows, as in Figure 3-4(e-f), to the tip/poles of the droplet. Booty *et al*. (Booty and Siegel 2005) performed simulations to show the evolution of tip streaming from the polls of a droplet

held in place by a four-roll mill and undergoing zero-Reynolds-number extensional flow. They also showed that in the limit of zero surface diffusion of surfactant, the insoluble surfactants immobilize the surface of a droplet. The movement of the surfactants to the back of the drop causes a large reduction in the surface tension making the formation of sharp, cusp-like interfaces energetically favorable.

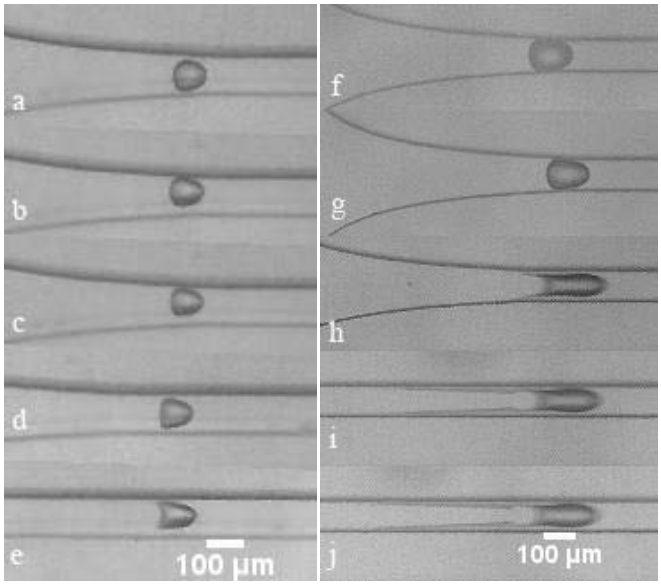

Figure 3-2: Droplet deformation for two different types of surfactant coated droplets. The capillary number increases from top to bottom in each case. (a)-(e) are 5mM cetylpyridinium chloride (CPyCl) solution droplets with a confinement of C=0.77 and a radius of r_d=38 um. (a) Ca=0.014 (b) Ca=0.024 (c) Ca=0.03 (d) Ca=0.05 (e) Ca=0.08. (f)-(j) are 5 mM Sodium Oleate (NaOa) solution drops and these drops have a confinement of C=1.1 and a radius of r_d=55 um. (f) Ca=0.002 (g) Ca=0.006 (h) Ca=0.016 (i) Ca=0.019 (j) Ca=0.21.

Droplet deformation was measured as a function of the extensional capillary number and the amount of relative confinement of the drop. Not all droplets remain elliptical in shape, therefore a schematic is shown in Figure 3-3 to demonstrate how each of the droplet shapes are measured to determine values of a and b. It is important to note

that the length of the tails formed at the rear of some drops was not incorporated into the deformation parameter because we felt that would skew the data.

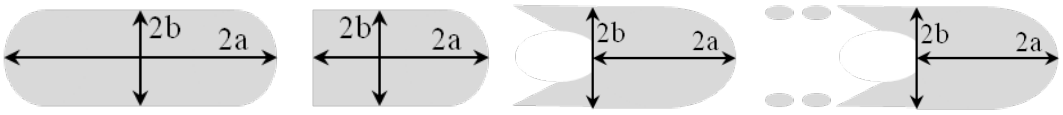

Figure 3-3: Schematic of how droplet deformation is measured for various deformed droplet shapes.

As seen in Figure 3-2, the shape transitions observed for surfactant covered droplets are quite different from those observed for water droplets in Figure 2-4 in the previous chapter. The deformed water droplets are initially spherical before becoming elliptical with increasing capillary number, Figure 2-4. At larger capillary numbers, water droplets begin to take on a bullet-like shape, with a slightly blunt trailing edge and a rounded leading edge. Surfactant-laden droplets on the other hand transition to the bullet-like shape at a much lower capillary number than water droplets do. As the capillary number is further increased, long tails of fluid are pulled first as a single tail from the center of the surfactant-laden drops and then as the drop is more heavily confined two tails form near the wall as seen in Figure 3-4. The location of the two tails near the wall suggests that they are shear induced, while the single tail in the center is extensionally induced. In fact, tails are clearly observed to occur at lower capillary numbers with increasing confinement. Once these long tails are formed, the surfactant droplets begin to shed material in the form of daughter drops from the tailing edge of the droplet. For the 5mM CPyCl solution, the bullet shape forms at a capillary number of $Ca = 0.005,$ whereas the bullet shape for the NaOa is not observed until a capillary number of $Ca = 0.006$.

Inspecting the tails shown in Figure 3-4 more closely, we see that the droplet enters the contraction as an ellipsoid with the front of the droplet always being slightly thinner than the rear of the droplet. The droplet continues to extend as it enters the contraction, with a single tail forming on the rear of the droplet indicating the presence of strong extensionally-dominated flow at moderate drop confinement. As was seen in four-roll mill extensional flow experiments (Bentley and Leal 1986), a single tail forms at the rear stagnation point of the droplet, Figure 3-4c. The single tail continues to extend until the tailing edge of the droplet becomes fully confined. At this point in the flow, shear becomes important and two tails form on the end of the droplet next to the walls of the contraction, Figure 3-4e. The single tail is simultaneously observed to detach from the middle of the droplet and breakup. As the droplet progresses further into the contraction, the double tails along the walls of the contraction also begin to breakup. This transition from the single tail to double tails highlights the complexity of drop deformation in confined extensional flows as the flow transitions from pure extensional to mixed kinematics with increased confinement. It also demonstrates that unlike in shear flows, confinement for viscosity ratios less than one, $\lambda < 1$, reduces the critical capillary number for drop breakup by as much as an order of magnitude. Note that in unconfined extensional flow critical capillary number for tip streaming is reported as $Ca = 0.5$ for $\lambda \leq 0.1$ (Stone 1994; Anna and Mayer 2006).

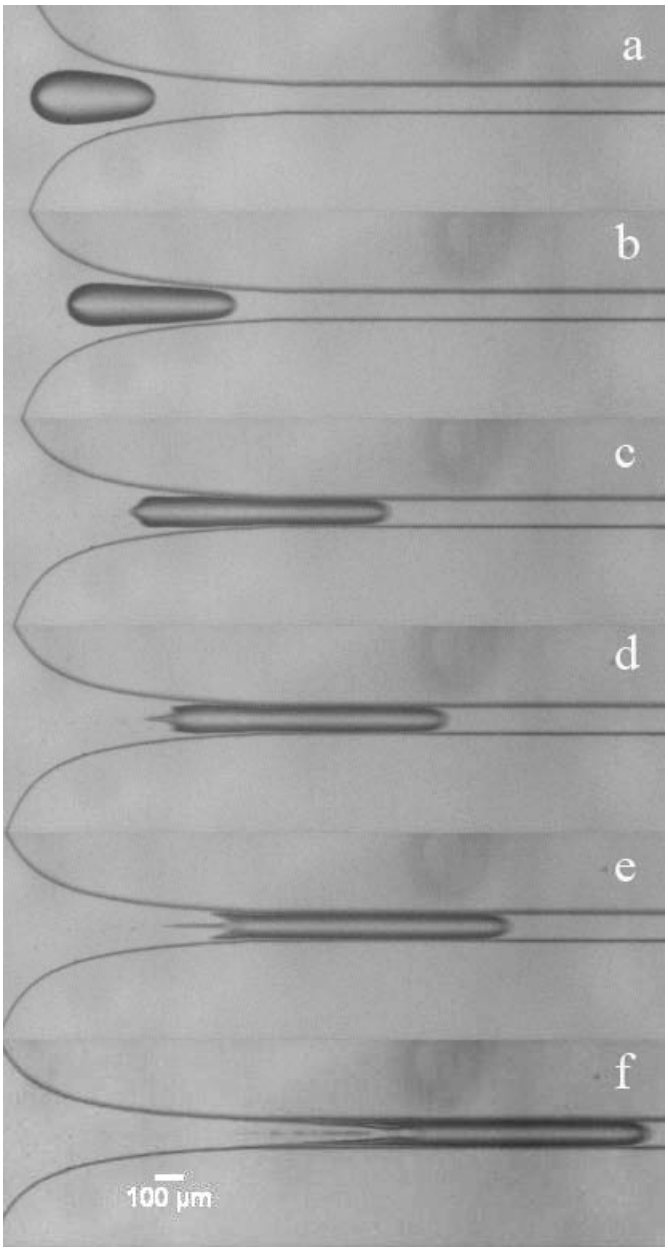

Figure 3-4: A time series of images showing tail formation due to extensional stresses placed on the droplets as they enter the hyperbolic contractions. This is a solution of 5mM NaOa in miglyol oil 840. In (a) the drop is entering the contraction at time *t*=0 ms. In (b) the drop is shown further into the contraction at time *t*=1.62 ms. In (c) the extensional tail is seen beginning for form the back of the drop at *t*=3.24 ms. In (d) the extensional tail is seen at *t*=3.82 ms. In (e) the formation of two other tails due to the confinement of the droplet is shown at *t*=4.4 ms. In (f) the drop is seen as it is out of the contraction and fully confined at *t*=5.56 ms.

In Figure 3-5, a phase diagram is presented for all surfactant solutions used, which quantifies the transition from droplets which do not have tails to droplets which do have tails which stream daughter droplets. The lines included on the graphs in Figure 3-5 are simply meant to guide the eye, they are not meant to be quantitative. It is interesting to note that the OTAB solution, like water, does not form tails at the trailing edge of the droplet at any of the capillary numbers or confinements tested. The transition to tail streaming occurs at a different capillary number for each of the surfactant solutions tested. This is likely due to the differences in molecule size and mobility of each surfactant. Smaller molecules diffuse to and along the droplet interface more quickly than the larger molecules (Ferri and Stebe 2000). Since OTAB is the smallest molecule, it is also likely the most mobile. Higher flow rates and capillary numbers are therefore required to produce the same surfactant concentration and surface tension gradients achieved along the droplets populated by the large, less mobile surfactants. Higher capillary numbers could not be reached for the OTAB solution under these experimental conditions. As a result, the OTAB appears to behave more like the water droplets than the other surfactant solution droplets. For the NaOa solution drops, tail formation happens at higher confinement and capillary numbers than for the other surfactant solutions presumably because it is the second smallest and second most mobile molecule.

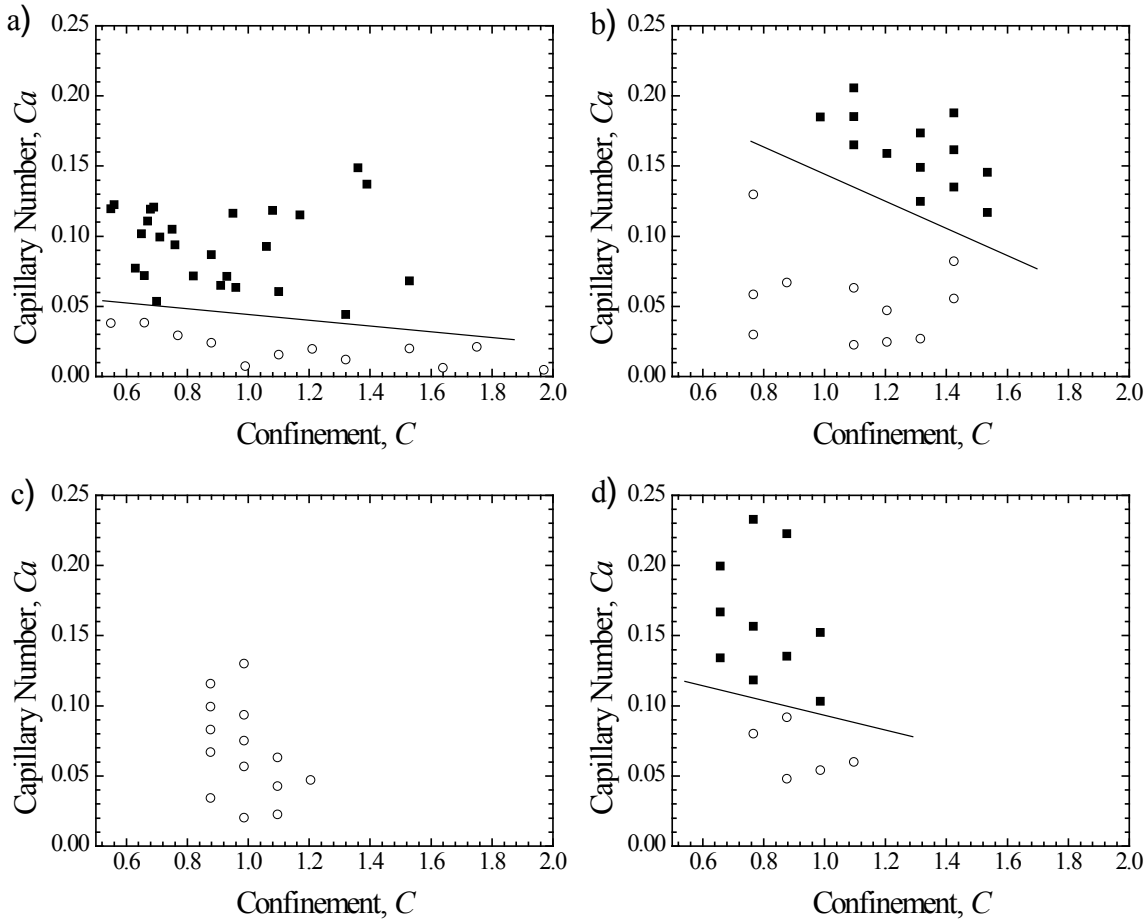

Figure 3-5: Phase diagram showing the presence of tails (■) or no tails (○) for the flow of four different surfactant solutions through a hyperbolic contraction. Data is included for a) 5mM CPyCl, b) 5mM NaOa, c) 5mM octyltrimethyl ammonium bromide (OTAB) and d) 5mM hexadecytrimethyl ammonium bromide (CTAB) A line is super-imposed over the data to emphasize the transition from no tails to tails. This line is not quantitative but is only meant to guide the eye.

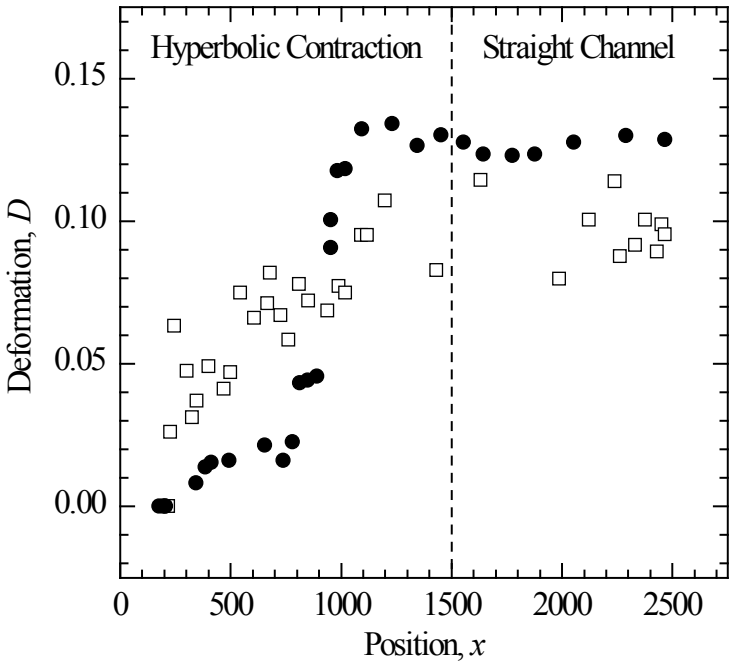

Figure 3-6: The deformation parameter, *D*, as a function of position, *x*, within the channel for CPyCl droplets. The hyperbolic contraction extends from $0 \le x \le 1500$ μm. Beyond $x = 1500$ μm the width of the microfluidic channel is fixed at $w_2 = 50$ μm. The data include a confinement and capillary numbers of $C = 0.66$ and $Ca = 0.034$ (□) and $C = 1.1$ and $Ca = 0.008$ (●).

In Figure 3-6 the evolution of droplet deformation through the hyperbolic contraction is shown for a partially and fully-confined droplet. Droplet deformation initially increases as it passes through the contraction. However, in both the partially and full-confined case the deformation asymptotes to a steady state value well before the end of the hyperbolic contraction at $x = 1500$ μm. For both droplets, the data initially shows a first order growth in the droplet deformation leading to an asymptotic steady state value achieved relatively early on in the hyperbolic contraction and well before the start of the downstream straight channel. For the fully-confined droplet, $C = 1.1$, the initial plateau

is close to the predictions of the unconfined Maffetone and Minale model, however, at a position of about x=750 μm, a shape transition is observed from an ellipsoidal to a bullet-like shape along with a corresponding jump in the droplet deformation. At the point of the shape transition, the droplet is at a relative confinement of about C=0.73. It is not until a position of about $x = 900$ μm that the droplet becomes fully-confined, $C > 1$, by the contraction walls. So it is clear that the effects of shear are felt even for partially-confined flow.

Figure 3-7a shows the deformation parameter as a function of the capillary number for CPyCl surfactant solution droplets. The trends for the deformation parameter as a function of the confinement are qualitatively similar to those observed for water in the previous chapter, with higher deformation parameters at the same capillary number. This disparity is likely due to the flow induced surface tension gradients present along the surfactant-laden drops. For low partial confinement, the deformation parameter as a function of capillary number seems to follow the Maffetone and Minale model even more closely than the clean water droplets did. However, the droplet deformation is observed to deviate dramatically from the Maffetone and Minale model above a critical capillary number. This deviation directly corresponds to the droplet's shape transitions from ellipsoids to bullet-like shapes with tails that do not shed droplets; 'rocket ships". In Figure 3-7a, a sketch of the drop shapes have been added to the data for C=0.88, to highlight where the drop shape transition from ellipsoids, to bullets, to rocket ships and finally to tail streaming occurs. The Maffetone and Minale model fails to predict the drop deformation for the shape transitions, in part, because the model assumes ellipsoidal deformation and a constant surface tension along the drop. For fully confined droplets,

the data has a very high slope leading up to a plateau where the deformation parameter seems to increase again at roughly the same slope as the slope predicted by the Maffetone and Minale model.

With the exception of OTAB droplets, which behave more like water droplets, all the surfactants behave similarly to the CPyCl. As such, rather than giving extensive data sets for each surfactant a single set of confinements was chosen to compare the surfactant droplets as a function of capillary number. In Figure 3-8, the deformation parameter is shown as a function of the capillary number for NaOa, CTAB and CPyCl at a confinement of C=0.77. The NaOa and CTAB data agree well with CPyCl. Also shown is the deformation parameter as a function of capillary number for a confinement of C=0.88 for OTAB and CPyCl. The OTAB has much smaller deformation than the CPyCl. This is most likely due to the fact that OTAB is a very small and mobile surfactant and less likely to build up the surface tension gradients needed to induce the shape transitions and tail streaming observed for the CPyCl and other surfactants. These trends are consistent across the range of capillary numbers and confinements studied.

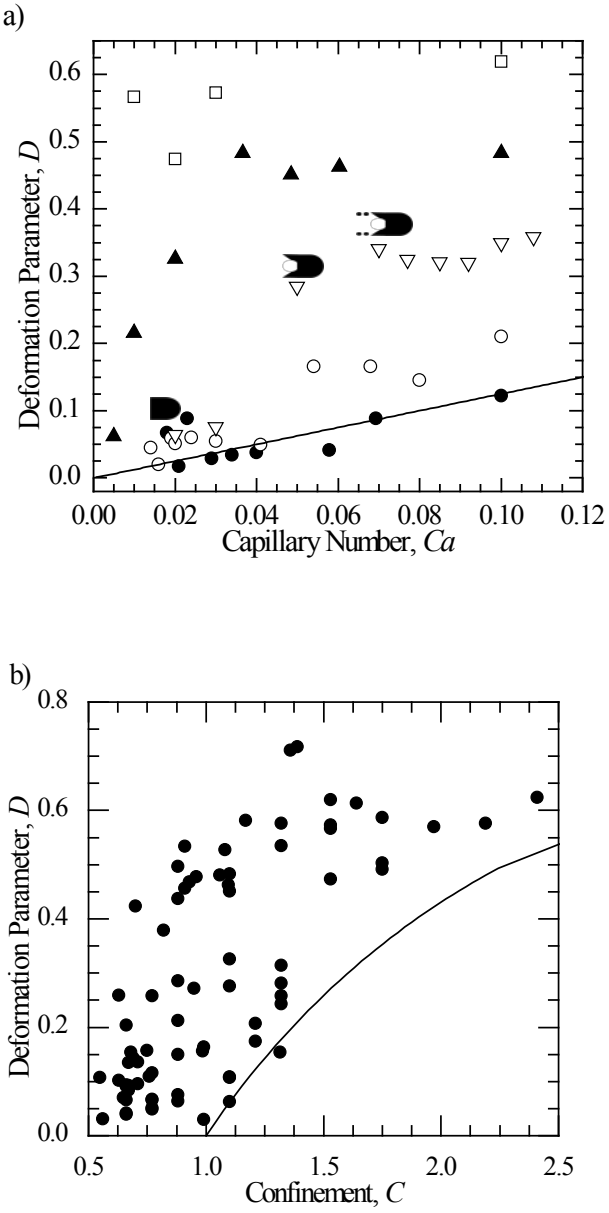

Figure 3-7: In (a) the deformation parameter is shown as a function of the capillary number at various confinements for 5 mM CPyCl drops in oil undergoing extensional flows. The strength of the extensional flow is defined by the capillary number and the deformation parameter shows the deviation of a drop from a circle. The data include confinement parameters at *C*=0.66 (●), *C*=0.77 (○), *C*=0.88 (▽), *C*=1.1 (▲) and *C*=1.5 (□). The line shown represents the results of the Maffetone and Minale model for extensional flows. In addition sketches showing drop shape transitions are superimposed over the $C = 0.88$ data. (b) shows the deformation parameter as a function of the confinement for all capillary numbers studied (●).

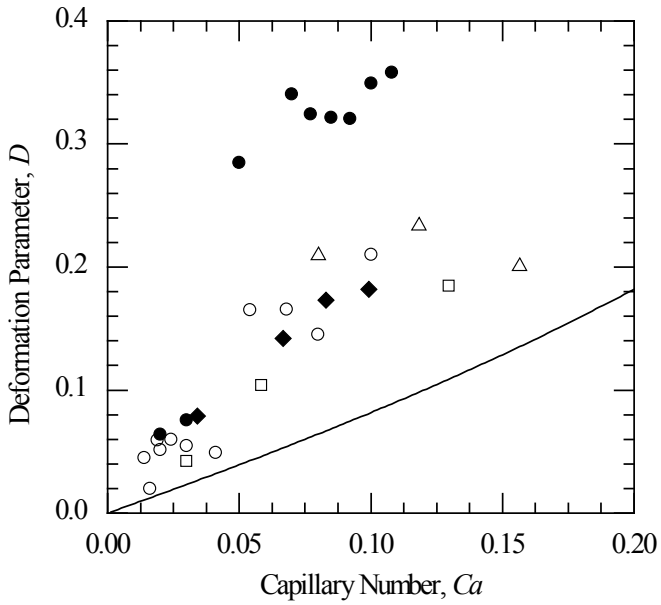

Figure 3-8: The deformation parameter is shown as a function of the capillary number at various confinements for the three other surfactant solution drops. The data include the confinement parameter of C=0.77 for NaOa (□), CTAB (△) and CPyCl (◇) and C=0.88 for OTAB (■) and CPyCl (●). The line shown represents the results of the Maffetone and Minale model for extensional flows.

As an interesting aside, a series of images are presented in Figure 3-9 demonstrating the dynamics and fluid structures that can occur when multiple deformed droplets can interact within a confined microfluidic channel. Here a small, strongly deformed droplet is observed in the wake of a larger droplet undergoing tail streaming. The smaller droplet is observed to move faster than the larger drop, eventually impacting the rear of the larger droplet and bouncing off without coalescing. In addition, the tails of the large droplet are not smooth as observed for a single droplet, but contain ripples resulting from the interplay between the tails and the multiple droplets in its wake.

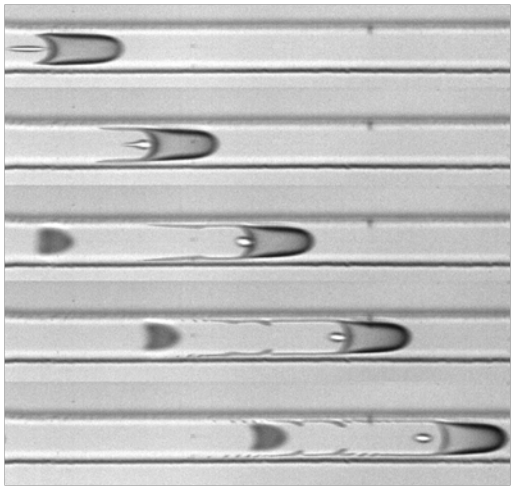

Figure 3-9: Sequence of images showing the interaction of CTAB droplets within the contraction and the interesting flow structures that result.

3.4 Surfactant Droplet Deformation Conclusions

The focus of this work was to understand the deformation of a single drop under pure extensional flow and mixed extensional and shear flow using a microfluidic hyperbolic contraction. Droplet formation and production is well characterized and understood. This knowledge was used to create droplets using a bottom up approach. Droplets moved through the microfluidic device to a hyperbolic contraction where they first experienced a homogeneous extensional flow and then some degree of shear flow as the droplets became confined. Droplet deformation was only measured after droplets had reached a steady state of deformation.

Droplets were deformed by extensional forces at the entrance to the hyperbolic contraction. The deformation of surfactant solution droplets in an oil matrix was characterized. The droplet deformation was compared to a Maffetone and Minale model for unconfined droplets, $C < 1$, undergoing pure extensional flows. Surfactant droplets followed the same trend as the Maffetone and Minale model, however the deformation

was found to grow faster than the predictions of the Maffetone and Minale model starting at a critical capillary number. This critical capillary number is found to decrease with increasing confinement and decreasing surfactant mobility. For confinements great than $C > 1.0$, the deformation data for the surfactant coated droplets never followed the Maffetone and Minale model. In some cases the deformation can be as much as three times that predicted for the unconfined droplets. Droplet deformation increased with increasing confinement and was greater than that predicted by the Maffetone and Minale model which does not include confinement in its prediction of droplet deformation.

For the range of capillary numbers and confinements test the deformed surfactant solution droplets transitioned from ellipsoids, to bullets, to bullet-like shapes with two elongated tails resembling a rocket ship and then finally to tail streaming in all cases except for the OTAB. OTAB was also not observed to follow the same trends as the other surfactant solutions when droplet deformation was plotted as a function of capillary number at a given confinement. The deformation of the OTAB solution was observed to be much smaller than that for the other surfactant solutions. The evolution of the droplet shapes, for the other three surfactants used, was seen to correspond to transitions in the deformation as a function of capillary number. In the case of CPyCl, as the droplet transitioned from a blunt bullet-like shape to a bullet-like shape with two elongated tails resembling a rocket ship, the droplet deformation began to deviate from the Maffetone and Minale model quickly. The critical capillary number for tail streaming to occur decreased with increasing confinement, as the shear forces acting on the droplet increased sweeping more surfactant to the trailing edge of the droplet facilitating the observed tail

streaming. The critical capillary number for tail streaming also decreases as surfactant mobility decreases and surfactant size increases.

CHAPTER 4

DEFORMATION OF PARTICLE COVERED DROPLETS IN EXTENSIONAL FLOW

Using a microfluidic flow-focusing device, monodisperse water droplets in oil were generated and their interface populated by either 1μm or 500nm amine modified silica particles suspended in the water phase. The deformation and breakup of these Pickering-type droplets were studied in both pure extensional flow and combined extensional and shear flow at various capillary numbers using a microfluidic hyperbolic contraction. The shear resulted from droplet confinement and increased with droplet size and position along the hyperbolic contraction. Droplet deformation was found to increase with increasing confinement and capillary number. At low confinements and low capillary numbers the droplet deformation followed the predictions of theory. For fully-confined droplets, where the interface was populated by 1μm silica particles, the droplet deformation increased precipitously and two tails were observed to form at the rear of the droplet. These tails were similar to those seen for surfactant covered droplets. At a critical capillary number, daughter droplets were observed to stream from these tails. Due to the elasticity of the particle-laden interface these drops did not return to a spherical shape, but were observed to be buckle. Although increases in droplet deformation were observed, no tail-streaming occurred for the 500nm silica particle covered droplets over the range of capillary numbers studied.

4.1 Particle Droplet Deformation

Emulsions are common in our everyday lives and can be found in food, personal care products, pharmaceuticals and can be used as microreactors (Shu, Eijkel et al. 2007). Emulsion droplets are readily deformable under flow because the liquid-liquid interface is mobile unlike solid particles (McClements 1999; Fischer and Erni 2007). Also, unlike solid particles, emulsion droplets can coalesce. For that reason, the droplets within emulsions are commonly stabilized against coalescence with the addition of surfactants or solid particles (Binks 2002). Solid particles, unlike surfactants, do not assemble into aggregates in the bulk, but they can assemble at the liquid-liquid interface where, due to their size, they are held more strongly than surfactants (Binks 2002). Particle stabilized emulsions, commonly called Pickering emulsions, have attracted a great deal of attention for their potential use in creating new materials, medications where they can act as agents to deliver drugs and cosmetics (Clegg, Herzig et al. 2007; Wang, He et al. 2010). The understanding of emulsion droplet deformation under flow has been of interest since Taylor's seminal experiments on droplet deformation (Taylor 1934). A number of studies investigated droplet deformation and breakup in both shear and extensional flows using shear rheometers, four roll mills and microfluidic devices (Mietus, Matar et al. 2002; Mulligan and Rothstein 2011). In many of these experiments the role of confinement on the deformation of a single droplet was investigated as a first approximation of the flow environment that a droplet would experience in a concentrated emulsion (Vananroye, Van Puyvelde et al. 2007; Mulligan and Rothstein 2011). In this work we will utilize a microfluidic hyperbolic contraction that can impose a nearly uniaxial extensional flow over a wide range of extension rates and degrees of droplet confinement. Although many of these studies have investigated the deformation and

breakup of droplets stabilized by surfactants, the study of the deformation of the droplets of Pickering emulsions under flow has not yet been performed. Understanding the dynamics of particle laden droplet deformation and breakup is important to a large number of industries and commercial applications as mentioned above. Rheology of bulk Pickering emulsions has shown that particle stabilized emulsions are shear-thinning (Braisch, Kohler et al. 2009) and that oil-oil droplets stabilized by particles are prevented from coalescing under shear. However, at a high enough particle concentration threads covered in particles begin to form (Tong, Huang et al. 2010).

Pickering (Pickering 1907) demonstrated how solid particles stabilize emulsions by residing at the interface of an oil droplet in a continuous water phase. A particle's ability to stabilize an emulsion depends on the particles wettabilty, shape, concentration and inter-particle interactions. For spherical particles, the energy needed to remove a particle from the interface between the two liquid phases is

$$E = \pi r_p^2 \sigma (1 \pm \cos\theta)^2, \tag{4.1}$$

where r_p is the radius of the particle. In Equation 4.1, the positive sign corresponds to the removal of the particle into the continuous phase and the minus is for the removal of the particle into the dispersed phase (Binks and Lumsdon 1999). It is interesting to note that particle stabilization was exploited by the food industry, even before the dynamics of particle stabilization were well understood, by using ice crystals in ice cream and fat particles in whipping cream (Binks 2002). A variety of different materials can be used to make particles for emulsion stabilization including fumed silica, latex, polystyrene, calcite and cadmium-selenium nanoparticles (Hsu, Nikolaides et al. 2005; Lin, Boker et al. 2005; Reynaert, Moldenaers et al. 2006; Drelich, Gomez et al. 2010; Wang, He et al.

2010). In addition bio-particles such as ferritin, which is a spherical protein have been shown to be quite effective at stabilizing these emulsions (Fujii, Aichi et al. 2009).

Recently a method was developed to measure the adsorption energy of self-assembled nanoparticles at the oil-water interface by monitoring the interfacial tension of the system during particle self-assembly (Du, Glogowski et al. 2010). It was also found that the binding energy of these systems could be tuned with the addition of salt and/or choice of solvent (Du, Glogowski et al. 2010). In some instances, salt can also be used to control the aggregation of colloidal particles on planar interfaces by screening surface charges of the particles and the interface (Reynaert, Moldenaers et al. 2006). The self-assembly of colloidal particles at the interface between two immiscible fluids is driven by the reduction of interfacial energy between the two phases (Pieranski 1980; Binks 2002; Lin, Skaff et al. 2003). Recently, however, several groups have reported not observing a reduction in the interfacial tension when particles are present on the interface between the two phases (Vignati, Piazza et al. 2003; Drelich, Gomez et al. 2010), so this seems to be an open question in the literature.

Many emulsions are prepared using high speed-mixing and agitation, which produces a polydisperse emulsion. As an example, Wang *et al*. (Wang, He et al. 2010), created Pickering-type emulsions by shaking an oil-water mixture and stabilizing the droplets against coalescence with calcite particles. More recently, microfluidic droplet creation methods have been developed to create monodisperse emulsions (Anna, Bontoux et al. 2003; Christopher and Anna 2007; Abate, Romanowsky et al. 2009; Abate and Weitz 2009; Miller, Rotea et al. 2010). In the experiments described here, a microfluidic flow focusing device of the design presented in Mulligan *et al.*, (Mulligan

and Rothstein 2011) will be used to generate monodisperse droplets for a series of Pickering emulsion studies.

Once the droplets have been created, it takes a finite amount of time for the interface to become fully populated with particles. This timescale is governed by the diffusion of particles through a fluid as they are subjected to Brownian motion. The diffusion coefficient for a spherical particle, $D_{diffusion}$, is

$$D_{Diffusion} = \frac{k_B T}{6\pi\mu r_p}, \tag{4.2}$$

where k_B is the Boltzmann constant, T is the temperature and μ is the viscosity of the fluid in which the particles are suspended (Leal 1992). From this a conservative estimate of the time for the particles to diffuse to the interface can be approximated by

$$t \approx \frac{x^2}{D_{diffusion}}. \tag{4.3}$$

where x is the distance the particle must diffuse to the surface. In our system this timescale is several seconds.

In the case where the liquid-liquid interface becomes saturated with particles, the interface can become solid because the particles become jammed and immobile. Emulsion droplets with solid elastic shells and colloidosomes have been utilized in a wide variety of encapsulation applications (Dinsmore, Hsu et al. 2002; Sander and Studart 2011). Colloidosomes are formed by emulsifying a suspension of two immiscible fluids along with colloidal particles and then replacing the continuous phase with the same solvent that is inside the colloidosome. Once the droplet interface is completely covered the resulting elastic shell has a well-defined permeability and easily measured mechanical properties (Dinsmore, Hsu et al. 2002). Dinsmore *et al.* (Dinsmore, Hsu et al.

2002), showed that the material properties can be tuned by varying the size and/or type of particle used. Sander *et al*. (Sander and Studart 2011) showed that microfluidic devices could be used to create monodisperse colloidosomes with a wide variety of surface properties which can be tuned by the choice of functionalized nanoparticles populating the surface of the colloidosomes.

Droplet formation, as well as droplet deformation and breakup, is governed by the interplay between the viscous and interfacial forces between the continuous and dispersed phase fluids. This interplay is characterized by the capillary number

$$Ca = \frac{U\eta_c}{\sigma_{12}} = \frac{\dot{\varepsilon} R \eta_c}{\sigma_{12}}, \tag{4.4}$$

where U is the velocity, R is the maximum radius of the drops that do not break, η_c is the viscosity of the continuous phase, $\dot{\varepsilon}$ is the extension rate and σ_{12} is the interfacial tension between the dispersed and continuous phases as measured with particles. Droplet deformation is defined as

$$D = \frac{a-b}{a+b}, \tag{4.5}$$

where a is the semi-major axis of an ellipse and b is the semi-minor axis of the ellipse. If a critical capillary number is reached the droplet will breakup. The critical capillary number for droplet breakup under shear and extensional flows was well characterized by Bentley and Leal (Bentley and Leal 1986), who noted that the critical capillary number for droplet breakup is a function of the type of flow, shear or extension, used to deform the droplets and also the viscosity ratio, $\lambda = \eta_d / \eta_c$, where η_d is the viscosity of the dispersed phase. In extensional flows the critical capillary number for droplet breakup is smaller than that for shear flow (Bentley and Leal 1986). The deformation of clean

droplets as well as droplets with surfactants have been well studied under various flow conditions, including irrotational flows (Bentley and Leal 1986), shear flows (Taylor 1934; De Bruijn 1993), extensional flows (Bentley and Leal 1986) and combined shear and extensional flows (Mietus, Matar et al. 2002; Mulligan and Rothstein 2011).

As seen in Mulligan and Rothstein (Mulligan and Rothstein 2011) microfluidics lends itself well to the study of individual droplet deformation and breakup. Microfluidic devices can be designed to make monodisperse, bidisperse and even polydisperse emulsions using a variety of droplet formation techniques (Christopher and Anna 2007). These droplets can then be subjected to a variety of flow types downstream of droplet formation. The deformation and breakup of individual Pickering emulsion droplets in extensional flows has never before been studied. In this work, microfluidic techniques were used to look at individual particle coated droplet deformation under extensional and then mixed extensional and shear flows utilizing a hyperbolic contraction.

4.2 Particle Coated Droplet Experimental

The experimental flow cell is shown in Figure 4-1. The flow cell varies from that used in the experiments described in Chapters 2 and 3 with the winding path to the hyperbolic contraction. Particles need time to diffuse to the droplet interface necessitating a longer time between droplet formation in the flow-focusing device and droplet deformation in the hyperbolic contraction. Particles, which were suspended in the dispersed aqueous phase were given sufficient time to populate the interface of the droplets. Devices were fabricated using standard soft lithography techniques (Anderson, Chiu et al. 2000; McDonald, Duffy et al. 2000), the process described in detail in our

previous work (Mulligan and Rothstein 2011) and the process described in Chapter 2.2.1: Device Fabrication and Chapter 2.2.2: Hyperbolic Contraction and Droplet Deformation.

Flow of the continuous and dispersed phases was driven by two stepper-motor actuated micro-syringe pumps (New Era Pump System, NE-500 OEM) using a 1 mL plastic syringe (BD, plastic Leur-Lok Tip) for the dispersed phased and a 10 mL plastic syringe (BD, plastic Leur-Lok Tip) for the continuous phase. All experiments were carried out on an inverted microscope (Nikon TE2000-U) and video data was recorded using a high-speed video camera (Vision Research, Phantom 4.6). The continuous phase fluid for all experiments was Miglyol 840 (Miglyol 840, Sasol) which has a viscosity of η_c=10 mPa·s. Miglyol 840 is used because it does not swell the PDMS flow cells over the duration of an experiment. The dispersed phase consisted of either a 3.4% suspension of 1μm diameter amine modified silica microspheres (Polysciences, Inc., Cat# 24757, Lot# 619432) or a 3.0% suspension of 500nm diameter amine modified silica microspheres (Polysciences, Inc., Cat# 24756, Lot# 608737). The viscosity ratio, $\lambda = \eta_d / \eta_c$, was fixed at $\lambda = 0.1$. The interfacial tension between Miglyol oil 840 and the 3.4% suspension of 1 μm particles was measured to be 7.1 mN/m and for the 3.0% suspension of 500 nm particles it was 15.3 mN/m. All interfacial tension measurements were made using a pendent drop experiment (Dataphysics, OCA 20, San Jose, CA).

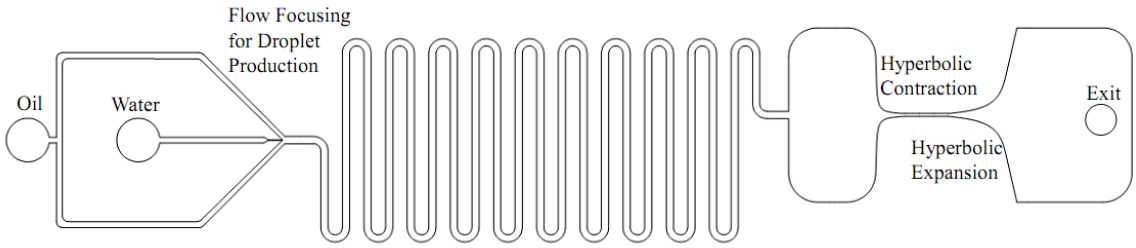

Figure 4-1: Schematic diagram of the microfluidic flow cell used in this work including the flow focusing device, the numerous turns used to give the particles time to populate the droplet interface and the hyperbolic contraction.

A hyperbolic contraction was chosen to study droplet deformation under extensional flow and to investigate the role of confinement on droplet deformation because it can be used to achieve a nearly constant extensional flow along the center-line of the contraction (Oliveira, Alves et al. 2007). Extensive details of the hyperbolic contraction geometry can be found in previous work (Randall, Schultz et al. 2006; Mulligan and Rothstein 2011) and in Chapter 2.2.2: Hyperbolic Contraction and Droplet Deformation. After reaching its minimum width, the contraction is extended for an additional distance at a separation of $2w_2$, where w_2 is the final downstream half-width of the contraction, so that the effect of confinement on droplet deformation can be observed.

Shown in Table 4-1 are the relevant dimensions of the two flow cells used. The contraction is then re-expanded through a hyperbolic expansion designed to result in a compression rate ten times smaller than that of the contraction.

Table 4-1: Dimensions for each of the flow cells used in the experiments.

	w_1 (μm)	w_2 (μm)	l_c (μm)	Extension (μm)	c_1 (mm^2)
FC3	3000	50	1000	1500	0.025
FC4	6000	75	1500	2000	0.056

In the set of microfluidic devices used in these experiments, a range of extension rates between $90s^{-1} < \dot{\varepsilon} < 2300s^{-1}$ were accessible. Additionally, the total Hencky strain imposed on the fluid can be determined from $\varepsilon = \ln(w_1 / w_2)$ which for our geometry is equal to ε_{FC3}= 4.1 and ε_{FC4}= 4.4. The extension rate calculated from Equation 4.7 was used to recalculate an extensional capillary number from Equation 4.4.

4.3 Particle-Laden Droplet Deformation Results and Discussion

The deformation of Pickering emulsion droplets with 1 μm diameter particles populating the oil-water interface is shown in Figure 4-2 as a function of capillary number for a broad range of droplet confinements. SEM images of the particles were taken to verify that the particles were discrete particles and not chains of particles, which would affect the packing dynamics of the particles as well as the elasticity and rigidity of the particle shelled formed on the droplets. Scanning Electron Microscope (SEM) images for both 1μm and 500nm amine modified silica particles can be seen in Figure 4-3. Each point in Figure 4-2, is averaged over multiple drops with the same confinement and capillary number. All droplets are measured at the end of the hyperbolic channel just after it passes into the straight channel, as described in the previous two chapters.

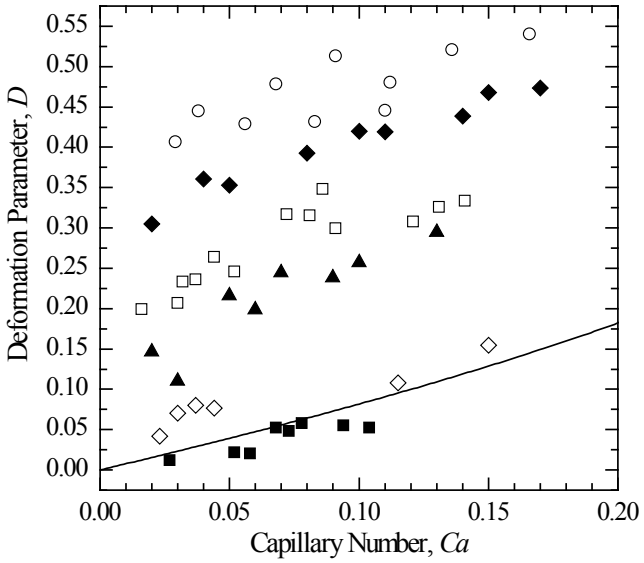

Figure 4-2: Deformation parameter as a function of the extensional capillary number is shown at various confinements for 1 μm amine modified silica particle coated droplets in oil. The data includes confinements of *C*=0.6 (■), *C*=0.9 (◇), *C*=1.1 (▲), *C*=1.2 (□), *C*=1.4 (◆), *C*=1.6 (○). The line is a prediction of droplet deformation when droplets are not confined.

For unconfined clean water droplets, in a continuous oil phase, with a viscosity ratio of $\lambda = 0.1$ the critical capillary number for droplet breakup is predicted to be $Ca_{cr} = 0.19$ (Bentley and Leal 1986). Mulligan and Rothstein (Mulligan and Rothstein 2011) recently showed that confinement and the resulting shear from the walls of the hyperbolic contraction can significantly increase the deformation of water and surfactant covered droplets at the same capillary number. Similar results are observed here for the particle covered droplets. In Figure 4-2, the droplet deformation increases monotonically for any given confinement from left to right between capillary numbers of $0.02 \le Ca \le 0.18$. For the moderately confined case of $C = 0.6$ the line for the droplet deformation as a function of capillary number lies close to the line of droplet deformation

without confinement predicted by the Maffetone and Minale model (Maffettone and Minale 1998), while the case of $C = 0.9$ shows a modest increase over the Maffetone and Minale model. These trends were also observed for unconfined water and surfactant droplets (Mulligan and Rothstein 2011). Surfactant coated droplets were seen to deviate from the predictions of the Maffetone and Minale model at a confinement of $C = 0.8$ due to the droplets transitioning from the predicted ellipsoidal deformation to bullet-like shapes and eventually to tail streaming (Mulligan and Rothstein 2011). Tail streaming will be discussed in more detail later in this chapter and has been discussed in previous chapters in detail. The Maffetone and Minale model was used to predict droplet deformation in the absence of confinement for homogenous uniaxial extensional flow. The model assumes the droplets remain ellipsoidal and do not breakup, therefore it is only truly valid at moderate to low capillary numbers. A detailed discussion of the Maffetone and Minale model and how it relates to droplet deformation can be found in (Maffettone and Minale 1998; Mulligan and Rothstein 2011). For fully-confined droplets, $C \geq 1$, the droplet deformation is found to deviate quickly from the predictions of the Maffetone and Minale model. Droplet deformation increases monotonically with capillary number even in the presence of confinement, however, as droplet confinement increases, larger droplet deformations are seen for a given capillary number. These trends are similar to those noted for water and surfactant droplet deformation within a hyperbolic contraction, although for surfactant covered droplets, deviation from the Maffetone and Minale model is observed even for confinements of $C < 1.0$ (Mulligan and Rothstein 2011).

As seen in Figure 4-4, the droplet deformation increases with increasing confinement beyond $C > 1.0$ for all capillary numbers tested. In Figure 4-4, the data from Figure 4-2 is replotted to investigate the relationship between deformation and confinement. The solid line in Figure 4-4 shows the predictions for droplet deformation at zero capillary number due to confinement effects alone (Mulligan and Rothstein 2011). For droplets which are fully-confined, $C \geq 1$, the initial droplet radius is larger than the final half width, w_2, of the downstream contraction and the droplets are too large to fit through the contraction without deforming. Therefore even in the absence of flow, these droplets would be deformed solely due to confinement. All points in Figure 4-4 lie above the line for droplet deformation without flow. However, it is important to note that the deformation observed in Figure 4-2 is not solely due to the presence of the contraction walls, nor is it a superposition of the steric deformation and the deformation due to a purely extensional flow as predicted by the Maffetone and Minale model and observed for unconfined droplets. The droplet deformation is due to a complex interplay between the extensional and shear flow in the hyperbolic contraction and we will see that, for the fully-confined case, the result is a shape transition in the particle laden droplets. Shape transitions were also observed for the surfactant coated droplets deformed by extensional flows and mixed extensional and shear flow conditions within a hyperbolic contraction (Mulligan and Rothstein 2011).

a)

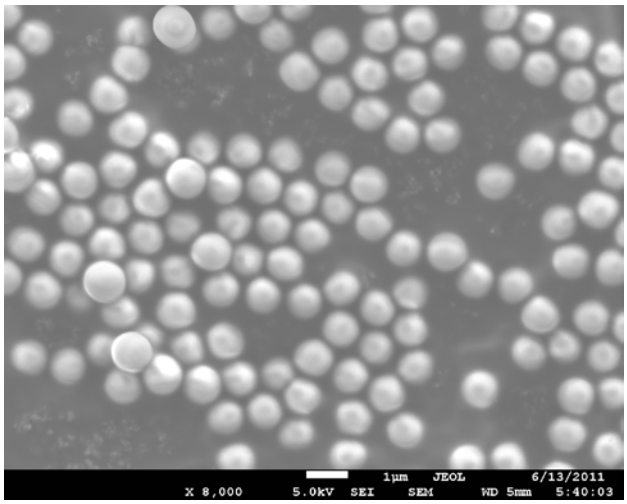

b)

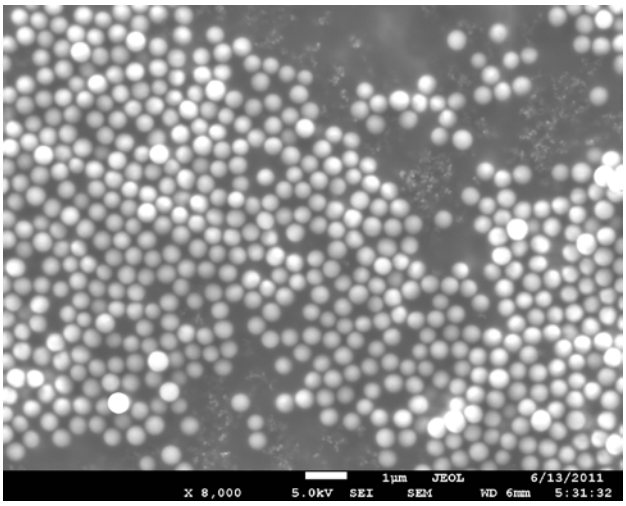

Figure 4-3: a) Scanning Electron Microscope (SEM) image of 1 µm amine modified silica particles. b) SEM image of 500 nm amine modified silica particles

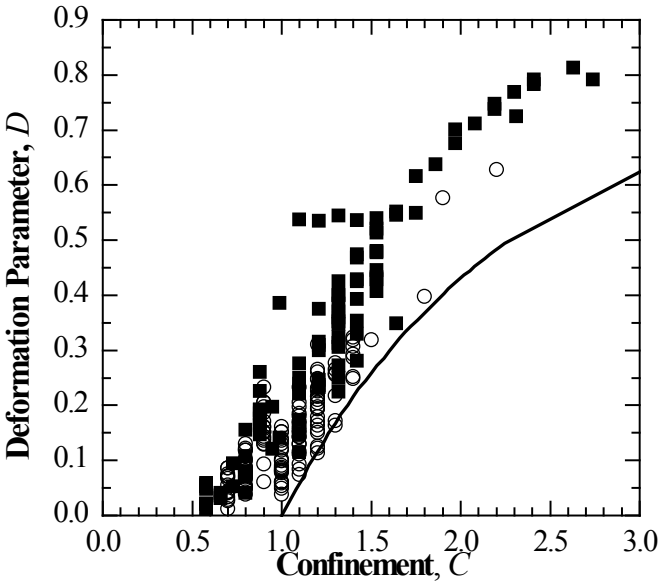

Figure 4-4: Droplet deformation as a function of confinement for droplets covered with 1 μm silica particles (■) and 500 nm silica particles (○) for all capillary numbers studied. The solid line shows the deformation parameter as a function of confinement at zero capillary number.

Particle image velocimetry measurements have shown that for the hyperbolic contraction, the velocity profile is relatively flat across the channel. As a result, across roughly the inner 80% of the channel width, the velocity is nearly constant and can be approximated as plug flow. However, the presence of shear near the walls can play an important role in droplet deformation especially for fully-confined or the nearly fully-confined droplets (Oliveira, Alves et al. 2007; Mulligan and Rothstein 2011). The shear rate is at a maximum near the walls and vanishes at the center line of the contraction. At the narrowest points in the contraction the shear rate can be twice as much as the extension rate, however shear rate decreases significantly at wider points of the

contraction. The significance of shear increases as droplet confinement increases due to the proximity of the droplet edge to the walls of the contraction.

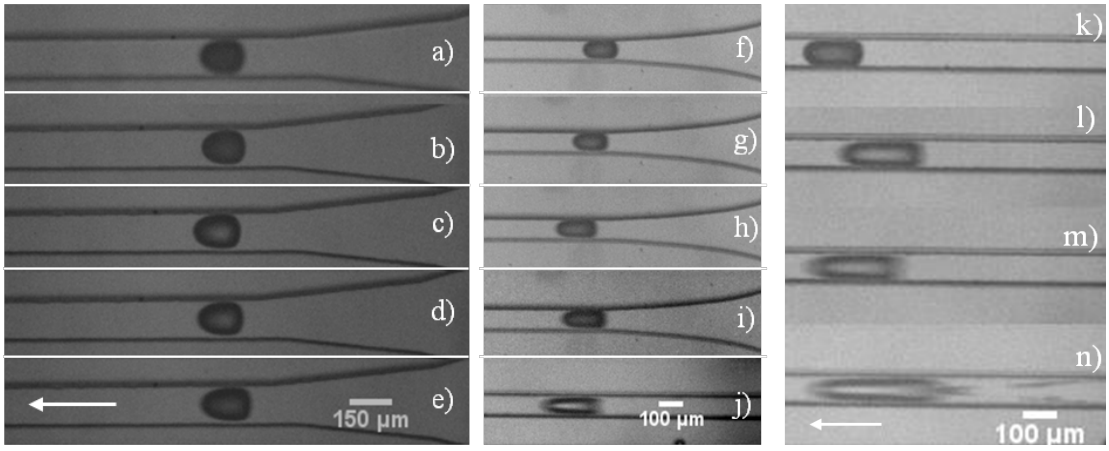

Figure 4-5: Droplet deformation for a partially-confined droplet, $C = 0.9$, and a fully-confined droplet, $C = 1.1$, coated with 1 µm amine modified silica particles. Capillary number increases for each series of images from top to bottom. (a)-(e) shows a droplet with *C* = 0.9 and r_d = 66 µm. (a) *Ca* = 0.06, (b) *Ca* = 0.07, (c) *Ca* = 0.09, (d) *Ca* = 0.1, and (e) *Ca* = 0.2. (f)-(j) shows a droplet with *C* = 1.1 and r_d = 55µm. (f) *Ca* = 0.02, (g) *Ca*= 0.05, (h) *Ca* = 0.07, (i) *Ca* = 0.1, and (j) *Ca* = 0.2. (k)-(n) shows droplet deformation for a fully-confined droplet, $C = 1.3$ and $r_d = 66$ µm, at various capillary numbers. (k) $Ca = 0.04$, (l) $Ca = 0.09$, (m) $Ca = 0.1$ and (n) $Ca = 0.2$.

Shown in Figure 4-5 are a series of images of a partially-confined droplet, $C = 0.9$, and two fully-confined droplets, $C = 1.1$ and $C = 1.3$, traveling through the hyperbolic contraction at various capillary numbers. For the partially-confined droplet, Figure 4-5(a)-(e), a gradual shape transition from an ellipsoidal shape to a flat trailing droplet edge, bullet-like shape, is observed as the capillary number increases from $0.06 \le Ca \le 0.2$. For the fully-confined droplet, over the same range of capillary numbers, the shape transition is sharper and the deviations from the ellipsoidal shaped droplets are more dramatic. In Figure 4-5(f)-(j), the initial shape transition from an

ellipsoidal droplet, to a bullet-like droplet which has a blunt trailing edge can be seen in Figure 4-5(h). At larger capillary numbers a second transition occurs to a rocket-ship like shape as seen in Figure 4-5(j). Shown in Figure 4-5(k-n) is a highly-confined droplet, $C = 1.3,$ and droplet radius, $r_d = 66\,\mu\text{m}.$ This sequence of images illustrates the drop shape transition from an ellipsoid to tails of daughter droplets streaming from the trailing edge of the parent droplet. As the capillary number increases, the droplet progresses from an ellipsoidal shape, as seen in Figure 4-5(k), to a bullet like shape, Figure 4-5(l), to a droplet with two tails, Figure 4-5(m) and finally to a droplet that breaks up producing a series of daughter droplets, Figure 4-5(n). It appears that the droplets trailing in (n) originate from the breakup of two tails on either side of the droplets trailing edge at the walls. The two tails break off the parent droplet and form daughter droplets, which trail behind the parent droplet and draw additional droplets from the center of the trailing edge of the parent droplet. This illustrates the interplay between the extensional and shear flow in the channel that was seen in (Mulligan and Rothstein 2011). Interestingly, a very similar transition was seen for droplets covered with surfactants (Mulligan and Rothstein 2011) and was likened to the phenomena of tip streaming (Anna and Mayer 2006). However, unlike surfactant covered droplets, in the case of these particle-laden droplets, the formation of tails on the rear of the droplet was only observed for the fully-confined cases. It is possible that tails could be observed in the case of the partially-confined droplet for much larger capillary numbers. However our experiments were limited to a maximum capillary number of approximately $Ca = 0.25.$ It is however likely that particles on the interface of the droplet have formed an elastic shell which resists significant droplet deformation and large-scale shape transitions in the absence of

confinement. The presence of this elastic shell has additional implications and results in some interesting physical phenomena which will be discussed in greater detail later. Figure 4-6 is a phase diagram meant to illustrate under what capillary number and confinement conditions tails form on the rear of the 1 μm particle-laden droplets.

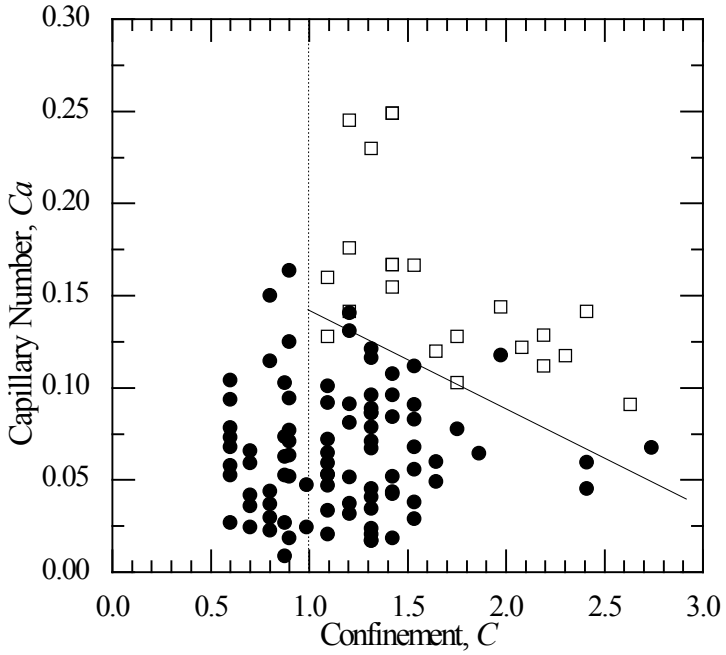

Figure 4-6: Capillary number as a function of confinement showing when tails (□) form on the rear of the 1 μm particle coated droplets and when they do not form (●). The vertical dotted line shows where droplets become fully-confined. The solid line superimposed over the data is not quantitative, but meant to emphasize the transition from no tails to tails.

A time progression of a large drop entering the hyperbolic contraction is shown in Figure 4-7 to illustrate the dynamics of tail formation and breakup for particle-laden droplets. Unlike surfactant covered droplets, which were found to produce sharp tails, the droplets in this case form rounded tails that resemble those on a fish. Once formed

near the walls, the tails are pulling off from the center of the tailing edge of the droplet, where the extensional forces dominate the flow. The difference in the observed shape of the tails formed on the surfactant covered and particle-laden drops is most likely due in part to the difference in the size of the particles (1 μm) and surfactants (several nanometers) used in previous studies (Mulligan and Rothstein 2011). The relative particle size is not negligible when compared to the size of the droplets which are typically on the order of 50 μm in radius. A close analysis of the tails formed in Figure 4-5(k-n) and Figure 4-7 indicates that the radius of curvature of the tail and the ejected daughter drops is of the same order as the silica particles. Additionally, the size and shape of the particles limits the number and packing of particles at the rear stagnation point and thus the effectiveness to which they can locally reduce surface tension and increase droplet curvature. Finally, note that the breakup of particle-laden drops occurs at significantly lower capillary number than that of the confined or unconfined water droplets. However, when compared to surfactant droplets, the breakup occurs at a slightly higher capillary number for a given confinement and the resulting daughter droplets are significantly larger.

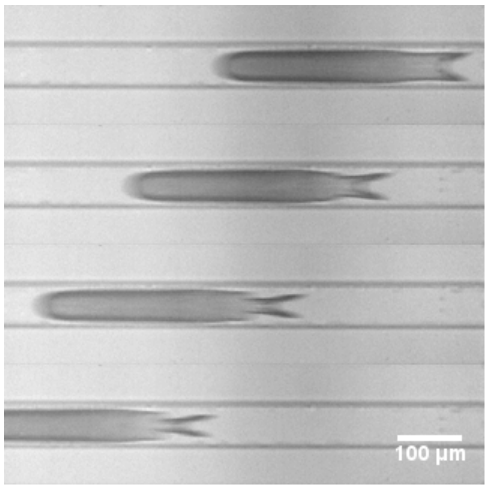

Figure 4-7: Sequence of images showing tail formation on the trailing edge of a fully-confined droplet.

To illustrate the effect that confinement has on droplet deformation, the deformation of two partially-confined, $C = 0.6$ and $C = 0.9$, at capillary numbers of $Ca = 0.03$ and $Ca = 0.07$ respectively and a fully-confined droplet, $C = 1.1$, at a capillary number of $Ca = 0.06$ are shown in Figure 4-8 as a function of the droplet's position along the contraction. The droplets position was measured based on the relative position of the leading edge of the droplet with the start of the contraction at $x / l_c = 0$. For these experiments, two different sized hyperbolic contractions were used, FC3 and FC4 and the position of the droplets along the channel was normalized by the contraction length, l_c, for both channels. For the partially-confined droplets, flow cell FC4 was used and for the fully confined droplet, flow cell FC3 was used. A value of $x / l_c = 1$ corresponds to the transition from the contraction to the straight extension. For the partially confined droplet with $C = 0.6$, the maximum deformation of $D \cong 0.02$ at $x / l_c = 0.6$. For the partially-confined droplet with $C = 0.9$ the droplet reaches maximum deformation at a position of $x / l_c = 1.1$, which is just past the end of the hyperbolic contraction. For the

fully-confined droplet, the droplet becomes fully-confined before reaching the narrowest part of the contraction; at a position of $x/l_c = 0.8$, as shown by the dashed lined in Figure 4-8. This droplet reaches maximum deformation at $x/l_c = 1.25$, 250 μm after the end of the contraction. For the fully-confined case, the droplet deformation increases continuously with position. Thus, in this case, it is clearly the confinement that dictates the evolution of the drop size and shape and less the strength of the extensional flow. For the partially-confined droplets, the deformation does not grow continuously. Instead, the droplet with $C = 0.9$ quickly reaches an asymptotic value of $D \cong 0.02$ before increasing sharply at $x/l_c = 0.8$. This asymptotic value is consistent with the predictions of the Maffetone and Minale model for an unconfined droplet as seen in Figure 4-2 and the jump in deformation occurs at a point where the droplet confinement is $C = 0.7$ and a transition in shape from ellipsoidal to bullet-like.

To investigate the effect of particle size on droplet deformation and breakup, 500 nm particles were also used to populate the droplet interfaces. Similarly to the 1 μm particle coated droplets, the 500 nm particles showed an increase in droplet deformation as a function of capillary number for any given confinement, as shown in Figure 4-9. Droplet deformation was found to deviate from the predictions of the Maffetone and Minale model for droplets with 500nm particles adsorbed to the interface. This likely is due to the fact that droplets studied all had a confinement of $C \geq 0.8$ or more. As Figure 4-8, and our previous studies have shown, confinements above about $C > 0.7$ all show enhanced deformation (Mulligan and Rothstein 2011). When compared to the deformation of droplets coated with 1μm particles, the deformation induced on droplets with the smaller 500nm particles is slightly reduced. For example, the 1 μm particle

covered droplets with a confinement of $C = 1.4$, droplet deformation ranged from $0.3 \le D \le 0.45$ over a range of capillary numbers $0.02 \le Ca \le 0.16$. While, for the 500 nm particle covered droplets with a confinement of $C = 1.4$ droplet deformation ranged from $0.25 \le D \le 0.33$ for the range of capillary numbers from $0.009 \le Ca \le 0.06$.

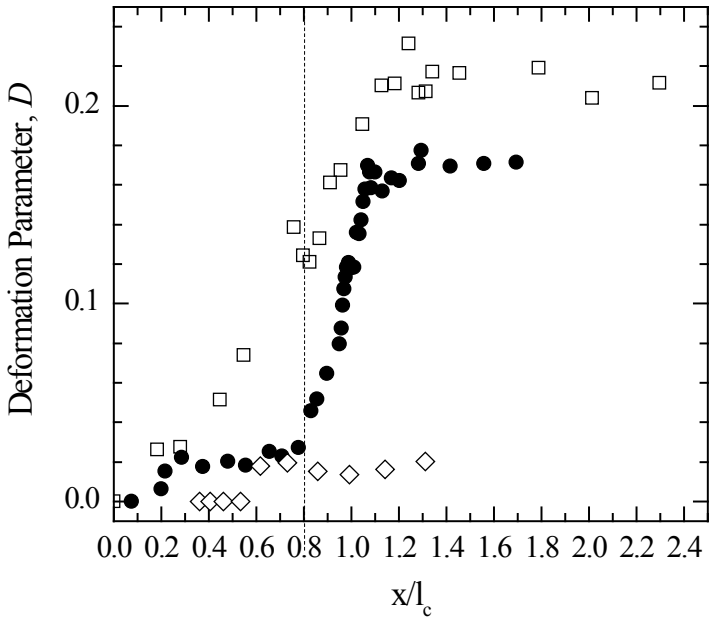

Figure 4-8: Deformation as a function of position normalized by the length of the hyperbolic contraction for two partially-confined droplets, $C = 0.6$ at a capillary number of $Ca = 0.03$ (◇) and $C = 0.9$ at a capillary number of $Ca = 0.07$ (■) and a fully-confined droplet, $C = 1.1$, at a capillary number of $Ca = 0.06$ (○). The dashed line shows where the transition from partially-confined to fully-confined for the $C = 1.1$ droplet occurs.

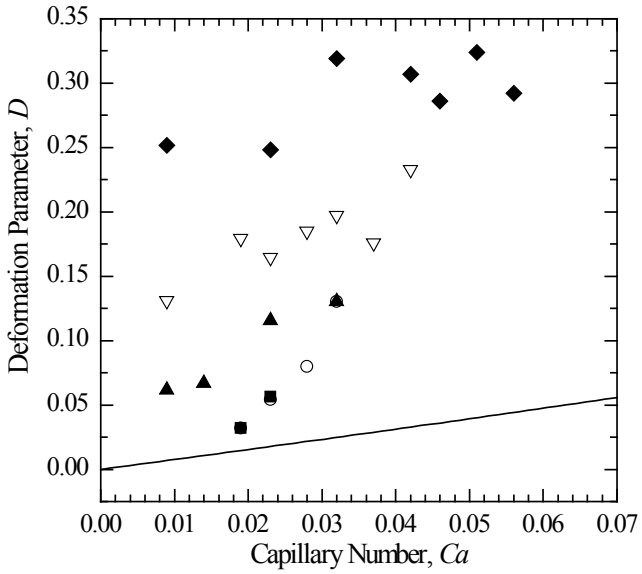

Figure 4-9: Deformation parameter as a function of the extensional capillary number is shown at various confinements for 500 nm amine modified silica particle coated droplets in oil. The data includes confinements of *C*=0.8 (■), *C*=0.9 (○), *C*=1.0 (▲), *C*=1.1 (□), and *C*=1.4 (◆).

However, even though the degree of deformation was similar for the droplets populated by the 500 nm amine modified silica particles, tails were never observed on the droplets and the droplets were never observed to break up into daughter droplets. Tails were only seen to form for the 1μm particle laden droplets for a confinement greater than $C > 1$ and a capillary number greater then about $Ca \cong 0.1$. The lack of tail streaming is likely a result of the higher interfacial tension between the droplets coated with the 500nm particles and the continuous oil phase and therefore the lower range of capillary numbers accessible within the microfluidic devices. It is likely that tail formation and tail streaming will occur at higher capillary numbers, unfortunately higher capillary numbers could not be reached within this experimental device design.

4.4 Buckling and Crumpling of Particle-Laden Interfaces

For highly-confined droplets coated in 1μm particles, an interesting departure from the tails seen for the fully-confined and partially-confined droplets occurs. Shown in Figure 4-10(a)-(b) are droplets for which the elastic particle-laden water-oil interface has buckled. The evolution of the buckling of the interface can be seen prominently in Figure 4-10a, where a tail is forming and breaking off from the trailing edge of the droplet. At the trailing edge of the droplet the interface does not return to an ellipsoidal shape as it pinches off. Instead it remains pointed and creased as the particle-laden interface buckles as it begins to retract after pinch-off. In Figure 4-10b, the process of tail retraction is shown and the evolution of the crumpling interface is illustrated. Note that following the highly confined drop is a daughter drop with a pointed and sharp tail. The sharp points of the daughter droplet and the folded and bent trailing edge of the parent droplet are formed within the contraction and subsequent straight channel. These interface structures are long-lived and can be observed to survive the re-expansion downstream of the hyperbolic contraction.

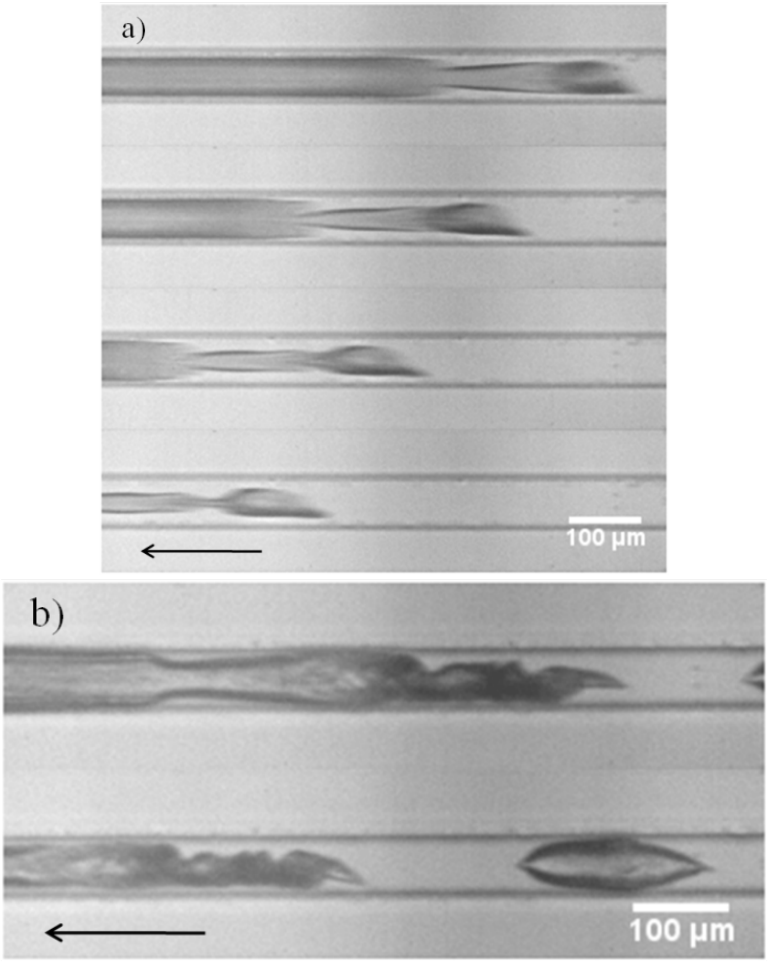

Figure 4-10: Formation of buckled and crumpled tails. a) Formation and evolution of a buckled tail. b) Buckled tail after breakup.

Aside from the buckled and crumpled structures seen in the middle of the contraction, as shown in Figure 4-10, there is also evidence of the long-lived nature of these buckled and crumpled droplets and daughter droplets downstream of the re-expansion in the flow cell. Figure 4-11 shows a representative image of the long-lived buckled and crumpled structures that result from the deformation of highly confined droplets. Unfortunately, the design of our microfluidic device caused most of the droplets to coalesce when they reached the exit reservoir, making it difficult to do any long-term studies on the evolution of the buckled droplets shape with time.

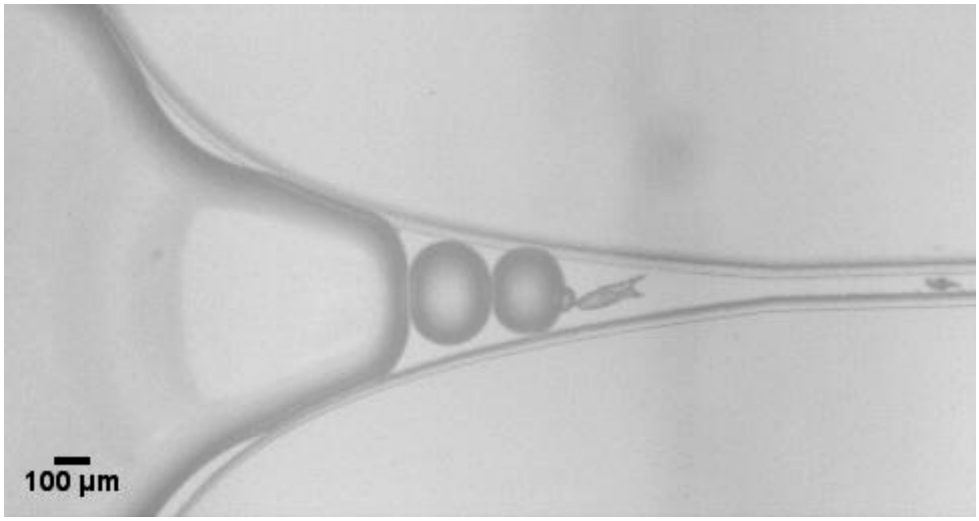

Figure 4-11: Representative images of buckled and crumpled tails droplet daughter droplets down-stream of the re-expansion.

There is evidence in the literature that, under the right conditions, particle-laden droplets, planar interfaces (frequently called particle rafts, sheets or monolayers) and cylinders behave like thin elastic films (Vella, Aussillous et al. 2004; Edmond, Schofield et al. 2006; Datta, Shum et al. 2010). While the dynamics of the interface deformation vary from shape to shape, all these shapes have shown evidence of their elastic nature by undergoing a buckling instability. Buckling instabilities occur when the compressive stress on an elastic membrane exceeds a critical value. In the case of the droplets shown in Figure 4-10, the compressive load is applied by interfacial tension after daughter drops were produced from a parent drop. In this flow, the elastic membrane is initially stretched by the extensional forces present on the droplet. As the droplet is stretched, new interface is produced and populated by particles. When daughter droplets pinch off or when the deformed drops are allowed to relax downstream of the re-expansion, surface tension drives the drop back towards a spherical droplet and in the process reduces the

interfacial area and thereby applies a compressive load on the particle laden interface. Particles, as discussed earlier in this work, are not very mobile and can jam on the interface of the droplets. Unlike surfactants, particles are bound to the interface by thousands of k_BT and are not easily displaced into the water or oil phase (Du, Glogowski et al. 2010). Thus the droplet must either maintain its non-spherical shape or if the compressive stress exceeds a critical value the droplet will buckle and wrinkle as seen in Figure 4-10.

There is also direct evidence of the solid like behavior of particle coated droplets (Datta, Shum et al. 2010). To understand the dynamics of the elastic shell created by coating a droplet with nanoparticles, fluid is controllably pumped out of the interior of the droplet. Droplets are found to buckle and crumple upon the reduction of volume, which confirms the solid like behavior of these elastic shells formed by the particles coating the exterior of a droplet. The dynamics of deformation of a sheet and a shell vary because "unlike the case of a sheet deforming a thin elastic shell requires it to both bend and stretch" (Datta, Shum et al. 2010).

Particle coated interfaces are finding an increasing number of applications in a wide variety of technological and medical uses (Binks 2002; Dinsmore, Hsu et al. 2002; Vella, Aussillous et al. 2004; Du, Glogowski et al. 2010). The increasing use of particle-laden interfaces has to do with the elastic and solid-like behaviors of the interface.

The mechanical properties, including Poisson's ratio, υ, and Young's modulus, E, of a particle-laden air-water interface were studied by Vella, *et al.* (Vella, Aussillous et al. 2004) through a series of buckling experiments. This was done by utilizing the one property of a particle-laden water-air interface which is easily measured; the wavelength

of the wrinkles in the interface. Using a number of assumptions, Vella *et al.* (Vella, Aussillous et al. 2004) were able to correlate the wavelength of the wrinkles to the elasticity of the particle raft. The first assumption was that the particle raft behaves like an isotropic, homogeneous elastic material with a thickness equal to the diameter of the particles used to create the interface. The Poisson's ratio was calculated to be $\upsilon = 1/\sqrt{3}$ through geometrical arguments and finally assuming a hexagonally close packed arrangement of the particles on the interface, the volume fraction, ϕ, was determined to be $\phi = \pi/(2\sqrt{3})$. Using the beam equation, the Young's modulus of the system was determined as a function of wavelength to be

$$E = \frac{3}{4\pi^4}\frac{\rho g(1-\upsilon^2)\lambda^4}{d^3} \tag{4.6}$$

where ρ is the density of the liquid which provides the restoring force to the system, g is the acceleration due to gravity and d is the diameter of the particles populating the interface Vella *et al.* (Vella, Aussillous et al. 2004) experimentally determined that the Young's modulus of the particle raft decreased with increasing particle diameter with the same power law dependence predicted by Equation (4.6). The wavelength of the wrinkles on the buckled interface was found to increase with increasing particle diameter (Vella, Aussillous et al. 2004). Vella *et al.* (Vella, Aussillous et al. 2004) found the Young's modulus varied between $10Pa < E < 100,000Pa$ for particles with a radius of $1000\mu m > d > 1\mu m$. These are relatively soft solids. Note for example that the= Young's modulus of concrete is $E = 25GPa$, while the Young's Modulus of Oak is $E = 12GPa$ (Beer and Johnston 1992). In similar work by Lin *et al.* (Lin, Leahy et al. 2010) nanoparticles were used instead of microparticles. Nanoparticle covered flat-

interfaces were also found to wrinkle under compression. The difference however, is that because of their small size and large modulus, they tend to form multiple layers of particles within a given wrinkle to reduce the bending energy (Lin, Leahy et al. 2010).

In recent work, we have been collaborating with an undergraduate, Colin Pespia, to verify and extend the findings of Vella *et al.* (Vella, Aussillous et al. 2004) for particles at an oil-water interface, rather than an air-water interface. Our goal was to quantify the wavelength and the amplitude of wrinkles on a particle raft located at an oil-water interface. This measurement would allow us to calculate the Young's Modulus of the particle laden interface from Eq. (4.6) and better understand the buckling of the droplets as seen in Figure 4-10.

Using a Langmuir trough, pictured in Figure 4-12, a planar water-oil interface was created using hexadecane and water. The wall pictured on the left, in Figure 4-12, is attached to a micrometer, which when turned compresses the particle-laden interface and induces wrinkling. The amount of interface compressive strain was easily quantified, however compression rate of the interface was not measured as the micrometer was advanced by hand. The strain applied by the micrometer was defined as the engineering strain

$$\varepsilon = \frac{\Delta L}{L} \tag{4.7}$$

where ΔL is the difference between the initial length of the interface and the final length of the interface and $L = 1.5"$ is the initial length of the interface. Deionized water was placed on the bottom of the trough and hexadecane was used as the oil phase. Surfactant free latex particles with a diameter of $d = 3.1\mu m$ (Invitrogen, SKU# S37223, Lot# 466864) were suspended in a solution of four parts alcohol to five parts water, as done by

Reynaert *et al*. (Reynaert, Moldenaers et al. 2006). This mixture was injected by a syringe at the location of the interface, thus reducing the diffusion time of the particles to the interface. The alcohol is a cosolvent for water and oil. After injection the interface loses its sharpness becoming diffuse. Over time the alcohol diffuses into the oil and water phases, away from the interface, leaving the particles behind to form a sharp, particle covered oil-water interface. The total time for the interface to form was found to be less than five minutes.

a)

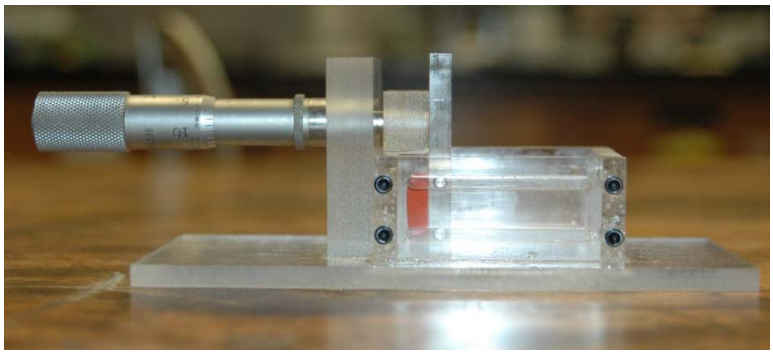

b)

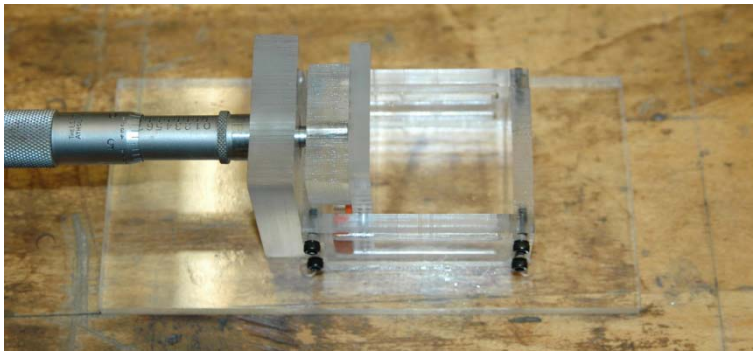

Figure 4-12: Pictures of the Langmuir trough used to study the wrinkling of particle rafts at the water-oil interface. (a) shows a side view and (b) shows a top view of the Langmuir trough.

The concentration of particles used to create the particle rafts was much larger than that needed to populate the entire interface. This was done to ensure full coverage of the oil-water interface with particles. Vella *et al*. (Vella, Aussillous et al. 2004)

predict that the wavelength at the onset of wrinkling for a $d = 3.1\mu m$ particle at the air-water interface will have a wavelength of about $\lambda \approx 350\mu m$. We find that the onset of wrinkling for a $d = 3.1\mu m$ occurs at a compressive strain of 0.35 and has a wavelength of $\lambda = 548\mu m$. As seen in Figure 4-13, the wavelength of the wrinkles was found to decrease roughly linearly with increasing strain. After the onset of wrinkling, the amplitude of existing wrinkles increases with increasing strain, but the appearance of new wrinkles is not observed. The wrinkles are simply found to compress. Additionally, no plateau or change in slope in the data is observed in Figure 4-13 that would suggest that the interface is folding upon itself to localize strain and create layers of particles as seen in Leahy *et al*. (Lin, Leahy et al. 2010). To measure the wavelength of the wrinkles of the particle laden interface, a laser light sheet was shown on the interface and the wrinkles were counted. Representative images of this data can be seen in Figure 4-14.

The wrinkled interface was looked at from a variety of different angles. A number of pictures showing wrinkles and buckling of the particle-laden interface can be seen in Figure 4-15. In Figure 4-15a, the regular pattern of the wrinkles can be seen. The wrinkles at this point in the compression are nice and regularly spaced. In Figure 4-15b, a particle raft which has transitioned from wrinkling to buckling is pictured. In Figure 4-15c, one can see the wrinkled and buckled surface with a section of the surface which is perpendicular to the particle raft. This perpendicular section, which we will call a "leaf", was created by poking the compressed interface with a blunt syringe tip and then removing the syringe tip. This leaf demonstrates the elastic nature of the interface by showing a wrinkled and buckled portion of the particle raft. These images are used to

demonstrate the wrinkling, buckling and elastic nature of the particle rafts, which will be explored further.

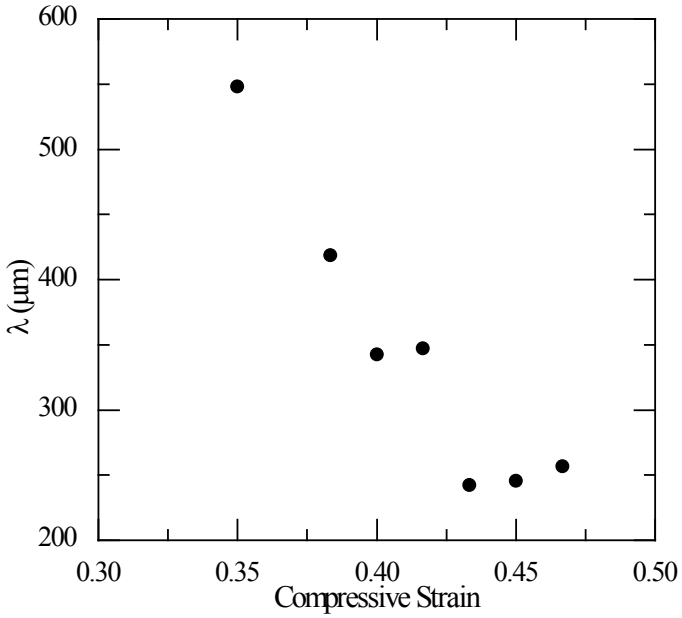

Figure 4-13: Graph showing compressive strain vs. wavelength for a fully populated particle raft at the oil-water interface.

The Young's modulus, calculated using Equation (4.6), was found to be $E = 34,600Pa$ at a wavelength of $\lambda = 548\mu m$.

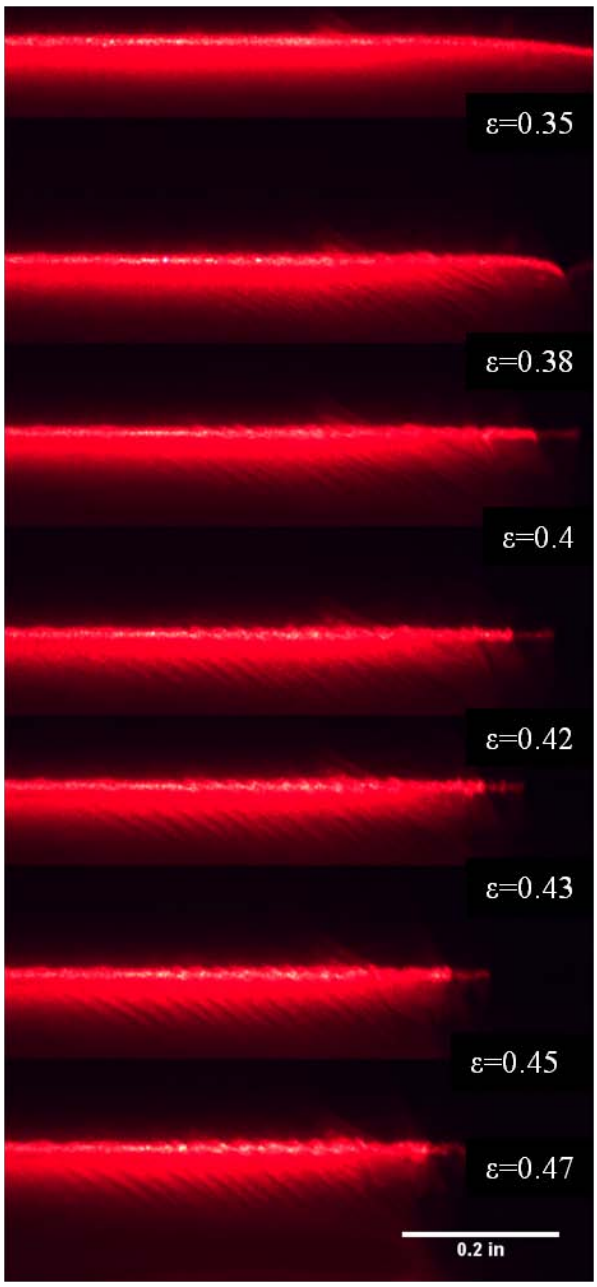

Figure 4-14: Picture of the interface at various compressions illuminated by a laser light sheet. Compression increases from top to bottom and the wrinkles can be seen at the bottom of each image.

There is more work to be done to understand the elastic nature of this particle-laden interface. Design improvements will be made the Langmuir trough to create a more exact interface. A measurement technique will be developed for determining the

amplitude of the wrinkles. The onset of wrinkling, wavelength and amplitude of wrinkles will be studied for a variety of particles sizes and for varying volume fractions of particles on the interface.

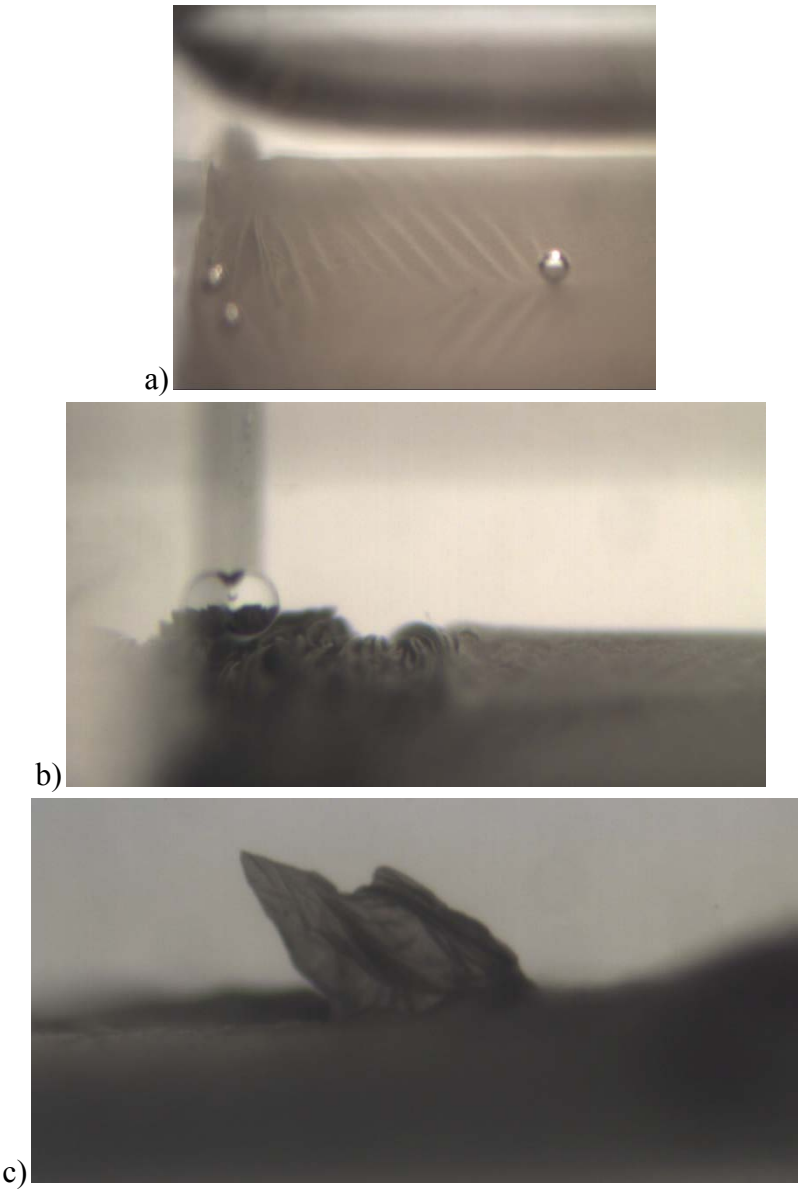

Figure 4-15: Representative images of (a) wrinkled particle raft at the oil-water interface, (b) a buckled particle raft at the oil-water interface and (c) a wrinkled and buckled leaf pulled from the interface by a syringe tip.

4.5 Particle-Laden Droplet Conclusions

In this manuscript, the deformation and breakup of particle laden droplets in a confined extensional flow was studied using a microfluidic hyperbolic contraction. In these experiments, the effect of confinement is studied to investigate an individual emulsion droplet under conditions that approximate a concentrated emulsion. The deformation of particle coated droplets was found to deviate significantly from the predictions of Maffetone and Minale for unconfined droplets. This deviation is due in part to shear flow superimposed on top of the extensional flow from droplet confinement. Initially, droplets deformed from a spherical to an ellipsoidal-shaped droplet as predicted by the model. However, at high confinement and capillary numbers there were a variety of interesting shape transitions observed including: bullet-like shapes with a rounded tip and a flattened trailing edge; droplets with one and two tails extending from the back of the droplet from which daughter droplets eventually streamed; and finally, at a very high confinement and capillary number, buckling, wrinkling and creasing of the droplet interface. This final transition is the result of the finite elasticity of the particle laden membrane which formed along the interface of the droplet as particles jam the surface and has been observed to occur previously on flat particle-laden interafaces. (Vella, Aussillous et al. 2004). For both surfactant and particle-laden droplets tail streaming is the result of a local reduction in surface tension at the rear of the droplet due to surfactants or particles being swept by the flow to the rear of the droplet. Although, tail streaming has been observed many times in the past for surfactant droplets (De Bruijn 1993; Mulligan and Rothstein 2011). These observations of tail formation and streaming from the rear of a particle laden droplet are, to our knowledge, the first of its kind.

Droplet deformation was found to increase with increasing confinement and capillary number for both the 1μm and 500nm amine modified silica particles studied. The deformation of the droplets was compared to the Maffetone and Minale model for unconfined droplets undergoing pure extensional flow. For the partially-confined droplets $C < 0.7$, the deformation was found to follow the Maffetone and Minale model. However, for the nearly-fully-confined and fully-confined droplets, $C \geq 0.9$, the droplet deformation deviated strongly from the Maffetone and Minale model within the range of capillary numbers studied. In some cases, droplet deformation was as much as three times that predicted by the Maffetone and Minale model for unconfined droplets. For the nearly-fully-confined and fully-confined droplets deformation was found to increase with increasing capillary number. For moderately confined droplets the deformation followed the Maffetone and Minale model until a critical capillary number, after which a strong increase in deformation occurred due to the above mentioned shape transition. This critical capillary number was found to decrease with increasing confinement.

Droplets which were fully-confined and coated in 1 μm silica particles were seen to have tails near the confining walls, for fully confined droplets only. This is in contrast to surfactant droplets for which tail streaming occurred even for partially confined droplets (Mulligan and Rothstein 2011). It is not clear whether full confinement is a necessary requirement for tail formation or if tail formation might happen for lower moderately confined drops if one could reach much larger capillary numbers. This question we hope to answer in the near future. Above a critical capillary number, daughter droplets were produced from these tails. For the 500 nm particle coated droplets, tail streaming was not seen in the range of capillary numbers studied, although it

is likely that if higher capillary numbers could have been achieved droplet breakup would have been observed.

In the case of highly-confined droplets, a buckling instability occurred when the daughter droplet pinched off from the parent droplet. As the droplets were deformed from spheres to ellipsoids, the interfacial area grew and was populated by particles. Unlike surfactants, which can easily move from the interface to the bulk, once at the interface particles are kinetically trapped. The compressive stress required for buckling to occur was generated by the pinch off of the daughter droplet, as the interfacial tension acting on the now unconfined daughter droplet acted to drive the droplet towards a spherical shape from its original non-spherical higher surface area shape. The buckled structures were found to be long-lived and were observed to withstand the downstream re-expansion within the microfluidic devices used in this study. It is clear that the elasticity of the jammed particle interface is responsible for the observed buckling as buckled structures were not seen for surfactant covered droplets (Mulligan and Rothstein 2011).

CHAPTER 5

PARALLEL MICROFLUIDIC DROPLET FORMATION VIA FLOW-FOCUSING GEOMETRY

Droplets were produced in a series of six parallel microfluidic flow-focusing devices on a single microfluidic chip. A single inlet channel was used for the dispersed surfactant solution phase and the continuous oil phase. Exit tubing for each of the six flow-focusing droplet generators was plumbed to each channel, to allow for maximum control over droplet size, production frequency and end placement of the droplets produced. The effect of exit tubing length was studied to determine the effect of tubing length on droplet size and production frequency. Longer exit tubing lead to larger droplets which were produced more frequently, most likely resulting from a higher dispersed phase flow rate and a lower continuous phase flow rate, which resulted in smaller shear stresses.

5.1 Parallel Microfluidic Droplet Generation

Droplet generation in microfliudic devices is a well-understood and studied phenomena, which is attracting increasing attention owing to a variety of potential applications in biology, medicine, chemistry and a wide range of industries (Shu, Eijkel et al. 2007; Dollet, van Hoeve et al. 2008; Li, Young et al. 2008). Microfluidic devices are capable of producing monodisperse droplets, which lends itself to a variety of industrial emulsification applications if the process can be scaled up to produce large quantities of precisely controlled monodisperse, bidisperse or even polydisperse emulsion droplets (Anna, Bontoux et al. 2003; Miller, Rotea et al. 2010).

Previously, several papers have discussed the process of scaling up microfluidic devices for producing emulsion droplets in the industrial setting, which requires a higher output of droplets from the microfluidic devices (Barbier, Willaime et al. 2006; Garstecki, Hashimoto et al. 2008; Li, Young et al. 2008). While it has been demonstrated that using a single microfluidic droplet creation device monodisperse and other precisely controlled droplet distributions can be generated, the interplay between multiple droplet creation devices is still under investigation (Barbier, Willaime et al. 2006; Garstecki, Hashimoto et al. 2008; Li, Young et al. 2008). A single microfluidic droplet creation device typically has flow rates on the order of tens to hundreds of microliters per minute, which is not a high enough throughput for industrial applications (Barbier, Willaime et al. 2006). Practically, industrial applications need much larger production rates and a system that allows for a minimal amount of "plumbing", input and output tubing. Ideally, a parallel microfluidic droplet creation device would have a single input for both the dispersed and continuous phases of the emulsion and individual outlets allowing for droplets of different sizes to be sent to different locations or all to the same location.

Using the T-junction method of droplet formation, Barbier *et al.* (Barbier, Willaime et al. 2006), study the behaviors of two parallel droplet production devices. The dynamics of droplet formation in this device were described as complex, oweing to the fact that there were several different modes of droplet formation including synchronization, quasi-periodic and chaotic droplet production. Droplet production frequency was found to increase with the increase in the water, dispersed, phase flow rate, as is typical for T-junction droplet creation devices. In the synchronized droplet creation regime monodisperse droplets were produced. This type of droplet creation was

achieved but having the legs of the two T-juntions be identical in length. For the quasi-periodic droplet formation mode, when both legs of the T-junction are the same length, the droplets have a polydisersity on the order of 8% in each leg of the device. In the chaotic regime, droplet polydispersity ranged from 30-60% When the T-junction legs were different length the polydisperity of droplet production was large and droplet production was chaotic and not snychonized. (Barbier, Willaime et al. 2006)

Garsetcki *et al.* (Garstecki, Hashimoto et al. 2008) looked at the process of scaling up microfluidic flow-focusing droplet creation devices. Using a common inlet for the continuous phase solution, a common outlet for the droplets produced and individual inlets for the dispersed phase fluid, Garstecki *et al.* (Garstecki, Hashimoto et al. 2008) sought to understand the coupling dynamics of droplet and bubble generation in parallel microfluidic flow-focusing droplet production. It was found that the mechanism of interaction between the coupled droplet generators depended on the compressibility of the dispersed phase fluid. Parallel bubble formation, using gas as the dispersed phase, was found to have complicated formation dynamics due to the compressibility of the gas dispersed phase. Droplet formation was not found to be coupled over the range of flow rates studied. (Garstecki, Hashimoto et al. 2008)

An interesting application of microfluidic droplet creation devices is using these devices to create monodisperse microparicles (Xu, Nie et al. 2005). A recent study focused on using parallel droplet generation using a flow-focusing droplet creation geometry to create polymer microparticles in parallel (Kumacheva, Li et al. 2009). Common inlets were used for the continuous phase and dispersed phase that fed into each of the parallel droplet generators, and a common outlet was used for the particles

produced in the parallel droplet creator. This work found that microfluidic devices could be used to produce polymer microparticles at a rate of 50g/h with a maximum polydispersity of 5%. In this work, where all devices were fed through common inlets and outlets, there was found to be coupling between the parallel microfluidic droplet generators. This coupling was due to the hydrodynamic coupling between the parallel-connected streams. The pressure variations caused by droplet formation in a single droplet generator affected the adjacent droplet generators and caused a broadening of the size distribution of droplets generated. It was also found that by varying the length of the dispersed phase inlet polydispersity of droplet size could be controlled, but this also depended upon flow rate ratio. (Kumacheva, Li et al. 2009)

Li *et al*. (Li, Young et al. 2008) looked at the coupling between four parallel flow-focusing droplet generators with all the same dimensions and then with four different droplet generators which had differently sized orifices for droplet generation. While, the droplets could be considered monodisperse by NIST Size Standards (Li, Young et al. 2008), the broadening in the size distribution of droplets produced in the four identical droplet generators was attributed to the coupling between the droplet generators due to droplet formation in an adjacent droplet generator. For parallel droplet generation when the four droplet generators had different orifice dimensions monodisperse droplets were produced over the entire range of flow rates for the two droplet generators with the widest orifices. For the droplet generators with the two narrowest orifices, at low flow rates each generator created droplets of different sizes each with a small polydispersity. For flow rate ratios between eight and ten all four droplet generators produced the same size monodisperse droplets. (Li, Young et al. 2008)

In this work we seek to explore the dynamics of parallel flow-focusing droplet generators which a common inlet for the dispersed and continuous phases and individual outlets which allows for the tuning of the outlet-tubing lengths for each droplet generator. Using separate outlets for each droplet generator in parallel, the pressure drop in each individual flow-focusing droplet generator can be controlled and allows for the collection of droplets in individual containers or one single container. This also allowed for the fabrication of a single layer poly-dimethyl siloxane (PDMS) device, allowing for easy fabrication processes.

5.2 Parallel Microfluidic Droplet Generation Experimental

The experimental flow cell is shown schematically in Figure 5-1a. The flow cell was designed to have six parallel flow-focusing droplet generators with identical dimensions. Shown schematically in Figure 5-1b is one of the individual flow-focusing geometries. The relevant dimensions of the individual droplet generation devices are labeled in Figure 5-1b. Parallel microfluidic droplet generators were fabricated in PDMS using standard soft lithography methods and a PDMS ratio mismatch for sealing (Anderson, Chiu et al. 2000; McDonald, Duffy et al. 2000; McDonald and Whitesides 2002; Miller, Rotea et al. 2010; Mulligan and Rothstein 2011). The masks used for the fabrication of master wafers were printed on a high-resolution transparency with a resolution of 20,000 dpi, thus allowing for features as small as 10 μm. The size of the devices was limited by the area of the silicon wafer.

All experiments were carried out on an inverted microscope (Nikon TE2000-U, Melville, NY) and video data was recorded using a high-speed CCD video camera

(Vision Research, Phantom 4.6, Wayne, NJ). The continuous phase fluid for all experiments was Light mineral oil, which has a viscosity of μ_c=47 mPa·s (Fisher Scientific Brand). The dispersed phase was a 5mM cetylpyridinium chloride (CPyCL) in water. Flow through the parallel droplet generators was driven by two stepper-motor actuated micro-syringe pumps (New Era Pump Systems, NE-500 OEM, Wantagh, NY). The flow of the dispersed phase, Q_d, was held constant through-out the experiments at $Q_d = 20\mu L/\min$ and the continuous phase flow rate, Q_c, was varied.

a)

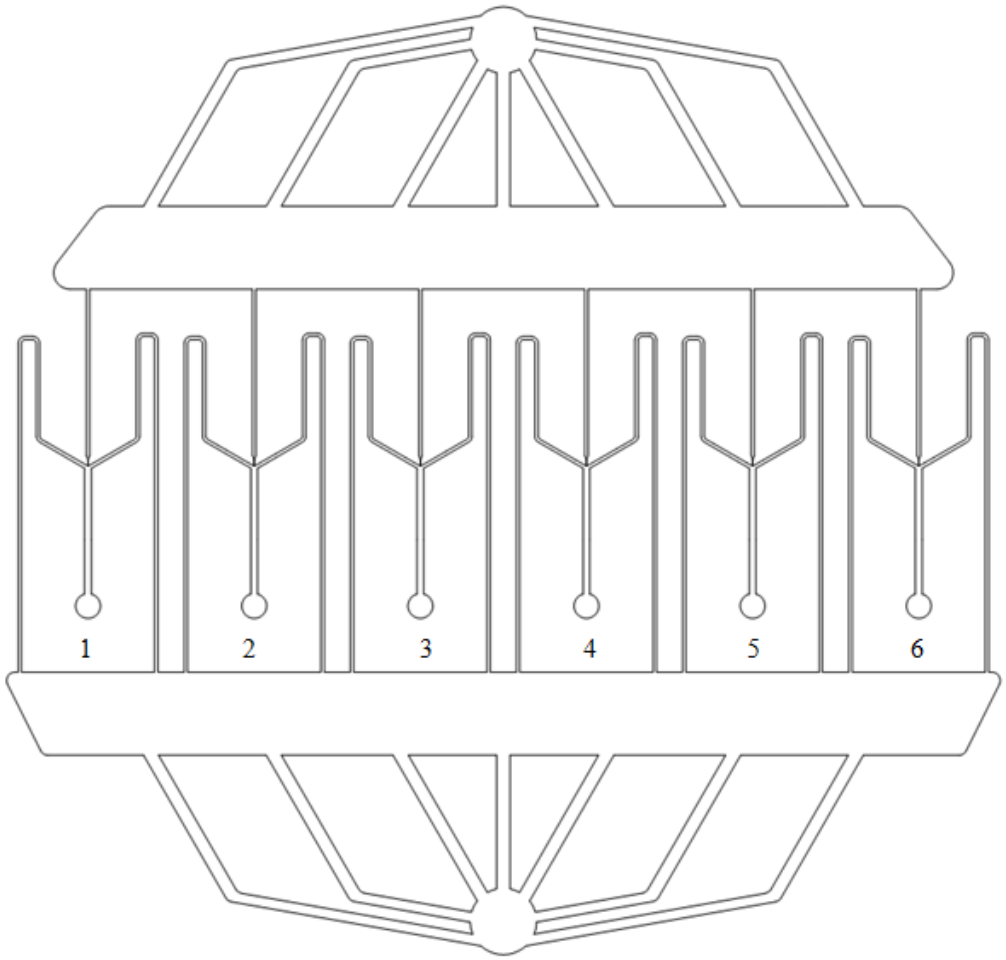

b)

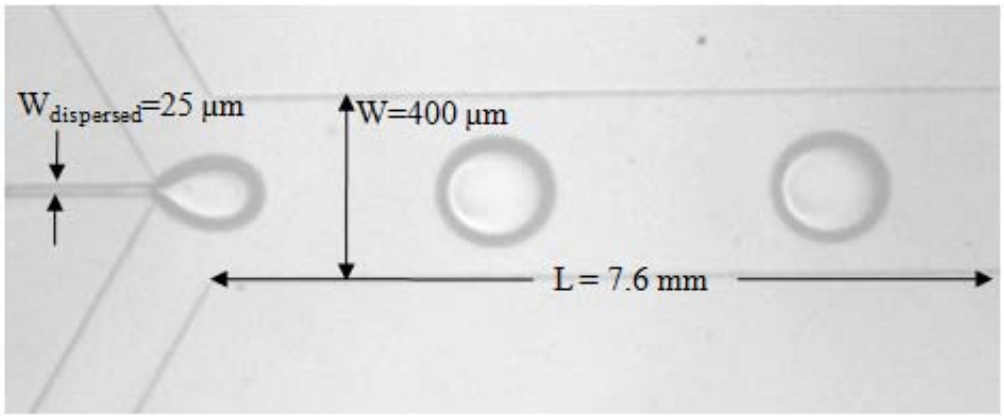

Figure 5-1: (a) Schematic of the six parallel flow-focusing device geometry with a common inlet for the dispersed and continuous phase fluids. (b) Picture of a single flow-focusing device with the relevant dimensions labeled.

5.3 Parallel Microfluidic Droplet Generation Results and Discussion

Using the microfluidic device shown in Figure 5-1, droplets can be produced in the six parallel flow-focusing devices simultaneously. Within a single channel, the droplets were found to be monodisperse with small variations of less than one pixel, as is shown in Figure 5-2. This corresponds to a 5μm variation over droplets as big as a 180μm in radius. In this case data is presented for channel number two and all the exit tubing is set to 10cm. In the case of the highest two flow rate ratios studied, $Q_r = Q_c / Q_d$, all droplets were measured to have the same radius, where Q_c is the flow rate of the continuous oil phase and Q_d is the flow rate of the dispersed water phase.

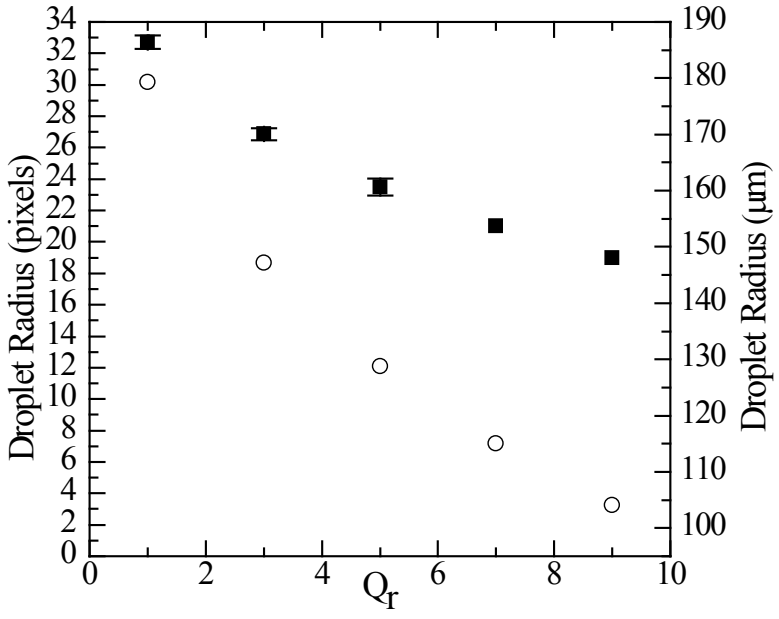

Figure 5-2: Droplet radius as a function of flow rate ratio, Q_r, for a single microfluidic flow-focusing device within the larger chip. The radii of the droplets are shown in pixels (■) and in micrometers (○), along with errors bars.

For scale-up, the variation of droplet size across all the channels should be small. In Figure 5-3, the average size and standard deviation of droplets at a given flow rate across all six flow-focusing devices is shown. Again the exit tubing in each case is equal in length and set to 10cm. When all six of the droplet creation devices are taken into account, the range of droplet sizes has a larger variation than that found for a single flow-focusing droplet creation device. At a flow rate ratio of $Q_r = 1$, the radii of the droplets varied between $155 \le r \le 179 \mu m$. The average droplet radius was $r = 172 \pm 9.1 \mu m$. When inspecting the size variation across the device, it is clear that the edge effects of the large reservoirs used to supply the oil and water phases to each of the channels plays a role in the flow of the water and oil phases. This was because the two outer-most flow-focusing devices, device numbers one and six, showed the largest deviation in the data. Shown in Figure 5-4 is a plot of the droplet radius as a function of the flow rate, Q_r, for all six channels in a single device with the exit tubing set to 10cm for all channels. The dispersed phase flow rate supplied by the pumps was set $Q_d = 20 \mu L / \min$ in all of these cases. One would like to assume that the flow rate of the dispersed phase, and the continuous phase, in each of the channels is one sixth of the total input flow rate. However, it is evident that that is not the case owing to the fact that droplet radii and droplet production frequency are not equal. Channels one and six have the largest variation in dispersed phase flow rate over the range of flow rate ratios tested. This can be an issue if one is to implement such a scale-up scheme to achieve monodisperse droplet distribution. However as we will see later, the length of the exit tubing can be used to change the pressure drop in an individual channel and therefore change the fraction of the total flow rate in the channel.

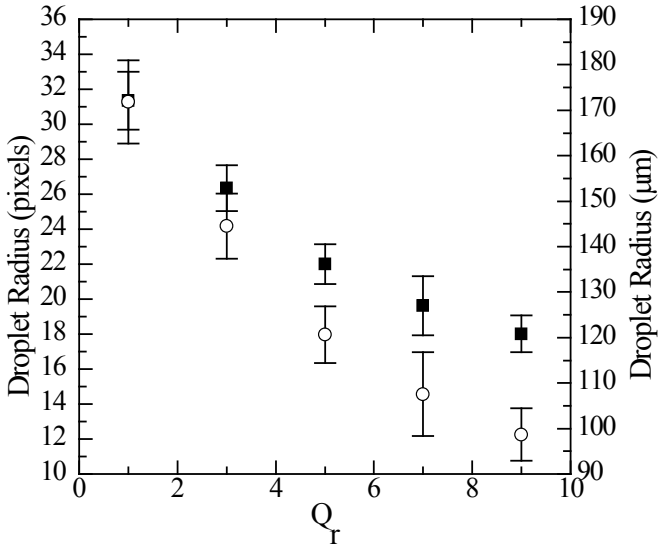

Figure 5-3: Average droplet radius as a function of flow rate ratio for all six microfluidic flow-focusing devices on the chip. The radii of the droplets are shown in pixels (■) and in micrometers (○), along with errors bars.

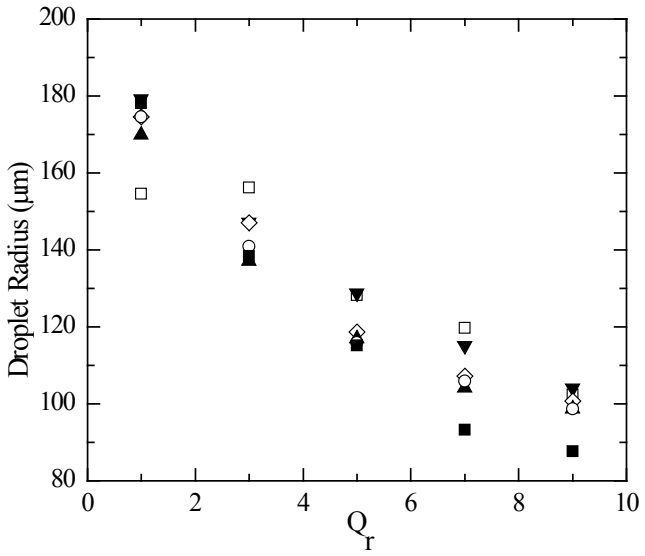

Figure 5-4: Droplet radius as a function of flow rate ratio for all six microfluidic flow-focusing devices on the chip with exit tubing length equal to 10cm for all channels. The symbols for each channel are as follows: one (□), two (▼), three (◇), four (▲), five (○) and six(■).

If one removes the outer two channels, the standard deviation of droplet size across all channels at each flow rate decreases significantly, as can be seen in Figure 5-5. For a flow rate ratio of $Q_r = 1$, the droplet radius across channels two through five varies between $170 \le r \le 179 \mu m$ with a standard deviation of 3.8, a decrease in standard deviation by a factor of 2.4.

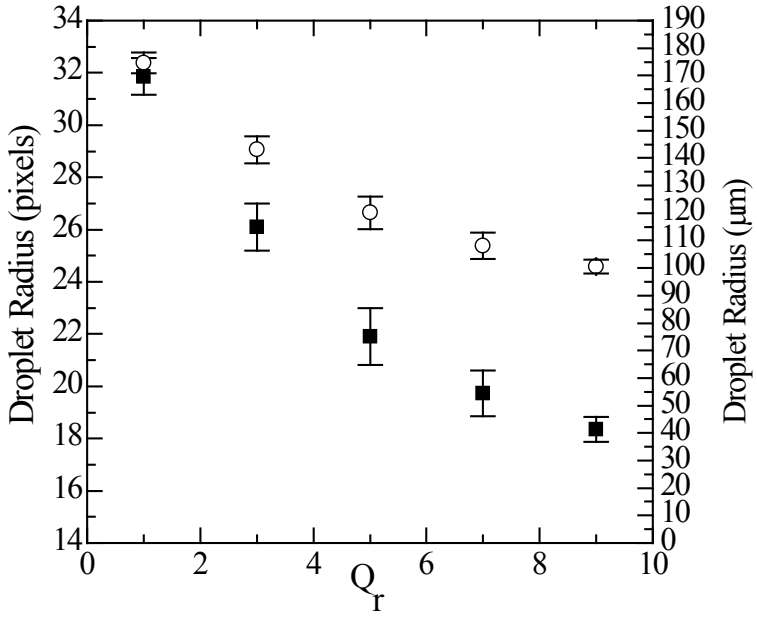

Figure 5-5: Average droplet radius as a function of flow rate ratio for the inner four microfluidic flow-focusing devices on the chip. The radii of the droplets are shown in pixels (■) and in micrometers (○), along with errors bars.

Shown in Figure 5-6, is the frequency of droplet production for all six channels when all channels have an exit tubing length of 10cm. At the lowest flow rate ratio, droplet production frequencies in each channel are all around the same frequency with a standard deviation of 1.2 for $Q_r = 1$ and 1.9 for $Q_r = 3$. As the flow rate ratio increases,

droplet production frequencies increase in each channel but the spread in frequencies is also found to increase.

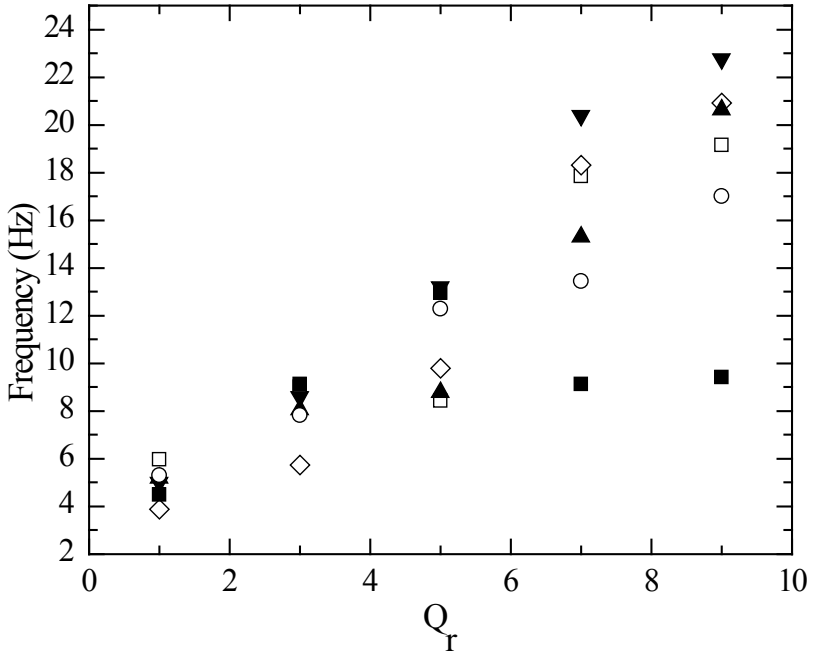

Figure 5-6: The frequency of droplet production in each channel when all of the channels have equal length exit tubing of 10cm. The symbols for each channel are as follows: one (□), two (▼), three (◇), four (▲), five (○) and six(■).

It has been shown that droplets can be produced across all six droplet generators simultaneously and that the droplets radii varied by 5% to 6% across the inner four flow-focusing devices. The goal, however, is to tune the flow cell by adjusting the length of the exit tubing for the different flow focusing devices such that all channels are producing monodisperse droplets, meaning that the radii of the droplets have less than 5% vartiation across all six channels, not just the inner four channels. All data thus far is presented for devices which have equal length exit tubing, which would lead to equal pressure drops within in all six channels if the flow rates were identical in each channel. However, we

have already seen that the flow rates are not identical in each of the six channels, even when the exit tubing is the same length. The pressure drop across all of the channels is equal. Pressure drop was calculated in an individual channel by

$$-\Delta p = \frac{3\frac{Q}{6}\eta l}{4ba^3}\frac{1}{1-\frac{192a}{\pi^5 b}\sum_{i=1,3,5}^{\infty}\frac{Tanh(i\pi b/2a)}{i^5}} \tag{5.1}$$

where Q is the total volume flow rate input into the system, η is the viscosity, l is the length of the channel, b is half the height of the channel, a is half the width of the channel and p is the pressure. For the circular outlet tubing with a radius of $r_{tube} = 0.0265\text{mm}$, the pressure drop across the exit tube was found by

$$-\Delta p = \frac{8Q\eta l}{6\pi r_{tube}^4}. \tag{5.2}$$

For a given flow rate, increasing the exit tubing length from 10cm to 100cm should produce a factor of ten increase in pressure drop. More precisely for a given change in pressure drop the result is a five times decrease in flow rate. Holding all tubing lengths equal to 10cm, except for channel four, which was varied from 100cm to 10cm, it was found that the channel, with the longest exit tubing, produced the largest droplets. This most likely resulted from the fact that channel four had the largest volume flow rate of the dispersed phase. When the outlet tubing on channel four was 100cm long droplets with a radius of $r = 175 \pm 0\mu m$ were produced for a flow rate ratio of $Q_r = 1$. The average droplet radius at the same flow rate for the other five channels was $r = 167 \pm 10\mu m$. The flow rate of the dispersed phase fluid within channel four when droplets were produced was the highest of all six channels. Beyond a flow rate ratio of $Q_r > 1$, no droplets could be produced in channel four, which is likely due to the large flow resistance. This

observation is an upper bound for how much variation in exit tubing length can be implemented and how tunable these devices are.

Shown in Figure 5-7, is the droplet radius for all six flow focusing devices with tubing lengths varying continuously from 20cm to 30cm. By tuning the length of the exit tubing, the droplet sizes can be adjusted. Channel six is an outlier in this data likely indicating a clog or other issue with the device. This is a case where the exit tubing length can be adjusted so that the radii of the droplets in channel six are closer in size to those in the other channels. Adjusting exit tubing length to vary droplet size and polydispersity is simpler than redesigning a droplet production device for each emulsion that needs to be produced.

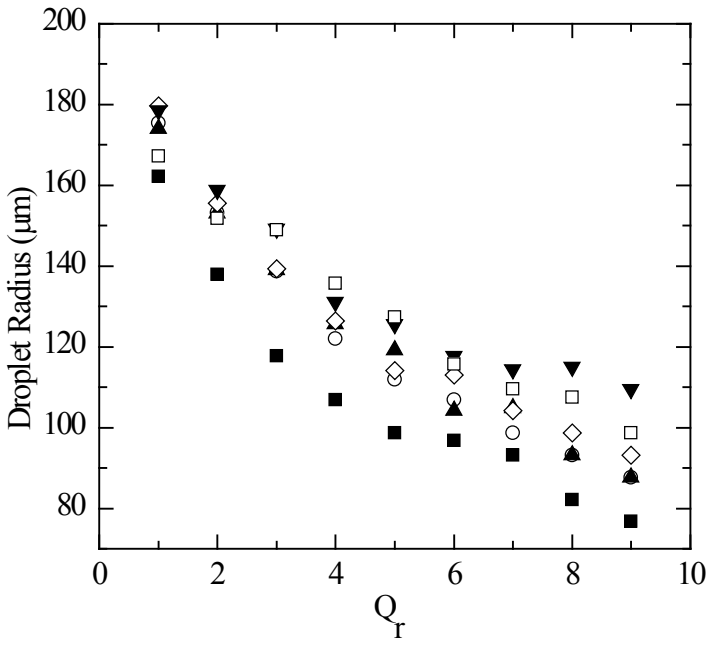

Figure 5-7: Droplet radius as a function of flow rate for all six microfluidic flow-focusing devices on the chip with outlet tubing length varying from 20 cm to 30 cm from channels 1 to 6. The outlet tubing length for channel 1 was 20 cm (□). The outlet tubing length for channel 2 was 22 cm (▼). The outlet tubing length for channel 3 was 24 cm (◇). The outlet tubing length for channel 4 was 26 cm (▲). The outlet tubing length for channel 5 was 28 cm (○). The outlet tubing length for channel 6 was 30 cm (■).

Shown in Figure 5-8 by a solid square is the average droplet radius for all channels except channel four which is shown by the open circles. In this case, channel four had an outlet tubing length of 50cm. It can be seen that channel four produced the largest droplets except in the case of the highest flow rate ratio, $Q_r = 9$, where the droplet size in channel four was equal to the average droplet size in the other five channels. With a longer outlet tube the total flow rate within the channel is reduced, thereby lowering the shear stress in the channel and allowing for larger droplets to be produced. In the absence of tip streaming, it has been shown that with an oil continuous phase and a water or surfactant solution dispersed phase, the average droplet radius decreases with an increasing total flow rate, $Q_{Total} = Q_c + Q_d$, at a fixed flow rate ratio, Q_r (Miller, Rotea et al. 2010). Therefore, a lower total flow rate leads to larger droplet radius because the shear on the dispersed water phase is smaller. Interestingly, the flow rate of the dispersed phase is highest in channel four in this case, even as the total flow rate is reduced. This is likely due to the difference in viscosity between the dispersed and continuous phases. The viscosity of the dispersed phase is $\eta_{water} = 1 mPa \bullet s$ and the viscosity of the continuous phase is $\eta_{oil} = 47 mPa \bullet s$. As a result, an increased volume fraction of the dispersed phase will reduce the overall pressure drop in the channel.

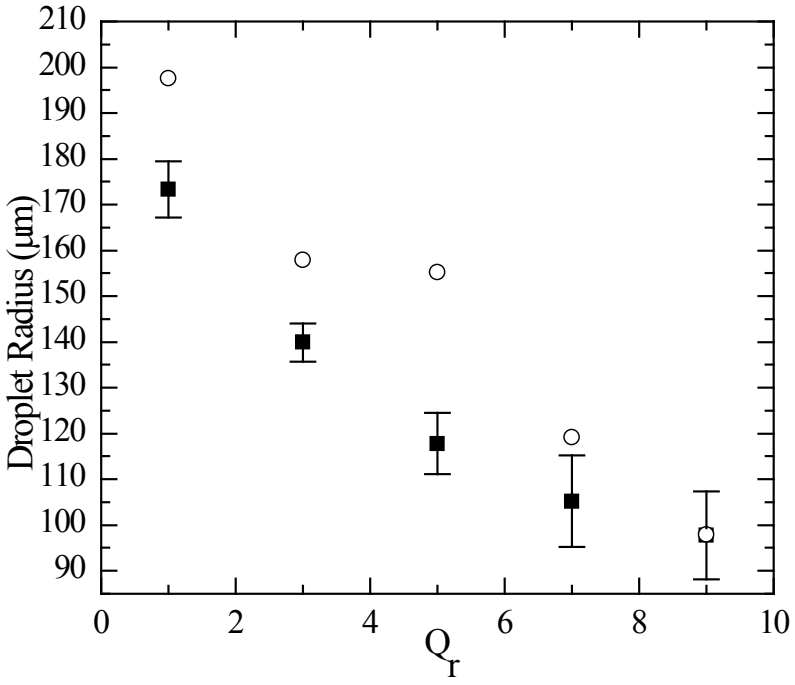

Figure 5-8: Average size of droplets in all channels with 10cm outlet tubing (■) except channel 4 (○) which has a 50 cm long exit tube.

Figure 5-9 shows a representative image of droplet formation in all six channels when the exit tubing lengths are equal, Figure 5-9a, and when the length of the tubing exit in channel four is 50cm, Figure 5-9b.

a) 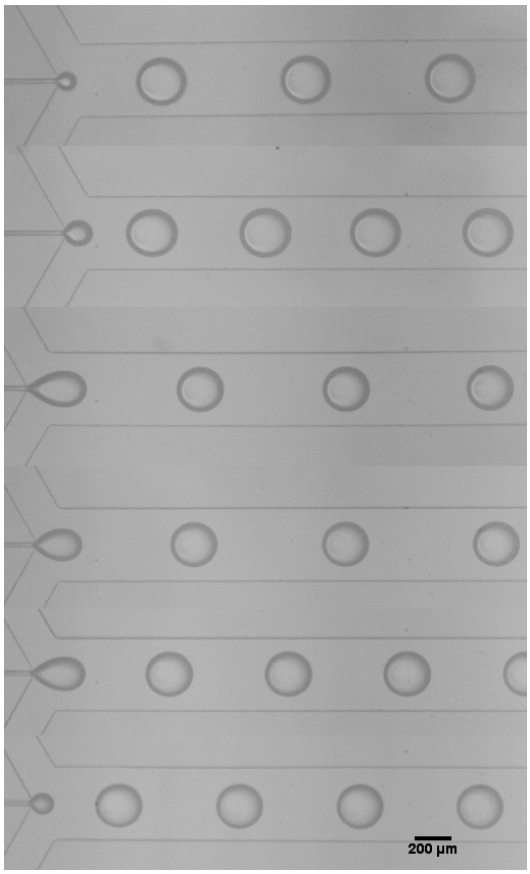

b) 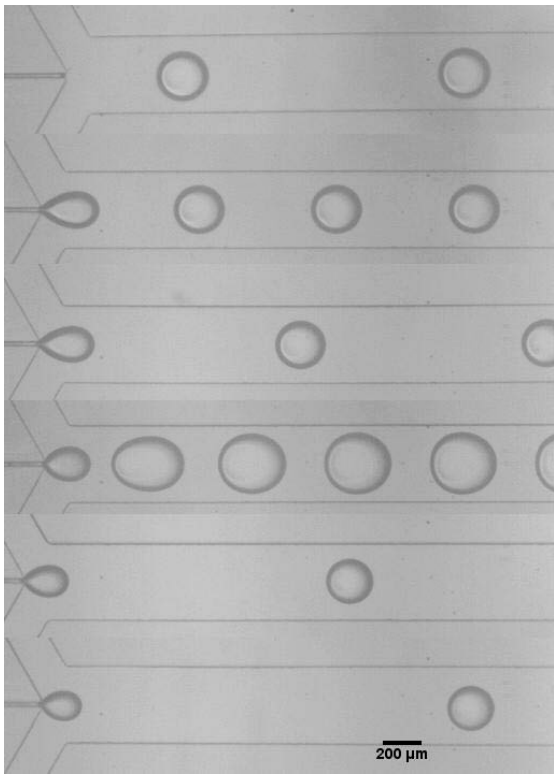

Figure 5-9: Representative images of the droplets in each of the six flow-focusing channels within the parallel droplet generation device. (a) Shows droplet formation when all the exit tubes have an equal length of 10cm at a flow rate ratio of $Q_r = 5$. (b) shows droplet formation when all of the exit tubes are 10cm long except channel 4 which is 50cm long at a flow rate ratio of $Q_r = 5$.

Shown in Figure 5-10 is the frequency of droplet production for all six channels when all channels have an outlet tubing length of 10cm, except for channel four, which has an outlet tubing length of 50cm. Channel four has the largest frequency of droplet production for all flow rate ratios tested.

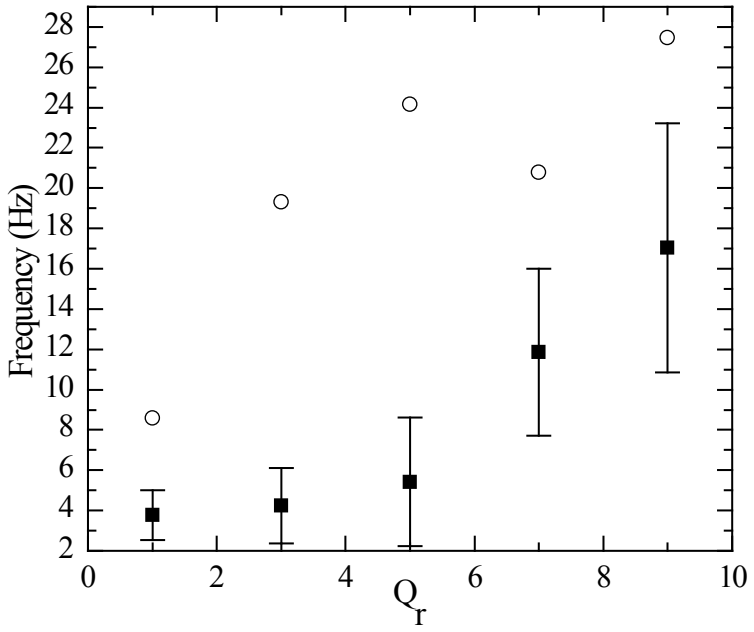

Figure 5-10: The average frequency of droplet production in all channels with 10cm exit tubing (■) except channel four (□) which has an exit tubing length of 50cm.

5.4 Parallel Microfluidic Droplet Generation Conclusions

Using a series of six flow-focusing devices in parallel, droplets were created simultaneously in all six devices on a single chip. The need to create droplets in parallel droplet generators arises from the need for higher output of droplets from microfluidic devices so that these devices can be utilized in industrial settings. This design has a single input for the continuous and dispersed phases and separate exit tubes for each of the flow-focusing channels on the chip. As shown previously, having separate exit tubes allows the users to tune the size of the droplets in individual channels. Also, the use of individual exit tubes for each flow-focusing device allows the user to separate droplets of different sizes into different containers, or put all of the droplets created into one container.

When all six channels had equal length exit tubing, it was found that the outer two channels of the device, channels one and six, had the largest variations from the average droplet size and would require additional tuning depending on the parameters of the emulsion to be made, monodisperse or polydisperse. By varying the tubing length in one channel by factors of ten and five, it was found that larger droplets were produced with a higher frequency in the channel with the longer outlet tubing, however as tubing length was reduced and the flow rate increased, the radii of the droplets produced in channel four eventually matched the average size of the droplets produced in the other five channels.

Droplet production frequency was found to be close at the lowest flow rate ratios tested, $Q_r = 1$ and $Q_r = 3$, when all of the outlet has a length of 10cm. However, as the flow rate increased, droplet production frequency increased and the spread in droplet production frequency became significantly larger. When channel four had a 50cm exit tube, the droplet production frequency in channel four was significantly higher than that seen in the other channels. Scaling-up microfluidic devices for high output droplet production is possible and using the device presented here, can be done with minimal "plumbing" of tubing and a high degree of control over droplet size and production frequency.

BIBLIOGRAPHY

Abate, A. R., A. Poitzsch, et al. (2009). "Impact of inlet channel geometry on microfluidic drop formation." Physical Review E **80**(2).

Abate, A. R., M. B. Romanowsky, et al. (2009). "Valve-based flow focusing for drop formation." Applied Physics Letters **94**(2).

Abate, A. R., M. B. Romanowsky, et al. (2009). "Valve-based flow focusing for drop formation." Applied Physics Letters **94**(2): 023503.

Abate, A. R. and D. A. Weitz (2009). "High-Order Multiple Emulsions Formed in Poly(dimethylsiloxane) Microfluidics." Small **5**(18): 2030-2032.

Anderson, J. R., D. T. Chiu, et al. (2000). "Fabrication of topologically complex three-dimensional microfluidic systems in PDMS by rapid prototyping." Analytical Chemistry **72**(14): 3158-3164.

Anna, S. L., N. Bontoux, et al. (2003). "Formation of dispersions using "flow focusing" in microchannels." Applied Physics Letters **82**(3): 364-366.

Anna, S. L. and H. C. Mayer (2006). "Microscale tipstreaming in a microfluidic flow focusing device." Physics of Fluids **18**(12): 121512.

Atencia, J. and D. J. Beebe (2005). "Controlled microfluidic interfaces." Nature **437**(7059): 648-655.

Barbier, V., H. Willaime, et al. (2006). "Producing droplets in parallel microfluidic systems." Physical Review E **74**(4).

Baret, J. C., F. Kleinschmidt, et al. (2009). "Kinetic Aspects of Emulsion Stabilization by Surfactants: A Microfluidic Analysis." Langmuir **25**(11): 6088-6093.

Beer, F. P. and E. R. Johnston (1992). Mechanics of Materials. New York, McGraw-Hill, Inc.

Bentley, B. J. and L. G. Leal (1986). "An Experimental Investigation of Drop Deformation and Breakup in Steady, Two-Dimensional Linear Flows." Journal of Fluid Mechanics **167**: 241-283.

Binks, B. P. (2002). "Particles as surfactants - similarities and differences." Current Opinion in Colloid & Interface Science **7**(1-2): 21-41.

Binks, B. P. and S. O. Lumsdon (1999). "Stability of oil-in-water emulsions stabilised by silica particles." Physical Chemistry Chemical Physics **1**(12): 3007-3016.

Booty, M. R. and M. Siegel (2005). "Steady deformation and tip-streaming of a slender bubble with surfactant in an extensional flow." Journal of Fluid Mechanics **544**: 243-275.

Braisch, B., K. Kohler, et al. (2009). "Preparation and Flow Behaviour of Oil-In-Water Emulsions Stabilised by Hydrophilic Silica Particles." Chemical Engineering & Technology **32**(7): 1107-1112.

Chang, F. C. and Y. C. Su (2008). "Controlled double emulsification utilizing 3D PDMS microchannels." Journal of Micromechanics and Microengineering **18**(6).

Christopher, G. F. and S. L. Anna (2007). "Microfluidic methods for generating continuous droplet streams." Journal of Physics D-Applied Physics **40**: R319-R336.

Clegg, P. S., E. M. Herzig, et al. (2007). "Emulsification of partially miscible liquids using colloidal particles: Nonspherical and extended domain structures." Langmuir **23**(11): 5984-5994.

Datta, S. S., H. C. Shum, et al. (2010). "Controlled Buckling and Crumpling of Nanoparticle-Coated Droplets." Langmuir **26**(24): 18612-18616.
De Bruijn, R. A. (1993). "Tipstreaming of drops in Simple Shear Flows." Chemical Engineering Science **48**(2): 277-284.
Dinsmore, A. D., M. F. Hsu, et al. (2002). "Colloidosomes: Selectively permeable capsules composed of colloidal particles." Science **298**(5595): 1006-1009.
Dollet, B., W. van Hoeve, et al. (2008). "Role of the channel geometry on the bubble pinch-off in flow-focusing devices." Physical Review Letters **100**(3).
Drelich, A., F. Gomez, et al. (2010). "Evolution of water-in-oil emulsions stabilized with solid particles Influence of added emulsifier." Colloids and Surfaces a-Physicochemical and Engineering Aspects **365**(1-3): 171-177.
Du, K., E. Glogowski, et al. (2010). "Adsorption Energy of Nano- and Microparticles at Liquid-Liquid Interfaces." Langmuir **26**(15): 12518-12522.
Duffy, D. C., J. C. McDonald, et al. (1998). "Rapid prototyping of microfluidic systems in poly(dimethylsiloxane)." Analytical Chemistry **70**(23): 4974-4984.
Edmond, K. V., A. B. Schofield, et al. (2006). "Stable jets of viscoelastic fluids and self-assembled cylindrical capsules by hydrodynamic focusing." Langmuir **22**(21): 9052-9056.
Eggleton, C. D., T. M. Tsai, et al. (2001). "Tip streaming from a drop in the presence of surfactants." Physical Review Letters **87**(4).
Everage, A. E. and R. L. Ballman (1978). "The extensional flow capillary as a new method for extensional viscosity measurement." Nature **273**: 213-215.
Ferri, J. K. and K. J. Stebe (2000). "Which surfactants reduce surface tension faster? A scaling argument for diffusion-controlled adsorption." Advances in Colloid and Interface Science **85**(1): 61-97.
Fidalgo, L. M., C. Abell, et al. (2007). "Surface-induced droplet fusion in microfluidic devices." Lab on a Chip **7**(8): 984-986.
Fischer, C., C. J. G. Plummer, et al. (2007). "Pre- and post-transition behavior of shear-thickening fluids in oscillating shear." Rheologica Acta **46**: 1099–1108.
Fischer, P. and P. Erni (2007). "Emulsion drops in external flow fields - The role of liquid interfaces." Current Opinion in Colloid & Interface Science **12**(4-5): 196-205.
Fujii, S., A. Aichi, et al. (2009). "Ferritin as a bionano-particulate emulsifier." Journal of Colloid and Interface Science **338**(1): 222-228.
Garstecki, P., M. J. Fuerstman, et al. (2006). "Formation of droplets and bubbles in a microfluidic T-junction - scaling and mechanism of break-up." Lab on a Chip **6**(3): 437-446.
Garstecki, P., I. Gitlin, et al. (2004). "Formation of monodisperse bubbles in a microfluidic flow-focusing device." Applied Physics Letters **85**(13): 2649-2651.
Garstecki, P., M. Hashimoto, et al. (2008). "Formation of Bubbles and Droplets in Parallel, Coupled Flow-Focusing Geometries." Small **4**(10): 1795-1805.
Garstecki, P., H. A. Stone, et al. (2005). "Mechanism for flow-rate controlled breakup in confined geometries: A route to monodisperse emulsions." Physical Review Letters **94**(16): -.

Hillborg, H., N. Tomczak, et al. (2004). "Nanoscale hydrophobic recovery: A chemical force microscopy study of UV/ozone-treated cross-linked poly(dimethylsiloxane)." Langmuir **20**(3): 785-794.

Hsu, M. F., M. G. Nikolaides, et al. (2005). "Self-assembled shells composed of colloidal particles: Fabrication and characterization." Langmuir **21**(7): 2963-2970.

Hu, S. W., X. Q. Ren, et al. (2002). "Surface modification of poly(dimethylsiloxane) microfluidic devices by ultraviolet polymer grafting." Analytical Chemistry **74**(16): 4117-4123.

Hu, S. W., X. Q. Ren, et al. (2004). "Surface-directed, graft polymerization within microfluidic channels." Analytical Chemistry **76**(7): 1865-1870.

Hu, S. W., X. Q. Ren, et al. (2004). "Tailoring the surface properties of poly(dimethylsiloxane) microfluidic devices." Langmuir **20**(13): 5569-5574.

Husny, J. and J. J. Cooper-White (2006). "The effect of elasticity on drop creation in T-shaped microchannels." Journal of Non-Newtonian Fluid Mechanics **137**(1-3): 121-136.

James, D. F. and G. M. Chandler (1990). "A converging channel rheometer for the measurement of extensional viscosity." Journal of Non-Newtonian Fluid Mechanics **35**: 421-443.

James, D. F. and G. M. Chandler (1990). "Measurement of the extensional viscosity of M1 in a converging channel rheometer." Journal of Non-Newtonian Fluid Mechanics **35**: 445-458.

Kumacheva, E., W. Li, et al. (2009). "Multiple modular microfluidic (M(3)) reactors for the synthesis of polymer particles." Lab on a Chip **9**(18): 2715-2721.

Leal, L. G. (1992). Laminar Flow and Convective Transport Processes: Scaling Principles and Asymptotic Analysis. Boston, Butterworth-Heinemann.

Li, W., E. W. K. Young, et al. (2008). "Simultaneous generation of droplets with different dimensions in parallel integrated microfluidic droplet generators." Soft Matter **4**(2): 258-262.

Lin, B. H., B. D. Leahy, et al. (2010). "Geometric Stability and Elastic Response of a Supported Nanoparticle Film." Physical Review Letters **105**(5).

Lin, Y., A. Boker, et al. (2005). "Nanoparticle assembly at fluid interfaces: Structure and dynamics." Langmuir **21**(1): 191-194.

Lin, Y., H. Skaff, et al. (2003). "Nanoparticle assembly and transport at liquid-liquid interfaces." Science **299**(5604): 226-229.

Link, D. R., S. L. Anna, et al. (2004). "Geometrically mediated breakup of drops in microfluidic devices." Physical Review Letters **92**(5): -.

Liu, H. H. and Y. H. Zhang (2009). "Droplet formation in a T-shaped microfluidic junction." Journal of Applied Physics **106**(3).

Madou, M. J. (2002). Fundamentals of Microfabrication: The Science of Minaturization. Boca Raton, CRC Press.

Maffettone, P. L. and M. Minale (1998). "Equation of change for ellipsoidal drops in viscous flow." Journal of Non-Newtonian Fluid Mechanics **78**(2-3): 227-241.

Maffettone, P. L. and M. Minale (1998). "Equation of change for ellipsoidal drops in viscous flows." J. Non-Newtonian Fluid Mech. **78**: 227-241.

Makamba, H., J. H. Kim, et al. (2003). "Surface modification of poly(dimethylsiloxane) microchannels." Electrophoresis **24**(21): 3607-3619.

McClements, D. J. (1999). Food emulsions: principles, practice and techniques. Boca Raton, CRC Press.
McDonald, J. C., D. C. Duffy, et al. (2000). "Fabrication of microfluidic systems in poly(dimethylsiloxane)." Electrophoresis **21**: 27-40.
McDonald, J. C., D. C. Duffy, et al. (2000). "Fabrication of microfluidic systems in poly(dimethylsiloxane)." Electrophoresis **21**(1): 27-40.
McDonald, J. C. and G. M. Whitesides (2002). "Poly(dimethylsiloxane) as a material for fabricating microfluidic devices." Accounts of Chemical Research **35**(7): 491-499.
Mietus, W. G. P., O. K. Matar, et al. (2002). "Droplet deformation in confined shear and extensional flow." Chemical Engineering Science **57**(7): 1217-1230.
Migler, K. B. (2001). "String formation in sheared polymer blends: Coalescence, breakup, and finite size effects." Physical Review Letters **86**(6): 1023-1026.
Miller, E., M. Rotea, et al. (2010). "Microfluidic device incorporating closed loop feedback control for uniform and tunable production of micro-droplets and emulsions." Lab on a Chip **10**(10): 1293-1301.
Milliken, W. J., H. A. Stone, et al. (1993). "The Effect of Surfactant on the Transient Motion of Newtonian Drops." Physics of Fluids a-Fluid Dynamics **5**(1): 69-79.
Mulligan, M. K. and J. P. Rothstein (2011). "Deformation and Breakup of Micro- and Nanoparticle Stabilized Droplets in Microfluidic Extensional Flows." Langmuir **27**(16): 9760–9768.
Mulligan, M. K. and J. P. Rothstein (2011). "The Effect of Confinement-Induced Shear on Drop Deformation and Breakup in Microdluidic Extensional Flows." Physics of Fluids **23**(2): 022004.
Nguyen, N.-T. and S. T. Wereley (2006). Fundamentals and Applications of Microfluidics. Norwood, MA, Artech House, Inc.
Nie, Z. H., M. S. Seo, et al. (2008). "Emulsification in a microfluidic flow-focusing device: effect of the viscosities of the liquids." Microfluidics and Nanofluidics **5**(5): 585-594.
Nisisako, T., T. Torii, et al. (2002). "Droplet formation in a microchannel network." Lab on a Chip **2**(1): 24-26.
Olbricht, W. L. (1996). "Pore-scale prototypes of multiphase flow in porous media." Annual Review Fluid Mechanics **28**: 187 -213
Oliveira, M. S. N., M. A. Alves, et al. (2007). "Viscous flow through microfabricated hyperbolic contractions." Experiments in Fluids **43**(2-3): 437-451.
Pathak, J. A. and K. B. Migler (2003). "Droplet-string deformation and stability during microconfined shear flow." Langmuir **19**(21): 8667-8674.
Pickering, S. U. (1907). "Emulsions." Journal of the Chemical Society **91**: 2001-2021.
Pieranski, P. (1980). "Two-Dimensional Interfacial Colloidal Crystals." Physical Review Letters **45**(7): 569-572.
Pipe, C. J. and G. H. McKinley (2009). "Microfluidic rheometry." Mechanics Research Communications **36**(1): 110-120.
Randall, G. C., K. M. Schultz, et al. (2006). "Methods to electrophoretically stretch DNA: microcontractions, gels, and hybrid gel-microcontraction devices." Lab on a Chip **6**(4): 516-525.

Reynaert, S., P. Moldenaers, et al. (2006). "Control over colloidal aggregation in monolayers of latex particles at the oil-water interface." Langmuir **22**(11): 4936-4945.

Rodd, L. E., J. J. Cooper-White, et al. (2007). "Role of the elasticity number in the entry flow of dilute polymer solutions in micro-fabricated contraction geometries." Journal of Non-Newtonian Fluid Mechanics **143**: 170-191.

Rodd, L. E., T. P. Scott, et al. (2005). "The inertio-elastic planar entry flow of low-viscosity elastic fluids in micro-fabricated geometries." Journal of Non-Newtonian Fluid Mechanics **129**: 1-22.

Sander, J. S. and A. R. Studart (2011). "Monodisperse Functional Colloidosomes with Tailored Nanoparticle Shells." Langmuir **27**(7): 3301-3307.

Shu, L., J. C. T. Eijkel, et al. (2007). "Multiphase flow in microfluidic systems - Control and applications of droplets and interfaces." Advances in Colloid and Interface Science **133**: 35-49.

Stone, H. A. (1994). "Dynamics of Drop Deformation and Breakup in Viscous Fluids." Annual Review of Fluid Mechanics **26**: 65-102.

Stone, H. A. and L. G. Leal (1990). "THE EFFECTS OF SURFACTANTS ON DROP DEFORMATION AND BREAKUP." Journal of Fluid Mechanics **220**: 161-186.

Stone, H. A., A. D. Stroock, et al. (2004). "Engineering flows in small devices: Microfluidics toward a lab-on-a-chip." Annual Review of Fluid Mechanics **36**: 381-411.

Taylor, G. I. (1932). "The viscosity of a fluid containing small drops of another fluid." Proceedings of the Royal Society of London Series a-Containing Papers of a Mathematical and Physical Character **138**(834): 41-48.

Taylor, G. I. (1934). "The formation of emulsions in definable fields of flow." Proceedings of the Royal Society of London Series a-Mathematical and Physical Sciences **146**(A858): 0501-0523.

Teh, S. Y., R. Lin, et al. (2008). "Droplet microfluidics." Lab on a Chip **8**(2): 198-220.

Thorsen, T., R. W. Roberts, et al. (2001). "Dynamic pattern formation in a vesicle-generating microfluidic device." Physical Review Letters **86**(18): 4163-4166.

Tong, W., Y. J. Huang, et al. (2010). "The morphology of immiscible PDMS/PIB blends filled with silica nanoparticles under shear flow." Colloid and Polymer Science **288**(7): 753-760.

van Puyvelde, P., A. Vananroye, et al. (2008). "Review on morphology development of immiscible blends in confined shear flow." Polymer **49**: 5363-5372.

Vananroye, A., P. Van Puyvelde, et al. (2006). "Effect of confinement on droplet breakup in sheared emulsions." Langmuir **22**(9): 3972-3974.

Vananroye, A., P. Van Puyvelde, et al. (2007). "Effect of confinement on the steady-state behavior of single droplets during shear flow." Journal of Rheology **51**(1): 139-153.

Vella, D., P. Aussillous, et al. (2004). "Elasticity of an interfacial particle raft." Europhysics Letters **68**(2): 212-218.

Vignati, E., R. Piazza, et al. (2003). "Pickering emulsions: Interfacial tension, colloidal layer morphology, and trapped-particle motion." Langmuir **19**(17): 6650-6656.

Wang, S., Y. J. He, et al. (2010). "Study of Pickering emulsions stabilized by mixed particles of silica and calcite." Particuology **8**(4): 390-393.

Wang, Y. L., H. H. Lai, et al. (2005). "Covalent micropatterning of poly(dimethylsiloxane) by photografting through a mask." Analytical Chemistry **77**(23): 7539-7546.

Ward, T., M. Faivre, et al. (2005). "Microfluidic flow focusing: Drop size and scaling in pressure versus flow-rate-driven pumping." Electrophoresis **26**(19): 3716-3724.

White, E. E. B., M. Chellamuthu, et al. (2010). "Extensional rheology of a shear-thickening cornstarch and water suspension." Rheologica Acta **49**(2): 119-129.

Whitesides, G. M. (2006). "The origins and the future of microfluidics." Nature **442**(7101): 368-373.

Whitesides, G. M. and A. D. Stroock (2001). "Flexible methods for microfluidics." Physics Today **54**(6): 42-48.

Xu, S. Q., Z. H. Nie, et al. (2005). "Generation of monodisperse particles by using microfluidics: Control over size, shape, and composition." Angewandte Chemie-International Edition **44**(5): 724-728.

Yeh, C. H., S. J. Lee, et al. (2008). "Manipulating T-junction chip for the generation of uniform O/W and W/O emulsions - art. no. 688610." Microfluidics, Biomems, and Medical Microsystems Vi **6886**: 88610-88610 175.

Zeng, C., H. Bissig, et al. (2006). "Particles on droplets: from fundamental physics to novel materials." Solid State Communications **139**: 547-556.